Vibration-based Energy Harvesting for Wireless Sensors used in Machine Condition Monitoring

Qing Ou

A thesis submitted in partial fulfilment
of the requirements for the degree of
Doctor of Philosophy
in
Mechanical Engineering
at the
University of Canterbury
Christchurch, New Zealand

XiaoQi Chen
Alan Wood
Stefanie Gutschmidt
Nigel Leigh

November 11, 2012

Abstract

In a wide range of industries, machine condition monitoring is one of the most cost effective ways to minimise maintenance efforts and machine down-time. To implement such a system, wireless solutions have increasingly become an attractive proposition due to the ease of installation and minimal infrastructure alternation. However, currently most wireless sensors in the world are powered by a finite battery source. The dependence of batteries not only requires frequent maintenance, but also has adverse environmental consequences associated with battery disposal. These reasons render massive deployment of wireless sensors in the industry problematic. With the advances in semiconductors, power consumption of wireless sensors has been continuously decreasing. It is an inevitable trend for self-powered wireless sensors to emerge and become the norm for machine and environmental monitoring. In this research, vibration is chosen to be the energy source to enable self-powered wireless sensors due to its ubiquitousness in machinery and industrial environments. As a result of relying on resonance, the biggest challenge for vibration-based energy harvesters is their narrow bandwidth. Even a small deviation of the vibration frequency can dramatically reduce the power output. The primary goal of this research is to address this problem. In particular, Piezoelectric generators are identified to be the most suitable technology. In this work, extensive theoretical and experimental studies are conducted in single mass and multi-modal harvesters, and in resonance tuning harvesters by modulus and impedance matching as well as by mechanical actuation. Mathematical modelling plays a significant role in energy harvester designs. A dynamic model that generalises the single degree of freedom models and the continuum models is derived and validated by experiments. The model serves as the building block for the whole research, and it is further refined for the investigation of modulus and impedance matching. In the study of multi-modal harvesters, a continuum model for double-mass piezoelectric cantilever beams is derived and experimentally validated. To study the feasibility of resonance tuning by mechanical means, prototypes were built and performance evaluated. This document details the theoretical basis, concepts and experimental results that extend the current knowledge in the field of energy harvesting. This research work, being highly industrially focused, is believed to be a very significant step forward to a commercial energy harvester that works for a wide range of vibration frequencies.

Publications

A. Wood, Q. Ou, N. Leigh, X.Q. Chen, S. Gutschmidt (2012) "Tunable Vibration Energy Harvester and Method", U.S Patent.

Q. Ou, X.Q. Chen, S. Gutschmidt, A. Wood, N. Leigh and A.F. Arrieta, "An Experimentally Validated Double-mass Piezoelectric Cantilever Model for Broadband Vibration-based Energy Harvesting," *Journal of Intelligent Systems and Structures,* vol. 23, no. 2, pp. 117-126, 2012

Q. Ou, X.Q. Chen, S. Gutschmidt, A. Wood, N. Nigel (2010) "A Two-mass Cantilever Beam Model for Vibration Energy Harvesting Applications," *Toronto, Canada: 6th IEEE Conference on Automation Science and Engineering (CASE 2010)*, August 21-24 2010.

Dedication

To my parents

Acknowledgements

In the journey of this research, I was repeatedly overwhelmed by the passion of the supervisory team. The wisdom and inspiration I got from them benefit me a lifetime. For the supervisory team, I would like to express my gratitude to my senior supervisor Prof. XiaoQi Chen, co-supervisor Dr. Alan Wood and Dr. Stefanie gutschmidt, and industry supervisor Nigel Leigh. It is hard to acknowledge their contribution to this work without having to make it sound overly generic. But from the bottom of my heart, I really mean it. Without them the outcome of this research would have been impossible. Their areas of expertise form a perfect team steering me to the success of this project. Over the three years, I am very grateful for being fortunate enough to be guided by the very best people, and to be given plentiful resources and financial support to do this research.

XiaoQi, thank you for overseeing the research project. It was you who suggested me to do a PhD at the first place. Now I think that is the best advice I have taken so far in my life. Without your constant feedback on progress and publications, I would not have completed my PhD on time. You are always the person who gets the job done, coordinates people and makes resources and funding available.

Alan, thank you so much for your patience and technical advice. You always have too many ideas than I can fully evaluate and too many questions than I can fully answer. Your enthusiasm on this project sometimes makes me believe you are the one who is doing the research. You are always available for questions and discussions. You even helped me read through data sheets and do measurement. As a student of yours, there is nothing more I could ask for.

Stefanie, thank you for teaching me theories in dynamics and many skills and tricks for doing research. The funding you sourced for me to attend the two international conferences really meant a lot to me. It has broadened my life experience greatly, and given me the opportunity to network with fellow researchers. The high editing quality of all publications and the thesis is credited to your meticulous attitude on proof reading and the very best editing skills you passed to me.

Nigel, thank you for your guidance to maintain this academic research so industrially focused. Your vision on the technologies for the energy industry enlightened me. Your experience and industrial knowledge is invaluable input to this project. Other than technical skills, I have learnt many personal skills from you that I think are essential for an engineer. It has been a wonderful

experience to have you as my mentor.

In addition, I owe my thanks to Wout Herman, who has done an excellent job on the design and prototyping of the two resonance tuning concepts.

To the technicians at the University of Canterbury, Julian Phillips, Garry Cotton, Ken Brown, Julian Murphy, Graeme Harris and Scott Amies, thank you all for the much needed advice and assistance you offered when I designed and built my prototypes, and set up my experiments.

I would like to gratefully acknowledge the support of the Ministry of Science and Innovation (MSI) fellowship, project number CILX0801, and the financial and technical support provided by GE Energy Ltd.

The people who I have interacted with, things I have experienced, observed, learned, unlearned and relearned over the course of this research have profoundly changed my attitude towards life in many positive ways.

Contents

List of Figures

List of Tables

Nomenclature

$\bar{\Theta}_{bc}$	Backward coupling constant in continuum model
$\bar{\Theta}_{fc}$	Forward coupling constant in continuum model
$\bar{M}_{eq}$	Equivalent proof mass in continuum model
β_r	Eigenvalues of the rth vibration mode
χ_r	modal electromechanical coupling term
$\delta_{ave}(t)$	Average strain of beam as a function of time
$\eta_r(t)$	Time dependent amplitude function of the rth vibration mode
κ_a	Ratio of vertical force on tip mass to average stress of beam
κ_b	Ratio of average strain to vertical displacement of proof mass
κ_{pt}	Power transmission factor
λ_r	Eigenvalues
μ_c	Correction factor between lumped-mass and continuum models
ω	Angular frequency input
ω_n	Natural angular frequency
ω_r	Natural angular frequency of the rth vibration mode
Ω_{oc}	Ratio of open circuit frequency to natural frequency
ω_{opt}	Optimal angular frequency input
Ω_{sc}	Ratio of short circuit frequency to natural frequency
$\phi_{r,seg}$	Modified eigenfunctions for electrode segmentation
$\phi_r(x)$	Mass normalised eigenfunction of the rth vibration mode
ρ_e	Resistivity
$\sigma(x)$	Stress of beam as a function of beam length
σ_p	PZT stress
$\sigma_{ave}(t)$	Average stress of beam as a function of time
$\tan\theta_{LT}$	Loss tangent

Θ_{bc} Backward coupling constant in generalised model

Θ_{fc} Forward coupling constant in generalised model

$\tilde{\Theta}_{bc}$ Backward coupling constant in lumped-mass model

$\tilde{\Theta}_{fc}$ Forward coupling constant in lumped-mass model

$\tilde{C}_m$ Damping constant of lumped-mass model

$\tilde{K}_{sp}$ Spring constant of lumped-mass model

$\tilde{w}_n(x,t)$ Absolute vertical displacement of the nth segment

ε_{33}^S permittivity at constant strain

ε_{33}^T Permittivity at constant stress

φ_r Forward coupling constant

ϑ Electromechanical backward coupling term

ξ_e Electrical damping ratio

ξ_m Mechanical damping ratio

ξ_r Mechanical damping ratio of the rth vibration mode

ξ_T Total damping ratio

A Acceleration amplitude

A_{pe} Effective PZT area

b Beam width

b_e Effective beam width

C Capacitance

C_e Electrical damping constant

C_L Load capacitance

C_m Mechanical damping constant

C_r Modal amplitude constant

c_s Equivalent strain rate damping constant

C_{eq} Equivalent damping constant

C_{pe} Effective internal PZT capacitance

D_3 Electrical displacement

d_{31} PZT constant

E Energy

E_3 Electrical field

e_{31} PZT constant

$F_m(t)$ Force exerted by the proof mass as a function of time

F_r External forcing function amplitude

$f_r(t)$ External forcing function

$f_{ext}(t)$ External forcing function in unit force per unit length

F_H The highest frequency

F_L The lowest frequency

F_{range} Frequency range

h_c Distance from centre of PZT layer to centre of substrate

h_p Thickness of a single PZT layer

h_s Thickness of substrate

h_{pe} Effective PZT layer thickness

I Overall second moment of areas

$i_L(t)$ Load current as a function of time

$I_o(\omega)$ Current output as a function of angular frequency

I_p Second moment of areas of the two PZT layers

$I_p(\omega)$ PZT current as a function of angular frequency

I_s Second moment of areas of substrate

I_t Moment of inertia of the proof mass about the y-axis

i_x Average current per length

I_{tn} Moment of inertia of the nth mass about the central axis in y direction

j Imaginary number

k Spring constant

k_{31} PZT electromechanical coupling coefficient

K_{eq} Equivalent spring constant

k_{sp} Spring constant

L Inductance

L_b Beam length

L_n Beam length of the nth segment

L_s Electrode segmentation length

m Proof mass or mass per unit length of the beam

$M(x)$ Bending moment as a function of beam length

m_n Mass per unit length of the nth segment

M_t Proof mass

M_{eq} Equivalent proof mass

M_{tn} The nth proof mass

P power output

$P_a(\omega)$ Power as a function of angular frequency in constant base acceleration

P_L Power losses

$P_v(\omega)$ Power as a function of angular frequency in constant base velocity

$P_y(\omega)$ Power as a function of angular frequency in constant base displacement

Q Electrical charge or quality factor

R_c Resistance of both PZT conducting layers combined

R_L Resistive load

$R_p(\omega)$ Frequency dependent resistance to model polarisation losses

R_{ce} Effective resistance to model ohmic losses

R_{cx} Average resistance per length

R_{esr} Series equivalent resistance

S_1 Longitudinal strain

V Voltage output

V_F Diode forward voltage drop

$V_o(\omega)$ Voltage output as a function of angular frequency

$v_o(t)$ PZT output voltage as a function of time

$V_p(\omega)$ PZT voltage as a function of angular frequency

$V_s(\omega)$ Source voltage of Thévenin equivalent circuit

$v_{dc}(t)$ Rectified DC voltage as a function of time

$w(x)$ Relative vertical displacement as a function of beam length

$w_b(t)$ Base displacement as a function of time

$w_L(t)$ Relative vertical displacement of proof mass as a function of time

$w_n(x_n, t)$ Relative vertical displacement of the nth segment

$x(t)$ Absolute vertical displacement of proof mass as a function of time

$y(t)$ Displacement of base as a function of time

Y_0 Displacement amplitude of base

Y_p Young's modulus of PZT

Y_s Young's modulus of substrate

$Z(\omega)$ Relative displacement as a function of angular frequency

$z(t)$ Relative vertical displacement of proof mass as a function of time

Z_C Impedance of a capacitor

Z_L Load impedance

$Z_p(\omega)$ Characteristic impedance of PZT as a function of angular frequency

AC Alternating current

CMOS Complementary metaloxidesemiconductor

DC Direct current

ESC Extremum Seeking Control

ESR Equivalent Series Resistance

FEM Finite Element Method

FFT Fast Fourier Transform

FoM Figure of merit

FRF Frequency Response Function

FWHM Full width at half maximum

MEMS Microelectromechanical systems

MOSFET Metaloxidesemiconductor field-effect transistor

Ni Nickel

ODE Ordinary Differential Equation

PDE Partial differential equation

POM Polyoxymethlene

PVDF Polyvinylidene fluoride

PZT Lead Zirconate Titanate

RF Radio frequency

RFID Radio frequency identification

rms Root mean square

RPM Revolution per minute

std Standard deviation

T Kinetic energy

U Potential energy

1 Introduction

1.1 Machine Condition Monitoring

In a wide range of industries, machine condition monitoring is adopted in maintenance programs to predict machine failures. A machine condition monitoring system regularly measures key indicators such as mechanical vibrations, pressure and temperature of critical machines, and tracks the information over time to look for abnormal changes. Once the earliest signs of failure are discovered, informed decision can be made and maintenance activities scheduled. Compared to traditional maintenance methods that either replace parts in a fixed schedule whether worn or not, or repair machines only after they have broken down, predictive maintenance is only scheduled on machines that need attention. In this manner, the system can bring huge cost saving by keeping both maintenance efforts and machine downtime minimal.

For most machines, vibration is the single most effective parameter to monitor. From captured vibration data, typically obtained by a cabled accelerometer, information about bearing health, misalignment and imbalance (amongst other things) can be assessed, and the machine scheduled for repair before a major and expensive problem arises. Autonomous monitoring systems or on-line systems allow vibration data to be captured according to pre-set routines and rules, and transmitted through computer networks. Analysis is processed in a computer, together with specialised software tools to predict machine conditions with great accuracy.

Accurate assessment of machine condition relies upon the information gathered. For this reason multiple sensors are usually installed on each machine. Although machine condition monitoring has been so beneficial, the costs of installing the vast amount of cabling for all the sensors can be prohibitively

high. Sometimes these costs exceed that of the whole monitoring system itself. Furthermore, in environments such as marine vessels, alteration of the infrastructure is difficult and highly undesirable [1]. For remote area operations, such as mining, electrical cables are hard to come by, and machines are mobile. There are many more circumstances where installation of vast amount of cabling is impractical.

Wireless sensing solutions are desirable to eliminate the costs associated with installing the cabling, and to overcome the problems where the use of cabling is impractical. However, battery-powered wireless sensor nodes are problematic for large-scale deployment both because of the adverse environmental effects associated with battery disposal, and the labour required for battery replacement on a regular basis, which detract from the many advantages a wireless solution offers. With advances in semiconductor technology, the size and power consumption of wireless sensors continue to decrease [2]. This trend enables the emergence of self-powered wireless sensors. By harvesting the power from the environment, sensors can be made self-sufficient over its life time with virtually no maintenance [1]. Not only will this technology allow expansion of the current wireless sensor networks, but also will it enable new applications. For example, self-powered wireless sensors can be embedded in roads, machines, constructions and under the deep ground for conditional and environmental monitoring. The vast possibilities of the applications could eventually revolutionise the way how assets and environments are monitored in general.

1.2 Energy Harvesting Basics

Energy harvesting, sometimes referred to as energy scavenging, is a process of converting ambient energy sources such as light, heat, vibration, and RF energy into usable electrical energy to provide power for electronic devices. In recent years, many commercial sectors have shown considerable interest in implementing energy harvesting technologies on wireless sensors used for structural and machine condition monitoring. The primary benefits are to eliminate the maintenance costs, and to permit permanent installation of wireless sensors in inaccessible and remote locations. Current energy harvesting research falls into two key areas: the design of the harvester and the design of the interfacing circuit that delivers electrical power to the load. In general, an energy harvesting system consists of three key components as shown in Figure 1.1: i) energy harvester, ii) power conditioning circuitry and

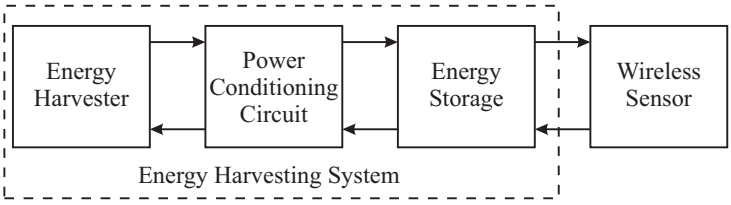

Figure 1.1: Components in a self-powered wireless sensor.

iii) energy storage reservoirs. The energy harvester is essentially a transducer that converts mechanical energy into electrical energy. As is the nature of all energy harvesting methods, electrical energy harvested by the generator is always irregular and/or intermittent. To make this a usable energy source, a power conditioning circuit is required to regulate the power to a suitable voltage and current level. Sensors relying on energy harvesting technology as the sole power source are unlikely being able to operate continuously. They usually operate at very low duty cycles. Hence it is necessary to accumulate the harvested energy in storage elements while the sensor is in sleep mode, and a burst of power is drawn when the sensor wakes up to perform its task.

1.3 Wireless Sensors and Power Requirement

This research was initiated by GE Energy Ltd, who wanted to investigate the possibility of adapting energy harvesting to its wireless sensor Ranger [3](see Figure 1.2) designed for machine condition monitoring. The Ranger

Figure 1.2: Ranger wireless sensor for machine condition monitoring. [3]

contains a biaxial accelerometer and a temperature sensor. While spending most of its time in sleep mode, Ranger wakes up to take recordings according to pre-set schedules and rules. Captured data is transmitted to a Ranger station, which then makes the data available in the TCP/IP network and/or internet. Ranger sensor is in cylindrical shape of 41 mm diameter and 43

mm tall, and weight 168 g. Currently the sensor is powered by a 3.6 V, 1.7 Ah non-rechargeable lithium ion battery pack. The diameter of the battery is 32.9 mm, height 10.2 mm and weight 21 g. Power profile of the sensor was determined by experiments. Each measurement takes 4.6 J, and the peak current during recording is about 100 mA. Typical usage of the sensor is to take 6 recordings per day. Each recording is configured as dual-channel vibration capture with 1024 samples, and 1 kHz maximum frequency. Based on this typical setting, the average power consumption is 0.24 mW and the peak power is 273.6 mW. Therefore, at least 0.24 mW of power in average the energy harvesting module has to deliver to make the wireless sensor completely self-powered.

1.4 Comparison of Energy Harvesting Technologies

With rapid advancement in semiconductor and nanotechnology, the power consumption of electronic systems continues to decrease. As a result, energy harvesting technologies show great promises to enable self-powered devices. Energy in the surrounding environment is abundant, but in very different forms. The most common ambient sources that have been of interest for energy harvesting are listed in Table 1.1. The choice of energy source depends

Table 1.1: Energy Density Estimate (From TI Newsletter [4]).

Energy Source	Environment	Power Density (mW/cm^2)
Solar	Outdoor	10
	Indoor	0.01
Thermal	Industry	1–10
RF	GSM	0.0001
	WiFi	0.001
Vibration	Industry	0.1

on the application at hand. One-for-all energy harvesting solution that will provide power for all potential applications do not exist [5]. Solutions need to be tailored based upon the power requirement and the operating environment of the application. A brief evaluation of each potential ambient energy source and their suitability for the Ranger wireless sensor is discussed in this section.

1.4.1 Solar

Solar energy is so far the most exploited ambient energy source. Utilisation of solar energy is technologically mature compared to other energy sources. This solution is cost effective for applications where a reliable light source is available. In most cases solar energy is the best alternative for outdoor applications. Even near the poles of the earth, 10 mW/cm^2 of power density is received on the surface under direct sunlight. Given that a commercially available photovoltaic cell typically provides an efficiency of 15% [6], the electrical power density converted from the cell is 1.5 mW/cm^2. If a solar panel is used on the top of the Ranger wireless sensor where the available area is about 10 cm^2, 15 mW of power could be generated under direct sunlight. An average of 3.75 mW is harvested in the assumption of 6 hours of direct sunlight per day. Compared to 0.24 mW required by the Ranger, the solar energy solution seems promising. However, for indoor usage under normal fluorescent lights, the solar cell decreases its power output by a factor of 1000 (Table 1.1). Even with an optimistic assumption of 24 hours lighting per day, power output is only 15 μW for the available area, which is insufficient to power the sensor.

1.4.2 Thermal

Thermoelectric generators convert temperature gradient into electricity by a special material property known as the Seebeck effect [7]. Thermal generators can be found in watches that extract power from human body heat (e.g. Seiko Thermic wristwatches). One of the commercially available thermoelectric generators is Micropelt thin film thermoelectric generator [8]. The size of Micropelt is similar to a surface mount IC package, and it comes in a footprint of only 3.2 mm $\times$ 4.2 mm. With the available area on sensor, six of these generators can be used. The product data sheet indicates that the total power output from six Micropelt generators is about 1 mW in 5 K temperature gradient. However, temperature gradient is highly dependent on the nature of the sensor operating environment considered. It is unrealistic to expect that reliable and adequate thermal gradients present in majority of the sensor operating environments. Furthermore, the required heat sink necessary to facilitate temperature difference can greatly increase the total volume. In the case of utilising the sensor steel housing as a heat sink, substantial changes have to be made to the mechanical design of the sensor.

1.4.3 Radio Frequency

In very populated areas, radio frequency (RF) energy from Wifi, cellular phone networks, and broadcast radio and TV signals is widespread and abundant. For certain applications RF energy can be a preferable energy source. RF energy conversion is realised by a rectifying antenna that is constructed with a Schottky diode located between the antenna dipoles [9]. Attempts have been made by researchers from Intel® to successfully harvest 60 mW of power from a TV antenna [10]. In spite of the large coverage, the disparate RF energy sources actually possess a very low power density. Figures shown in Table 1.1 indicate that the power density from RF is at least 2 orders of magnitude smaller than other ambient energy sources. Low power density implies a relatively large volume of energy harvester is required to obtain the same amount of power. Given the volume constraint of the Ranger wireless sensor, RF energy harvesting is not a suitable option. Radio Frequency Identification (RFID) is a passive way of energy transmission through a dedicated RF broadcasting device. It should be noted that RFID is an energy distribution method rather than an energy harvesting method. The range of power transmission is dependent on the amount of power broadcasting from the RF transmitter (typically less than a few meters [11]). In many countries, the maximum RF power transmission allowed is limited by regulations (typically 1 W [12]). Hence the very limited range of RFID means it is not a suitable method to power the Ranger wireless sensor.

1.4.4 Vibration

Vibration is one of the most ubiquitous energy sources present in the environment where the Ranger is designed for. Therefore, vibration is a guaranteed energy source. Moreover, its power density is higher than indoor light source. There are three methods commonly used for converting mechanical vibrations into electrical energy, namely electromagnetic, piezoelectric and electrostatic [13]. Although these three methods differ significantly in construction, the power output under resonance can be represented by a generalised equation derived from a spring damper system [13]:

$$P = \frac{m\xi_e A^2}{4\omega(\xi_e + \xi_m)^2}, \tag{1.1}$$

where P is the peak power output, m is the proof mass, A is the acceleration amplitude of the source vibration, ω is the excitation angular frequency, ξ_e

and ξ_m are the electrically induced and mechanical damping ratios, respectively. A brief description of the underlying principle for each vibrational energy conversion method is given in the following subsections. A brief description of the underlying principle for each vibrational energy conversion method is given in the following subsections.

Electromagnetic

Electromagnetic harvesters generates electricity according to electrical induction principles. Electrical power is generated by the changes of magnetic flux through a coil, which can be achieved by relative motions between a coil and a magnet. Components of a common electromagnetic harvester include a permanent magnet, a coil and a spring. The voltage generated is proportional to the number of turns in the coil. The maximum number of turns allowed is limited by the available volume. It was proven by Shad that only 100 mV is possible within a volume of 1 cm^3 [14]. The very low AC voltage output presents a challenge to the power conditioning circuit. Although micro-scale electromagnetic generators have been demonstrated [15], within which the limited number of turns on planar coils means the output voltage is far too low (i.e. micro-volts) to be utilised for most electronic systems. On the other hand, electromagnetic harvesters that produce a decent output voltage level are normally in macro-scale (e.g. the Perpetuum energy harvesters, 55.5 mm $\times$ 55.5 mm diameter). The merit of electromagnetic harvesters is that damping can be controlled electrically to mitigate impacts when subject to violent vibrations. Electromagnetic harvesters are also robust, reliable and thus they are excellent for industrial applications. The primary drawbacks are the relatively high part counts and low AC output voltage. While a miniature transformer can be used to step up the AC output voltage, the parts count will be further increased.

Electrostatic

An electrostatic harvester is essentially a variable capacitor. When subject to external vibrations, the capacitance of the harvester can be changed cyclically by either changing the effective area or the distance between parallel plates. In order to extract energy from the oscillating capacitance, additional electronics are needed to control the voltage and current (i.e. charge)

accordingly. As can be seen in

$$C = \frac{Q}{V}, \tag{1.2}$$

when the capacitance is increasing, holding voltage constant results in an increase in charge. When the capacitance is decreasing, holding charge constant results in an increase in voltage. In either case, the energy stored in the capacitor increases, as can be deduced from

$$E = \frac{1}{2}VQ. \tag{1.3}$$

The major advantage of electrostatic harvesters is that they are perfectly compatible with current CMOS and MEMS technologies. Hence they can potentially be produced in small footprints inexpensively. However, according to (1.1), power output is proportional to proof mass. Small silicon based packaging limits the amount of proof mass, so as the generated power. Additional disadvantages associated with an electrostatic generator are: 1) that it requires a separate voltage source to charge up the capacitor to initiate the energy conversion process, and 2) its reliability may be compromised due to the fact that in the presence of excessive external vibrations, capacitor electrodes can come into contact and lead to a short circuit [5].

Piezoelectric

Properties of piezoelectric material are well-known and fully exploited in a broad range of applications. Piezoelectric generators utilise the piezoelectric effect that when the material is under stress, the developed strain causes charge separation across the electrodes, and yields a voltage. A piezoelectric harvester can be simply constructed by a piezoelectric cantilever beam with a proof mass on its free end. Lead Zirconate Titanate (PZT) is a low cost and widely available piezoelectric material. The output voltage of a piezoelectric harvester is typically between 5 to 20 V, which is a perfect AC voltage range that can be directly rectified by off-the-shelf full-bridge rectifiers such as DF005S. Due to their simplicity, piezoelectric harvesters have received substantial research interest [16, 17]. Furthermore, unlike electrostatic harvesters, piezoelectric harvesters require no external voltage source, and are compatible with CMOS and MEMS technologies as being demonstrated by a number of researchers [18, 19, 20, 21]. One of the disadvantages of piezoelectric material is that the piezoelectric effect deteriorates over time [22]. In addition, most commonly used piezoelectric material Zirconate Titanate

(PZT) is quite brittle. Once subject to a stress that is greater than the yield stress, the piezoelectric material will crack and lose most of its power conversion capability. In the case where a more flexible piezoelectric film (e.g. PVDF polymer) is used, the mechanical coupling coefficient is compromised, leading a lower power output.

1.5 The Most Suitable Technology

After a brief review of various energy sources and harvesting principles, the most suitable technology needs to be chosen for the Ranger wireless sensor. The temperature gradients can vary significantly depending on where the Ranger is used, hence it is unreliable. Large and cumbersome RF antennas also makes RF energy source unsuitable for the Ranger wireless sensor. Although solar energy is excellent for outdoor applications, it is not able to supply enough power for indoor use. Since the Ranger is designed for machine condition monitoring, vibration seams to be the most reliable energy source. Comparison of the three vibration energy harvesting methods has been carried out extensively by researchers [12, 13, 23, 17]. The common conclusions drawn are that, in general, electromagnetic conversion is capable of producing high power but large in size and the output voltage is very low, while electrostatic harvesters benefit from smaller size, they are only suitable for ultra-low-power applications. Piezoelectric harvesters have both moderate size, power output and the output voltage is relatively high. Due to the limitations on size and proof mass, power output of electrostatic harvesters demonstrated in the literature typically produce less than 100 μW. Reliability is one of the foremost concerns for products used in the industry. Electrostatic harvesters, being less reliable than the other two types of harvesters, are apparently not the best choice. Greater than 200 μW of power output is found more commonly in piezoelectric and electromagnetic harvesters. Comparison shown in Table 1.2 further confirms that piezoelectric and electromagnetic methods hold the greatest potential to meet the Ranger's requirements. Compared to electromagnetic harvesters that tend to be bulky and produce a very low output voltage, piezoelectric harvesters are much simpler and more compact in construction, and they generate a much higher voltage. As a result, this research is focused on piezoelectric technology for the Ranger wireless sensors.

Table 1.2: Energy Storage Density Comparison [5].

Type	Practical Maximum (mJ/cm^3)	Theoretical Maximum (mJ/cm^3)
Electromagnetic	24.8	400
Piezoelectric	35.4	335
Electrostatic	4.0	44

1.6 Problems with Harvesting Energy from Machine Vibrations

Despite the various methods (in Section 1.4.4) of converting mechanical vibration into electrical energy, they all rely on operating at resonance. Power can be generated effectively only when the frequency of the source vibration (driving frequency) matches the resonant frequency of the harvester. When the driving frequency deviates even 1 or 2 Hz from the resonant frequency of the harvester, power output decreases dramatically. This is the very same problem faced by today's vibration-based energy harvesting products[1]. Historically, machines tended to run at fixed speeds dictated by the mains-power frequency. This allowed an energy harvester to be pre-turned to that running speed. But modern industrial processes are now often variable speed to optimise energy efficiency and provide more process flexibility. So a fixed frequency vibration harvester may spend a lot of its life time operating at a very low efficiency.

Furthermore, stringent manufacturing precision would be required to produce a harvester to meet a particular resonant frequency. Alternatively a manual tuning process could be used. But even then, material ageing, wear and temperature variations will cause the resonant frequency to drift over time. An energy harvester that can generate power efficiently over a wide range of frequency without human intervention is necessary to resolve these problems.

1.7 Thesis Scope and Objectives

While this research aims to push the frontier of energy harvesting systems, the existing area in this field are too broad to comprehend. Some of the key

[1]Perpetuum, Advanced Ceramics, KCF, CEDRAT Technologies, Ferro Solutions, Mide Technology Corporation

components are illustrated in Figure 1.3. The components included in this

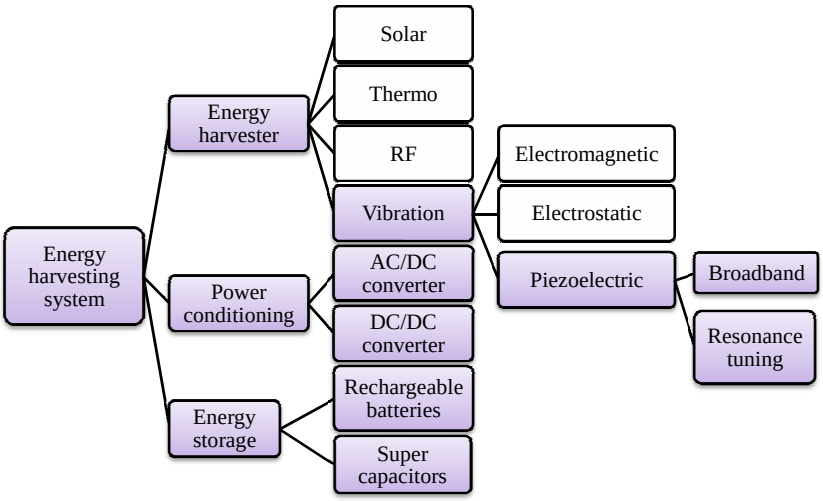

Figure 1.3: Energy harvesting system research components and scope.

work are highlighted by the filled boxes. The main focus of this research is the modelling and design of piezoelectric energy harvesters. Although power conditioning and energy storage are also included in the scope, they will not be investigated to the same breadth and depth compared to piezoelectric energy harvesters.

This research is geared towards the development of a commercial product, therefore, many constraints will eventually have to be imposed. The preliminary requirements for the size of the harvester is 60 mm diameter $\times$ 50 mm height. The weight of the harvester should not exceed 400 g. However, the main goal of this research is to provide an effective solution and proof of concept for wide frequency range vibration-based energy harvesters that can produce at least 0.24 mW of power for Commtest's wireless sensor. This goal breaks down to the objectives below:

- Identify the most favourable frequency range and vibration levels of industrial machine vibrations
- Develop an accurate model for piezoelectric energy harvesters
- Propose suitable solutions for wide frequency range energy harvesters
- Study each solution theoretically and experimentally
- Choose the best solution and propose a practical implementation

1.8 Thesis Layout and contributions

The main body of this thesis is centred around five topics: machine vibration characteristics, single mass piezoelectric energy harvesters, multi-modal piezoelectric energy harvesters, resonance tuning by impedance matching and resonance tuning by mechanical actuation. Among which, presented in the last three topics are independent ways of achieving wide frequency range harvesters. In Chapter 2, the state of the art on each of these topics are presented and their performance is discussed. The research work carried out to enhance the knowledge on each of these topics is then elaborated in Chapter 3 - 7. Conclusions are given in Chapter 8. The major contributions of this research work are presented in Chapter 3 - 7, which are summarised as follows.

In chapter 3, one of the major contributions is to produce a set of statistics for industrial machinery vibrations. The statistics are entirely produced from an energy harvesting perspective, therefore they can serve as an important reference for the energy harvesting community where the application is focused on machine vibrations. The statistics are valuable because understanding of the source vibration characteristics before designing the harvester can tremendously increase the chance of the harvester being commercialised. The presented statistics shed light on what acceleration level, frequency range and proof mass the harvester should be designed for, which are some of the critical design decisions to be made at the beginning of a product development process. Another contribution is the suggestion of several recommendations including what requirements a commercial energy harvester should meet in order to gear up with the demands of the industries.

In chapter 4, the major contributions are to improve the presentation of the continuum model (also known as the distributed parameter model), and to introduce a generalised model for single mass piezoelectric cantilever beams. The presentation of the distributed parameter model has been improved by forming a single formulation for both series and parallel connection of the two piezoelectric layers. The introduced generalised model can be used as either a lumped-mass model or a continuum model by applying the appropriate term definitions. The flexibility of the generalised model accommodates different needs of a designer, and the further analysis on the generalised model can be applied to both models appeared in the literature. Other significant contributions are the analysis of the generalised model as a current source circuit, and the Thévenin equivalent circuit where the source impedance of the electromechanical system is derived. The analytical expression of the source

impedance has important implication on impedance matching and it reveals the fact that when electrical damping and mechanical damping are equal, the impedance of the electromechanical system is indeed matched, leading to maximum power output. Furthermore, excellent agreement is found between the model and experiments.

In chapter 5, the major contribution is the derivation of a continuum model for double-mass piezoelectric cantilever beams using Hamilton's principle. The analytical solution of the model is presented and the model is experimentally validated. To avoid charge cancellation for higher order vibration modes, the model provides ideal locations for electrode segmentation. Moreover, it is proposed to have a rectifier for each segment as a workable circuit for power optimisation. Majority of the material presented in this chapter is published in the Journal of Intelligent material systems and structures [24].

In chapter 6, the major contribution is the derivation of an improved continuum model for single and double-mass piezoelectric cantilever beams. Given that the existing continuum models yield unrealistic results for an impedance matched system, the improved model solves this problem by including the polarization losses of the piezoelectric material, and the ohmic losses of the electrode layers. The model is experimentally validated by a modulus matched system and a system with a bridge rectifier and a capacitive load. Other major contributions are to show the potential tuning range to be gained by impedance matching, and the analysis to show that the major challenges of realising an impedance matched system lie in the losses of inductor and piezoelectric materials. It details the procedure to obtain the requirements of electrical components for impedance matching and argues that with the continual advancement in manufacturing technologies and material science, an impedance matched system can become an attractive implementation for a self-tuning harvester.

In chapter 7, the major contributions are the two concepts proposed for resonance tuning by mechanical actuations. Based on the two concepts, four prototypes were designed and built. Their performances in terms of damping and tuning range were evaluated and possible improvements were provided. It has demonstrated that the conical spring concept can result in a practical harvester that produces more than 1 mW of power at less than 0.1 g of base acceleration in the frequency range 24 - 50 Hz. The prototype can automatically tune its resonance frequency by 10 % in every 24 minutes. A patent was produced for this tuning mechanism.

2

Literature Review

2.1 Vibration Characteristics

Vibration, as an ubiquitous energy source in the industry, holds a great promise to enable self-powered wireless sensors. This is evident from the increasing research interests of the subject in recent years. However, almost all research is focused on the modelling, design and optimisation of the harvesters, and the power conditioning circuits. Very little study has been done on the vibration source itself. Vibrations with diversifying characteristics present in the environment means it is difficult to design a harvester that generates a consistent power level. Hence, understanding the vibration characteristics of the intended application is vital to the design of an effective harvester. Roundy et al. [14] briefly investigated a few commonly available vibration sources. As summarised in Table 2.1, the results give an overview of the characteristics of vibration from many day-to-day items around us. From the results, it is not surprising to see that most household appliances have a peak vibration around one or two times of the line frequency (60 Hz in the U.S). This simple fact has led to a niche market for vibration-based energy harvesters resonating at 60 Hz or 120 Hz such as the product Joule-Theft™ from AdaptiveEnergy. However, the results also show vibration peaks at a wide range of frequencies, from 1 to 285 Hz. For these vibration sources pretuned commercial resonators will not work. Another highlight of the results is the large variation of the vibration accelerations across the sources. Since power is proportional to the acceleration squared, it can be challenging to design a harvester that generates adequate power for a wide range of accelerations. Based on the median values, Roundy et al. [14] used 2.25 m/s^2, the typical acceleration of a microwave oven, and 120 Hz, twice of line frequency, as the basis for the design of their vibration-based energy harvesters.

Table 2.1: Characteristics of vibration sources [25, 14].

Vibration source	A_{peak} (m/s^2)	F_{peak} (Hz)
Car engine compartment	12	200
Base of 3-axis machine tool	10	70
Kitchen blender casing	6.4	121
Clothes dryer	3.5	121
Person nervously tapping their heel	3	1
Car instrument panel	3	13
Door frame just as door closes	3	125
Small microwave oven	2.25	121
HVAC vents in office building	0.21.5	60
Wooden deck with foot traffic	1.3	385
Bread maker	1.03	121
Windows next to a busy road	0.7	100
Laptop while CD is being read	0.6	75
Washing machine	0.5	109
Second story floor of busy office	0.2	100
Refrigerator	0.1	240

2.2 Modelling of Piezoelectric Energy Harvesters

In the energy harvesting community, mathematical models and simulations play an important role for concept evaluation and designs. Widely used models for Lead Zirconate Titanate (PZT) harvesters include the lumped-mass models and the continuum-based models. Based on different assumptions, the accuracy and complexity of these models can vary significantly. A Cantilever is the simplest form of energy harvesters and it is also the fundamental structure whose theoretical derivation can be directly applied to structures with other boundary conditions. Therefore, the majority models developed are for PZT cantilevers. Lumped-mass models [26] are often employed as the first approach to estimate the system dynamics. A lumped-mass model evaluates the average stress and strain of a PZT cantilever based on static deflections. The current generated by the PZT is proportional to the strain developed, hence the output voltage for a resistive load is estimated according to circuit theory. Another variant of the lumped-mass model is the equivalent circuit model [27, 28, 29] that represents the spring-mass-damper system by a RLC circuit shown in Figure 2.1. This equivalent circuit approach is

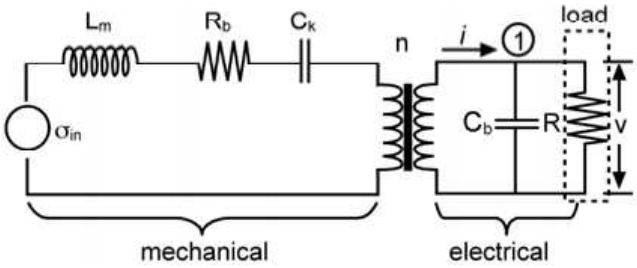

Figure 2.1: Equivalent circuit model of PZT cantilevers [27].

preferred by researchers with a strong electrical background. In the mechanical part, the inductor L_m, resistor R_b and capacitor C_k are the analogies of the proof mass, damping and spring elements, respectively. By linking the current to strain, and voltage to stress, the dynamics of the PZT cantilever is modelled by the circuit in the mechanical part. The transformer bridging the mechanical and electrical part represents the piezoelectric coupling effect. In the electrical part, the capacitor C_b is the piezoelectric capacitance, and R is the electrical load. The biggest advantage of the lumped-mass model is that its mathematical equations are so simple such that it can be easily solved by hand, yet the results capture most of the information of the dynamic systems. Furthermore, the equations of a lumped-mass model can be written into the state space form [27], which makes the model much more scalable when the PZT system is connected to a larger and more complicated electrical circuit. Figure 2.2 shows an experimental validation result of a lumped-mass model. It can be seen that the accuracy is adequate and there is certainly room for improvements [30]. The major drawback of lumped-mass models is that they can only predict the fundamental frequency of the system. Lumped-

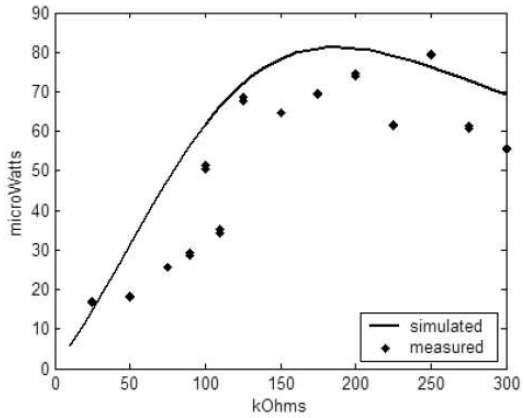

Figure 2.2: Experimental validation results for a lumped-mass model [25].

mass models are not able to predict the shift of the resonant frequency associated with the change of the electrical load. Continuum-based models are subsequently adopted for higher accuracy. Sodano et al. [31] developed an analytical model for a 2-layer PZT bender with no proof mass. From the results shown in Figure 2.3, the model has proven to be highly accurate. Continuum

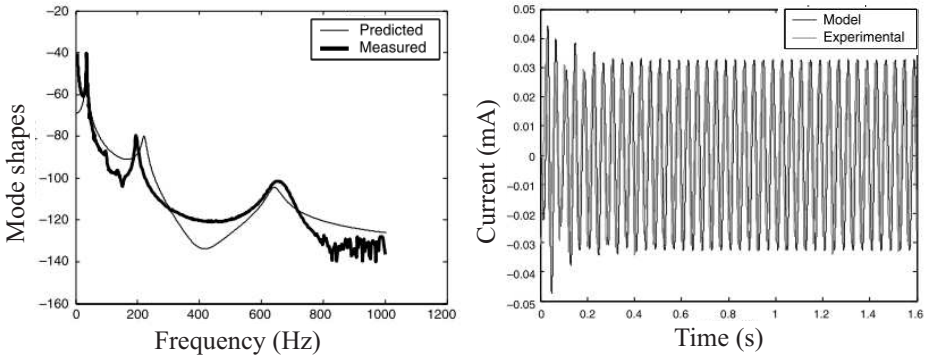

Figure 2.3: Experimental validation results for a continuum model of PZT cantilevers [31].

models are derived from variational method [32], such as Hamilton's principle [33]. Combining the Rayleigh-Ritz method and Euler-Bernoulli beam theory [34], the derived equations of motion have infinite many degrees of freedom and vibration modes. In energy harvesting applications, having at least one proof mass is advantageous, as it lowers the resonant frequency and increases the strain of the bender. A continuum-based model for a 2-layer PZT cantilever with a mass at the free end was developed by Erturk and Inman [35]. The addition of the end mass modified the eigenfunctions in the equations of motion. As can be seen in Figure 2.4, the modelling results show excellent agreement with experiment for the selected resistive loads. However, continuum models are only valid to a slender beam to adhere to the

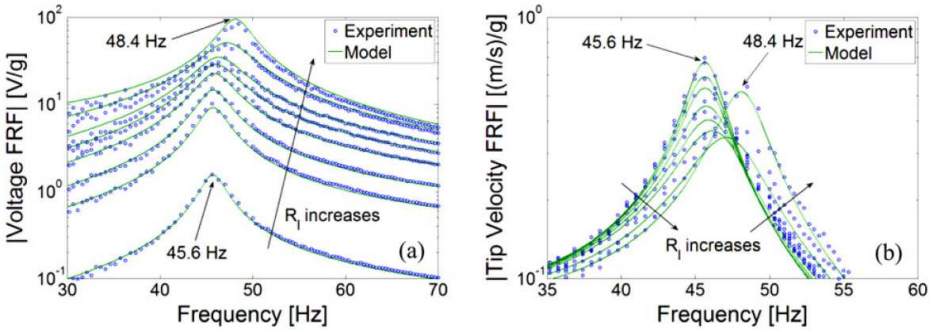

Figure 2.4: Experimental validation results for the distributed parameter model of a PZT cantilever with an end mass [35].

assumptions of the Euler-Bernoulli beam theory. The accuracy diminishes as the aspect ratio of the beam decreases. This problem can be overcome by applying plate theory. In addition to analytical modelling, Finite Element Method (FEM) is a popular implementation to model plate-type piezoelectric energy harvesters [36, 37]. Being flexible and sufficiently accurate, FEM is not necessarily bound by assumptions of the Euler-Bernoulli beam theory, and hence it can be quickly adapted for complex geometries. However, solving dynamic problems by FEM is a computationally intensive process. More importantly, FEM obscures the relationships between variables that can be otherwise observed in an analytical solution.

2.3 Techniques for a Wide Frequency Range Harvester

Despite the advancement made by research effort to optimise the power conditioning circuit and the PZT harvester geometries for power output at resonance, the fundamental problem of keeping the harvester in resonance in a wide frequency range is still unresolved. This problem alone greatly limits the commercial viability of vibration-base energy harvesters. For a normal resonator, one or two Hertz of deviation from the natural frequency is all it takes to result in dramatic power reduction. This problem gets worse when the quality factor of the resonator gets higher. Generally speaking there are two methods that can widen the frequency range of the harvester, namely wide bandwidth structures and resonance tuning. The typical frequency response of the two methods is illustrated in Figure 2.5 and 2.6. By adopting a wide bandwidth structure, such as a cantilever array, the harvester inherently exhibits broadband frequency response. It is the result of the dynamic property of the structure and no extra effort is needed to maintain this behaviour. On the other hand, resonance tuning refers to the method of shifting the resonant frequency of a narrow bandwidth resonator. This can be achieved mechanically by ways such as changing the length of the cantilever beam or the position of the proof mass. To eliminate moving parts for the tuning purposes, resonance tuning can also be implemented electrically by modulus or impedance matching. A plethora of concepts for broad-band and frequency tuning are reported in the Chapter 1 of [39]. The existing concepts for these methods are discussed in the following subsections.

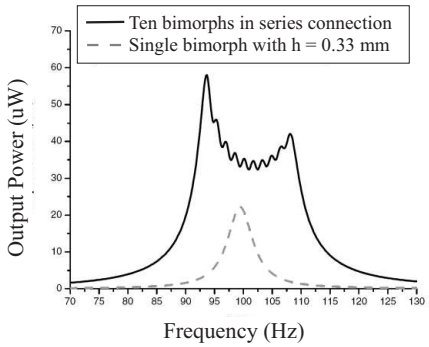

Figure 2.5: Wide bandwidth structure. A harvester made by an array of PZT cantilevers [38].

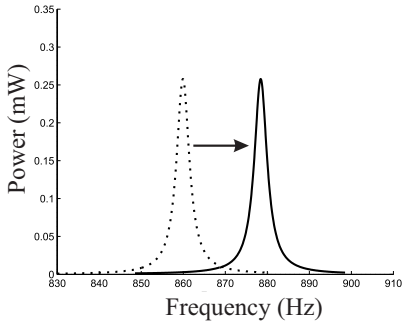

Figure 2.6: Shifting the resonant frequency of the harvester by changing its electrical and/or mechanical properties

2.3.1 Wide Bandwidth Structures

The existing concepts for wide bandwidth structures energy harvesters include cantilever arrays, multi-modal structures, the use of stoppers and nonlinear techniques. Figure 2.7 illustrated an example of a PZT cantilever ar-

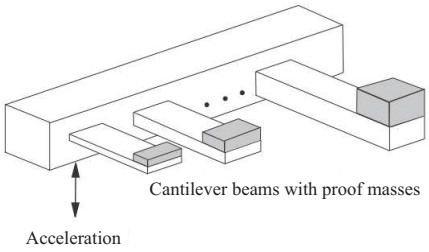

Figure 2.7: A wide bandwidth energy harvester implemented by a PZT cantilever array [40].

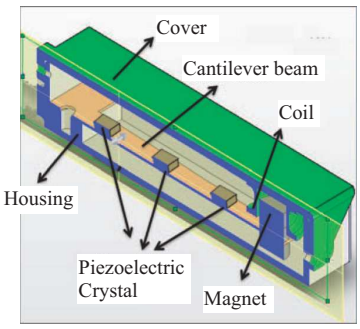

Figure 2.8: A wide bandwidth energy harvester implemented by a multi-modal structure [41].

ray. Extensive study and prototyping on this type of harvester was done by many researchers [38, 40, 21]. The effectiveness of this concept towards wide bandwidth is unquestionable. However, on the premise of a rigid common base, only one cantilever beam in the array is resonating for a given excitation frequency, leaving the rest of the beams under utilised. As a result, the power density of such a harvester tends to be low. Another commonly used structure that exhibits wide bandwidth is the multi-modal structure, which is also studied extensively [29, 41, 24, 42, 43, 44, 45]. The typical way to

implement a multi-modal structure is mounting multiple proof masses on a beam. An example of a multi-modal harvester is shown in Figure 2.8. Due to the high vibration modes from the beam, the utilisation of the proof mass is improved in multi-modal energy harvesters.

Instead of adding more masses or more beams to the harvester, wide bandwidth structure can also be realised by having a stopper on a single mass beam. One example is the configuration illustrated in Figure 2.9, where a

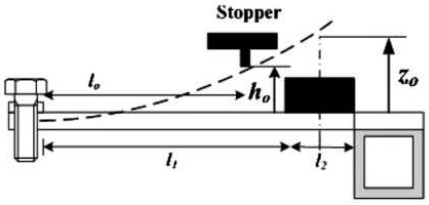

Figure 2.9: A wide bandwidth energy harvester by the use of a stopper [46].

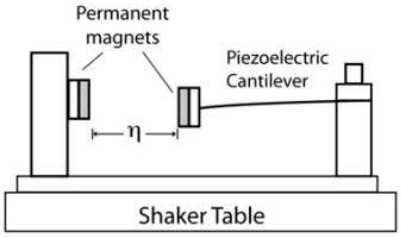

Figure 2.10: A wide bandwidth energy harvester by the use of magnets [47].

stopper is added on the vibrating path of the beam [46, 48]. Once the beam hits the stopper, the free section of the beam continues to deflect, disrupting the original vibrating pattern. Instead of exciting the beam at resonance, the key of this approach is to assure the beam to get in contact with the stopper. In other words, this approach relies on a minimum displacement and hence it is amplitude dependent. The bandwidth gets wider as the acceleration of the beam is higher, and vice versa.

Another approach for wide bandwidth structures is by the use of magnetic forces. As illustrated in Figure 2.10, an external magnet is placed in close proximity to the magnet on the proof mass. Similar configurations are used by other researchers [47, 49, 50]. As the proof mass vibrates, the non-linearly changing magnetic force alters the overall stiffness of the cantilever system, hence it results in a broadband frequency response. The higher the amplitude, the larger the stiffness variation, thus the bandwidth is amplitude dependant.

A variant of the approach above is a bistable set-up that also exploits the non-linear interaction of the magnetic force as the beam vibrates [51, 52, 53]. The difference is that the non-linear behaviour resulted in this approach renders the vibrating beam unstable and constantly jumping between two quasi-stable positions.

Last but not least, wide bandwidth structures can also be implemented by completely taking the advantage of the non-linearity characteristics exhibits in all piezoelectric materials [54, 55]. As the response of the piezoelectric cantilever exceeds a certain threshold, the dynamics become stochastic due to the soften/hardening property of piezoelectric materials. However, the bandwidth obtained by this approach not only depends on the amplitude of the cantilever response, but also depends on the direction where the excitation frequency is swept. Unfortunately it is impractical to control the vibration source in the real world, therefore none of these conditions can be reliably obtained for the harvester.

2.3.2 Resonance Tuning by Electrical circuits

For piezoelectric harvesters, resonance tuning can be realised through an electrical circuit. Essentially it utilises the piezoelectric beam as an actuator as well as a harvester. The biggest advantage of electrical tuning is the absent of moving parts for the tuning purpose, which greatly simplifies the mechanical design and increases the reliability against wear. Controlling the Stiffness by switching the piezoelectric element on for a brief time period each time when the deflection crosses a zero value is demonstrated by Lallart et al. [56]. Another most common approach to shift the resonant frequency of a piezoelectric beam is by impedance matching, which matches the impedance of the electrical to the overall impedance of the piezoelectric beam for all frequencies. There are two types of impedance matching, namely, modulus matching [57] and conjugate matching [58, 59]. The former is to match the modulus of the source impedance by a variable resistive load, while the latter is to match the source impedance completely using a complex load. Kong et al. [57] has designed a circuit that automatically matches the modulus of the load to that of the piezoelectric beam. The harvested power and the dissipated power by the control circuit is shown in Figure 2.11. Taken the losses of the control circuit into account, the system is able to retain about 58 to 72 % of the available power extracted by the optimal resistive loads. The dominant losses are the conduction loss of the diode and the inductor of the circuit. Nonetheless it has proven that the frequency range of a modulus matched system can be extended compared with a system with a fixed resistive load. Theoretically, an impedance matched system can further extend the frequency range. C. Luo and H.F. Hofmann [59] have demonstrated the viability of impedance matching with an active tuning technique, where the impedance was matched by applying a sinusoidal voltage on the piezoelectric beam to emulate an load impedance. Search algorithm was employed to

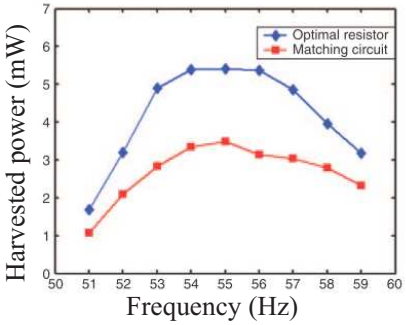

Figure 2.11: Frequency tuning by modulus matching [57].

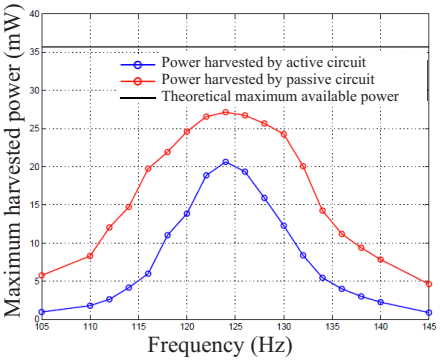

Figure 2.12: Frequency tuning by active impedance matching [59].

find the optimal phase angle and voltage magnitude of the applied voltage. From the results showing in Figure 2.12, they suggested that theoretically an impedance matched system can give a maximum and constant power output at all frequencies. Due to losses, the actual power harvested by impedance matching is diminishing as the driving frequency drifting away from the natural frequency. However, an improvement on frequency range of an impedance matched system over that of a passive system is evident in their experimental results.

2.3.3 Resonance Tuning by Mechanical Actuation

By altering the effective spring stiffness of the cantilever beam, the resonant frequency can be tuned to match the driving frequency. Compared to wide bandwidth structures that involved multiple proof masses, resonance tuning is usually concentrated on a single proof mass. Furthermore, resonance tuning allows the mechanical damping to be reduced (hence improves power output) without being penalised in the effective frequency bandwidth. The tuning method can be classified into the following three categories.

Passive tuning

Passive tuning refers to a vibration harvester whose natural frequency can be tuned manually by an operator. Passive tuning allows the harvester to be pre-tuned before installation. Although additional mechanism is required to achieve the tuning, it is very effective for vibration source that has little change on its dominant frequency over time. Several mechanisms have been

presented in the literature to achieve passive tuning [60, 61, 62, 63]. In Figure 2.13, a concept to change the resonance frequency of the beam by applying a pre-load compressive force is illustrated. As the beam gets compressed, the stiffness of the beam changed, hence the resonant frequency of the beam gets modified. For this concept, a frequency range of 200 - 250 Hz was

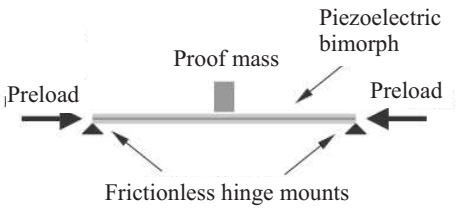

Figure 2.13: Resonance tuning by compressive axial pre-load [60].

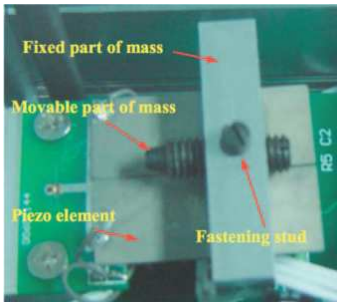

Figure 2.14: Resonance tuning by shifting the proof mass [61].

demonstrated on a prototype. The frequency range is limited by the amount of compression can be applied before buckling occurs. Figure 2.14 shows a prototype of a harvester tuned by shifting the position of its proof mass. By manually turning the screw (labelled in figure as movable part of mass), the centre of mass of the proof mass is shifted with respect to the fixed piezoelectric element. Hence the resonant frequency gets modified. This prototype demonstrated a tunable frequency range of 130 - 180 Hz. While this approach seems effective to frequency tuning, it can potentially have high mechanical damping due to the looseness between the screw and the mass. High mechanical damping can greatly reduced power output even the harvester is driven at resonance. To minimise mechanical damping, all the moveable parts involved in the tuning mechanism can be tighten or spring loaded.

Semi-active tuning

Semi-active tuning refers to a vibration harvester that tunes its natural frequency in response to a command signal. This tuning strategy takes the advantage of active tuning, and yet minimises the power dissipation. Hence it is the best balance between automatic tuning and control effort. Although semi-active tuning shows promising to solve the narrow band problem, relatively few prototypes have been demonstrated in the search community. By using additional piezoelectric beams as actuators, two prototypes [64, 65]

have been demonstrated. As a DC voltage is applied on the piezoelectric actuators, the bending of the beam alters the overall stiffness of the system, yielding a resonant frequency shift. The amount of frequency shift is controlled by the level of DC voltage applied to the actuators. Eichhorn et al. demonstrated the viability of this concept by the design shown in Figure 2.15. For a range of applied voltage from -30 V to +45 V, the harvester

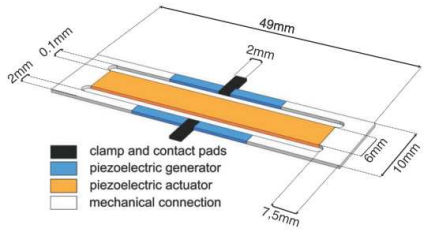

Figure 2.15: Semi-active tuning energy harvester. [64].

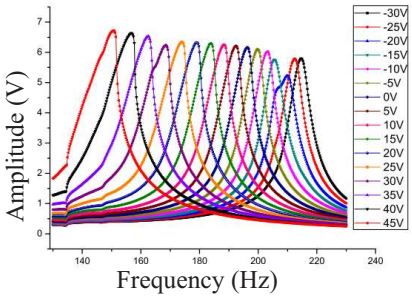

Figure 2.16: Response for different actuating voltages at 0.6 g acceleration amplitude. [64].

exhibits a resonant frequency shift from 150 to 190 Hz as shown in Figure 2.16. It is evident that the mechanism is quite effective in frequency tuning. The challenge of this approach is to generate the required negative voltage in the harvester. It could also be difficult to generate the relatively high voltage required for tuning, and the high control voltage can potentially result in relatively high losses.

Active tuning

Active tuning or self-tuning refers to vibration harvester that continuously tunes its natural frequency for optimal performance. (i.e. closed-loop control and continuously dissipating energy). Not only does this method add considerable complexity to the system, but also the energy gained over the energy spent on tuning needs justifying. Roundy [26] has established a mathematical proof to show that as long as the second-order mechanical system models the energy generator reasonably well, active tuning will never improve power output.

3

Machine Vibration Characteristics

3.1 Introduction

Common sources of vibration including human body, structures and machinery can have large variations on characteristics. A harvester that is capable of generating adequate power from all of these sources would most likely be inefficient, if possible at all. Therefore, understanding the characteristics of the source vibration where the harvester is intended for use is vital to the design of an efficient harvester. Generally speaking, machine vibrations are of low amplitude, strong force and high frequency compared to the vibrations of human body and structures. In the literature much effort is put on modelling and concept evaluation of energy harvesters. The only investigation on vibrations for the purpose of energy harvesting was done by Roundy et al. [25, 14], who carried out brief measurement on structures, and general day-to-day items and home appliances. Subsequently they used 2.25 m/s^2, the acceleration found in a microwave oven, as the basis to design their harvesters. To design an effective harvester for machine condition monitoring, a more thorough investigation on machine vibrations from an energy harvesting perspective is needed. In this chapter 15586 vibration recordings from 511 industrial machines are studied. The results provide valuable insight into the amplitudes and frequency distribution of machine vibrations, which sheds light on the minimum proof mass and optimal frequency range required for the harvester. It reveals that compared to the acceleration 2.25 m/s^2 used by Roundy et al., vibrations found in machinery are of much lower amplitudes. The findings serve as a valuable reference for the design of vibration-based energy harvesters.

This chapter is organised as follows. In Section 3.2, the theoretical maximum power output is derived, and the reason of choosing acceleration instead

of velocity or displacement as input is explained. Section 3.3 presents the statistical results of the investigated machine vibrations, and identifies the minimum proof mass to generate 500 μW power output. Section 3.4 discusses the key findings and gives a few recommendations to the design of energy harvesters. Conclusions are given in Section 3.5.

3.2 Theoretical Maximum of Power Transfer

Harvesting energy from machine vibrations is essentially a transduction and energy transfer process. As the energy harvester undergoes cyclical base excitation, its proof mass oscillates at the same frequency for a linear dynamical system with small displacement. At steady state, the energy stored in the oscillation of the proof mass is the *total* amount of energy available for extraction. The majority of this energy stays within the oscillating system in the form of kinetic and potential energy, respectively, and only a fraction of this energy leaves the system as dictated by mechanical and electrical damping. Generally the proof mass is much smaller compared to the mass of the vibrating machine, hence it is often assumed that the damping effects of the proof mass has negligible influence to the host machine. In other words, for a given vibration amplitude and frequency, the *total* energy available for harvesting is solely dependent on the weight of the proof mass. A secondary conversion stage is to convert the energy stored in the proof mass to electrical energy. Common technologies make use of electromagnetic, electrostatic and piezoelectric transducers. Despite the differences in converting mechanisms, fundamentally they all introduce electrical damping to the proof mass as a way of energy extraction. The energy transfer process can be generalized by a mass-spring-damper system illustrated in Figure 3.1, where the dampers have mechanical and electrical damping constants C_m and C_e, respectively. When subject to vibration, only the energy absorbed by the electrical damper will be converted to electrical energy. The energy absorbed by the mechanical damper constitutes losses. The equation of motion that describes *absolute* displacement of the proof mass $x(t)$ for the input displacement $y(t)$ can be written as

$$m\ddot{x}(t) + (c_m + c_e)\Big[\dot{x}(t) - \dot{y}(t)\Big] + k\Big[x(t) - y(t)\Big] = 0. \tag{3.1}$$

Under harmonic excitation, the base displacement can be represented by a sinusoidal function $y(t) = Y_0 \sin(\omega t)$, where Y_0 and ω are the input amplitude and angular frequency, respectively. Besides, it is more common to express the results in terms of damping ratios ξ_m, ξ_e and ξ_T and natural

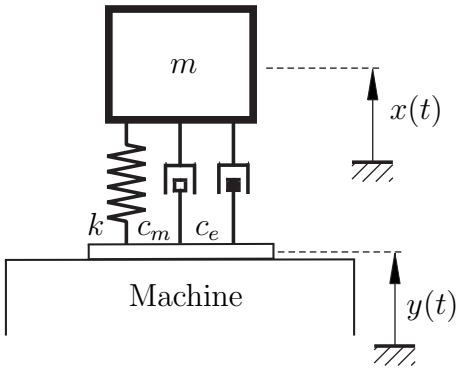

Figure 3.1: Mass spring damper system.

frequency ω_n instead of damping constant c_m and c_e and spring constant k. The relationship among these parameters are

$$c_m = 2\xi_m\omega_n m,\ c_e = 2\xi_e\omega_n m,\ \xi_T = \xi_m + \xi_e,\ k = m\omega_n^2, \tag{3.2}$$

Denoting $z(t) = x(t) - y(t)$ as the *relative* displacement of the proof mass to base, the response of the proof mass in the frequency domain can be written as:

$$Z(\omega) = \frac{\omega^2}{-\omega^2 + 2\xi_T\omega_n\omega j + \omega_n^2}Y_0, \quad \forall\,(\xi_T \neq 0 \wedge \omega \neq \omega_n). \tag{3.3}$$

The energy absorbed by the electrical damper is the product of the electrical damping force $c_e\dot{z}(t)$ and the relative velocity of the mass $\dot{z}(t)$. This gives the power output in the frequency domain as

$$P_y(\omega) = c_e|\dot{Z}(\omega)|^2. \tag{3.4}$$

The subscript y indicates that the power corresponds to a constant input displacement Y_0. Substituting (3.3) into (3.4), it yields

$$P_y(\omega) = \frac{2m\xi_e\Big(\dfrac{\omega}{\omega_n}\Big)^6\omega_n^3}{\Big[1-\Big(\dfrac{\omega}{\omega_n}\Big)^2\Big]^2 + \Big[2\xi_T\Big(\dfrac{\omega}{\omega_n}\Big)\Big]^2}Y_0^2, \tag{3.5}$$

which is also obtained by other research groups [15, 66, 23]. Note that there are two interpretations on the unit of the power P_y and the input Y_0 in (3.5). While the input is the amplitude of a sinusoidal waveform, P_y is the peak power, whereas if the input is the *rms* value, then P_y is the *average* power. The latter is used throughout this article because vibrations are often described in terms of *rms* in the industry. It is well-known from the

basics of dynamics that when damping is present, the resonant frequency is not necessarily equal to the natural frequency of the system. It is not so well known that, for a damped system, the choice of input quantity (being held constant) also influences the resonant frequency. In (3.5), a constant input displacement Y_0 is applied for all frequencies ω. However, if velocity or acceleration are held constant, the expressions of the power outputs become

$$P_v(\omega) = \frac{2m\xi_e\left(\frac{\omega}{\omega_n}\right)^4\omega_n}{\left[1-\left(\frac{\omega}{\omega_n}\right)^2\right]^2+\left[2\xi_T\left(\frac{\omega}{\omega_n}\right)\right]^2}V_0^2, \tag{3.6}$$

for a constant input velocity V_0 and

$$P_a(\omega) = \frac{2m\xi_e\left(\frac{\omega}{\omega_n}\right)^2\frac{1}{\omega_n}}{\left[1-\left(\frac{\omega}{\omega_n}\right)^2\right]^2+\left[2\xi_T\left(\frac{\omega}{\omega_n}\right)\right]^2}A_0^2, \tag{3.7}$$

for a constant input acceleration A_0. Figure 3.2 shows how the differences of input quantity influence the optimal frequency for maximum power transfer.

By applying the standard differentiation technique, the optimal frequency

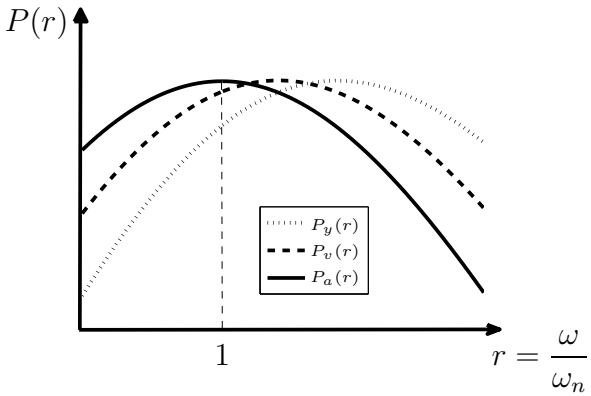

Figure 3.2: Optimal frequency depends on the input quantity that is held constant.

for each of the power expression can be determined analytically, which are summarized in Table 3.1. The analysis here shows that when input acceleration is held constant, the resonant and natural frequencies are identical, and it yields a much simplified expression for power output. Therefore, vibration levels are preferred to be described in terms of acceleration for the proceeding studies.

Table 3.1: Summary of optimal frequency for different input quantities.

Power function	Optimal angular frequency ω_{opt}
$P_y(\omega)$	$\omega_n \left((2 - 4\xi_T^2) - \sqrt{(4\xi_T^2 - 2)^2 - 3} \right)^{\frac{1}{2}}$
$P_v(\omega)$	$\omega_n \left(1 - 2\xi_T^2\right)^{-\frac{1}{2}}$
$P_a(\omega)$	ω_n

The extracted electrical power is maximum when the electrical damping is equal to mechanical damping ($\xi_e = \xi_m = \xi$), which leads to the theoretical maximum power at resonance,

$$P_{a,max}(\omega) = \frac{m}{8\xi} \frac{A_0^2}{\omega}. \tag{3.8}$$

As elaborated by Stephen [67], it is wrong to conclude in (3.8) that $P_{a,max} \to \infty$ as $\xi \to 0$. The power output expression is invalid since the conditions stated in (3.3) are violated. In the absence of damping, no power will be dissipated or absorbed for $\omega \neq \omega_n$, and steady state does not exist at resonance. On the other hand, $P_{a,max} \to \infty$ as $\xi \to \infty$ being suggested in (3.4) is equally invalid because a system with large damping will have very little displacement and velocity, hence the power dissipated is small. The expression of power output in (3.8) is deliberately separated into the product of two fractions. The first contains the parameters that we have control over as to how the harvester is designed, and the other contains parameters of the vibration source, for which we have to adapt. It is convenient to define this fraction as *power transmission factor*

$$\kappa_{pt} = \frac{A_0^2}{\omega}. \tag{3.9}$$

This factor implies that over the spectrum of a vibration recording, maximum power does not necessarily occur at the frequency of maximum acceleration, but rather at the frequency where the ratio of A_0^2 and ω is the greatest. On the other hand, the parameters that we have control over are the amount of proof mass used and the mechanical damping, while implicitly assuming that we have the absolute control of electrical damping and that has been set to optimum. Between the two parameters, the mechanical damping is equally rewarding in gaining power output. In practice, however, mechanical damping is very hard to control and it requires highly consistent manufacturing process in place. Furthermore, a very small mechanical damping renders a system of very narrow bandwidth, which makes it more frequency sensitive

and hence harder to be tuned to resonance. For a tuned harvester, the easiest and most cost effective way to raise the "ceiling" for power extraction is to increase the proof mass. To determine the minimum proof mass, we have to know the typical κ_{pt} among industrial machinery. It is also worth knowing the range and distribution of the optimal frequencies of machine vibrations. Hence the harvester can be designed to work optimally in that frequency range.

3.3 Data Analysis and Statistical Results

3.3.1 Data acquisition of machine vibrations

The majority of machinery in the industry are rotating machines, and some of which are fixed-speed drive. The spectrum of a fixed-speed machine will therefore have a peak at the main power frequency, which is either 50 or 60 Hz in most countries. However, this information alone is not sufficient to determine the most favourable frequency for energy harvesting. As mentioned before, the most favourable frequency is not necessarily the frequency with the greatest amplitude, but the frequency where κ_{pt} is the greatest. This is especially true for machines that have multiple peaks in their spectrum recordings, such as fans. Furthermore, as a future trend more and more machines will adopt variable speed drives to bolster power efficiency. In addition to the operating frequency, it is equally important to have a general view of the vibration levels, which can vary considerably from large to small machines, and from the same machine in different loading conditions. Figure 3.3 shows a machine being monitored by a dual-axis accelerometer wireless sensor. Common places to sample vibrations are the bearing housing of a machine's drive and non-drive ends for the prediction of bearing failures. The sampled vibration data is presented in a time waveform or an FFT spectrum for analysis. Figure 3.4 shows a typical vibration spectrum recording from an industrial cooling fan. A couple of observations can be made from this typical recording. First, there can be many peaks with comparable amplitudes present in the spectrum. Second, the amplitude at 50 Hz is not necessarily the highest peak even the machine is driven at 50 Hz. A comprehensive survey on spectrum recordings measured from industrial machines can provide valuable insights into the overall vibration characteristics. A database containing a total number of 15586 spectrum recordings from 511 machines in 3 companies is studied. The surveyed machines include cooling fans, heater fans, air compressors, oil circulating, hydraulic and water pumps, convey-

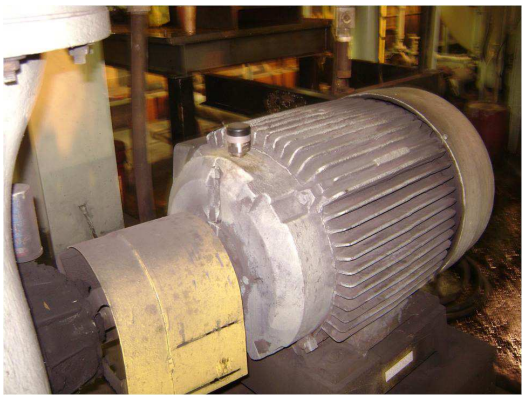

Figure 3.3: A dual-axis accelerometer wireless sensor measures the vibration of a machine drive-end. Photo was provided by GE Energy Ltd.

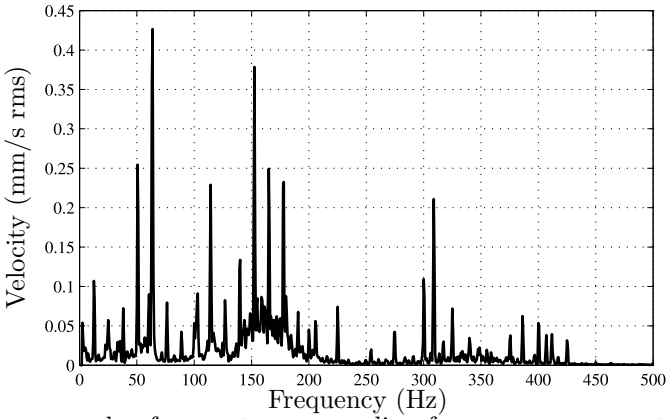

Figure 3.4: An example of a spectrum recording from an energy centre primary air fan motor drive-end, vertical axis, on 04/03/2008 2:31:03pm.

ors, sanders, crushers, grinders, agitators, gearboxes and other equipment in wind turbines. They should give a good representation of machines used in most industries. Each machine may have multiple measuring locations, and for each location several measurements may have been taken over time. To reduce bias, the maximum number of recordings for the same location is limited to 10. A program written in C# is used to extract the data from the SQL database, and save it in XML format. Matlab® is used to analyse the data and visualize the results.

3.3.2 Frequency characteristics

The knowledge on the dominant frequency is useful for designing narrow band harvesters, whereas the most favourable frequency range is of interest

to those who design wide bandwidth or tunable harvesters. The optimal frequency is defined as the frequency where κ_{pt} is the greatest. Harvesters resonate at the optimal frequency absorb the most energy from the source vibration. By analysing all the spectrum recordings in the database, Figure 3.5 shows how the optimal frequencies are distributed.

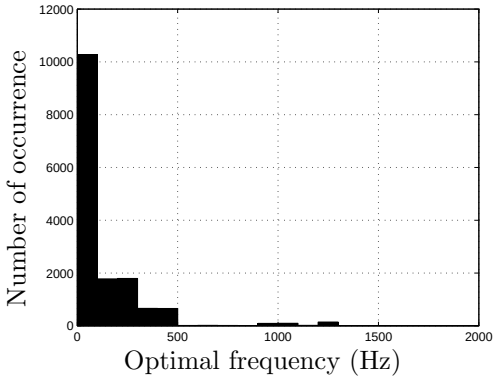

Figure 3.5: Optimal frequency occurrence below 2000 Hz.

The result turns out that over 97 % of the optimal frequencies are below 500 Hz. Figure 3.6 is a close-up view of the optimal frequencies under 500 Hz, which provides further detail on the distribution of the low frequencies. Since the machines are running on a 50 Hz power supply, the high vibrations concentrating around 50 Hz and 100 Hz have taken a fair share as expected. However, the single most dominant frequency is actually around the sub-

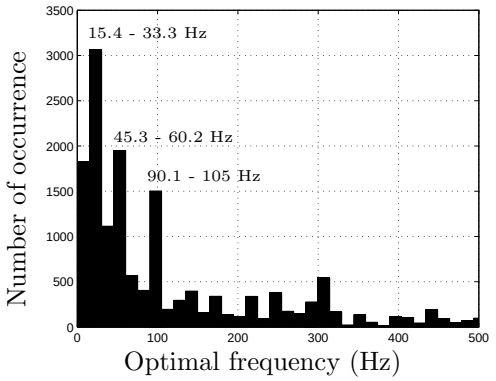

Figure 3.6: Optimal frequency occurrence below 500 Hz.

harmonic of the main frequency, i.e. 25 Hz, which accounts for about 13 % of all the recordings. These machines are likely to be driven by 2-pole induction motors, which turn at a speed slightly below half of line frequency.

Of equally noticeable is the significant share of frequencies below 15.4 Hz. The majority of these low frequencies come from wind turbines. For a typical three-blade wind turbine rotating at 16 RPM, the vibration of the main bearing is measured at 48 RPM or 0.8 Hz. Vibrations in many of the wind turbine gearboxes also have peaks below 8 Hz. As far as the range is concerned, it shows that substantial amounts of the optimal frequencies are at 100 Hz or below. Assuming a harvester can be made tunable, either at a very narrow range (±2 %) or a wide range, Table 3.2 summaries the percentage of recordings the harvester can operate at the optimal frequency. With

Table 3.2: Statistics on the optimal frequency between selected ranges.

Frequency range (Hz)	(±%)	Recordings (%)
Tunable: narrow range		
24.3 - 25.3	2	9.2
48.6 - 50.6	2	9.1
98 - 102	2	7.9
Tunable: wide range		
0.7- 14	90.5	11.3
11 - 26	40.5	20.0
22 - 52	40.5	32.8
47 - 102	37.0	26.7
22 - 102	64.5	50.0
11 - 102	80.5	58.0

additional circuitry, the resonant frequency of a piezoelectric harvester can be tuned electrically within a small range, one of the techniques is modulus matching [57]. Tuning for a wide range, however, usually involves mechanical means such as some of the concepts summarized by Tang et al. [68]. Table 3.2 shows that the share for the three most popular narrow bands 25, 50 and 100 Hz are quite comparable. Interestingly if an electrically tunable harvester that resonates at all of these three discrete frequencies, the chances of it operating optimally will be more than 26 %, outperforming a wide range harvesters of 0.7 - 14 Hz and 11 - 26 Hz. Existing mechanical configurations for discrete frequency resonators are cantilever arrays [21] and a cantilever with multiple proof masses [24, 44].

3.3.3 Amplitude characteristics

Having the knowledge of the expected range of the source acceleration level helps make critical design decisions for an energy harvester. The lower acceleration limit allows designers to impose the minimum power rating of the harvester, whereas the higher acceleration limit gives references to the extent of robustness the harvester required. From the energy harvesting perspective, instead of looking at the acceleration distribution, a more informative presentation is to show the percentage of recordings that exceeds a certain *rms* acceleration level. The result is shown in Figure 3.7. For different

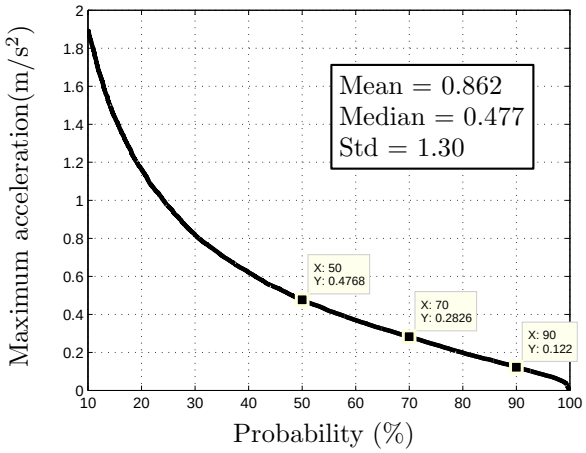

Figure 3.7: Statistics on maximum accelerations. It shows 50 % of recordings have an acceleration of 0.4768 m/s^2 or higher.

harvester designs, there may be constraints on velocity and displacement, therefore the information for these two quantities are also gathered at the same way as Fig. 3.7 and presented in Table 3.3 alongside with the acceleration values. The statistics of all three quantities have a similar pattern, where the standard deviation is much higher than the mean value. This indicates a fairly wide spread of vibration amplitudes. Due to the great deal of variance in the data set, median should be used in place of the mean value as the representative value. The velocity column can be used for a quick assessment of the credibility of the all results. Velocity in mm/s are generally used by professional vibration analysts. The median velocity of 1.108 mm/s falls within what experienced vibration analysts refer to as a normal vibration level, which is between 1 to 3 mm/s. More over, the results show about 80 % of the maximum velocities are less than 3 mm/s. A machine whose vibration falls within this range can be confidently considered to be in good working condition. Lastly, the table also shows the highest 1 % quantities,

Table 3.3: Statistics for maximum acceleration, velocity and displacement.

Recordings (%)	Acc. (m/s^2 rms) *exceeding*	Vel. (mm/s rms) *exceeding*	Disp. (μm rms) *exceeding*
90	0.122	0.322	2.613
80	0.199	0.476	3.658
70	0.283	0.642	5.011
60	0.369	0.840	6.887
50	0.477	1.108	9.647
20	1.164	2.943	31.300
1	5.963	22.320	$2.047e^3$

which give indication on how violent the harvester can be experiencing continuously. The highest 1 % acceleration, velocity and displacement are found in a frequency range of 3 - 2000 Hz, 1 - 50 Hz and 0.8 - 4 Hz, respectively. The extreme cases recorded are 28 m/s^2 at 1248 Hz, 511 mm/s at 3.75 Hz and 22 mm at 3.75 Hz. They are from a chip screen conveyor and a sump pump in a cleaner flotation area.

3.3.4 Minimum proof mass and frequency range

For any design of energy harvester, there is a targeted power output. Although mechanical damping is inversely proportional to power output, it is unrealistic to design a harvester to a precise damping ratio. This is because variation in mechanical damping is not only due to manufacturing tolerance, but also due to environmental conditions such as temperature, air pressure and humidity. From experiments we performed, it was observed that the damping measured in the morning can be as much as 15 % higher than it was at night for exactly the same set-up. The mechanical damping ratio was found to be typically between 0.005 to 0.02, which is consistent with the results found by Roundy [14]. Once the mechanical damping range of a certain design is identified and electrical damping is tuned to optimal, the proof mass has to be sized correctly to meet the required power output. From (3.8), the required proof mass depends on the value κ_{pt} of the vibration source. Figure 3.8 shows the statistics of κ_{pt} for all recordings. Similarly the large discrepancy between mean and median and a very high standard deviation suggest the median value is much more representative to the overall data set. In the scenario where the harvester can be always tuned to resonance, to generate 500 μW at 0.01 damping, Table 3.4 summaries the required proof mass to

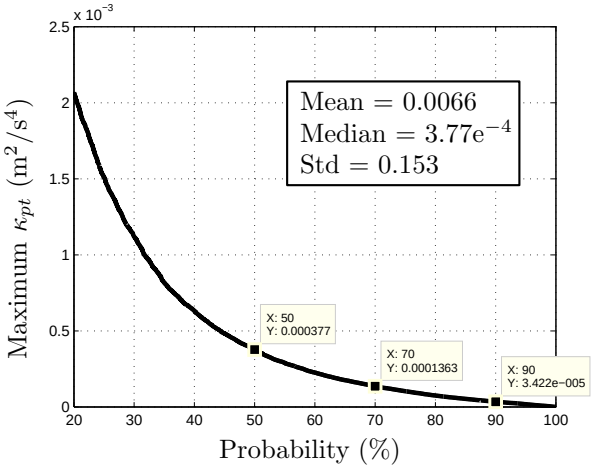

Figure 3.8: Statistics on κ_{pt} shows 50 % of recordings have a κ_{pt} value of 3.77e^{-4} m^2/s^4 or higher.

fulfil the corresponding percentage of recordings or machines. It is interest-

Table 3.4: Minimum mass required for 500 μW power output with $\xi_m = 0.01$, assuming the harvester has an infinite tuning range.

Recordings (%)	$\kappa_{pt} \times 10^{-4}$(m^2/s^4) *exceeding*	Minimum mass (g)
90	0.34	1170
80	0.75	534
70	1.36	293
60	2.26	178
50	3.77	106
1	267	1.5

ing to see that, to guarantee a power output of 500 μW even in 80 % of the sampled machines, a proof mass of 534 g is needed. Apparently there are some machines that have too little vibration to be scavenged. If we can further exclude 10 % of these machines, the required proof mass is nearly dropped by half, and it continues to decrease as we target only the machines with high levels of vibration. For harvesters being only deployed to the highest 1 % vibrations, the proof mass needed is as little as 1.5 g, which can be comfortably made into MEMS.

The results in Table 3.2 and 3.4 assume a harvester with an infinite proof mass operating at the optimal frequency and a specified mass operating at

an infinite frequency range, respectively. However, in reality neither of these assumptions can be true. For each recording, other than the optimal frequency, there could be other peak frequencies that are able to deliver the required power, as long as the proof mass is large enough for the given vibration amplitude. So the next questions to ask are: what proof mass and what tunable frequency range must the harvester have? The answers are summarized in Table 3.5, where it shows the percentage of recordings that would generate adequate power at each of the promising frequency range for the corresponding proof mass.

Table 3.5: Percentage of recordings where the harvester can generate 500 μW at mechanical damping ratio $\xi_m = 0.01$.

Frequency range (Hz)	(± %)	Recordings generate enough power (%) m = 200 g	m = 250 g	m = 300 g	Figure of merit
Tunable: narrow range					
24.3 - 25.3	2	12.8	14.4	15.7	7.15
48.6 - 50.6	2	9.8	10.8	11.8	5.40
98 - 102	2	8.9	10.4	11.8	5.18
Tunable: wide range					
0.7 - 14	90.5	10.9	11.7	12.5	0.13
11 - 26	40.5	20.5	23.0	25.0	0.56
22 - 52	40.5	31.2	34.5	37.3	0.85
47 - 102	37.0	27.7	30.6	33.1	0.82
22 - 102	64.5	41.2	45.3	48.3	0.70
11 - 102	80.5	44.3	48.7	52.0	0.60

The figure of merit (FoM) is defined as

$$\text{FoM} = \frac{\text{Average \% of recordings at m = 200, 250, 300 g}}{\text{Frequency range in } \pm\,\%}. \tag{3.10}$$

Note that unlike Table 3.2, the results shown in Table 3.5 may be overlapped by the same recording for a different frequency band, since some recordings may have multiple frequencies that can generate adequate power. The second column of Table 3.5 shows the frequency range in ± % of the central frequency. In general, the higher the frequency variation in percentage the bulkier and more expensive the harvester tends to be. Hence the FoM can be understood as the ratio of the likelihood of the harvester will work to the complexity of the harvester. Not surprisingly the narrow band frequencies dominate the FoM, setting 24.3 - 25.3 Hz the most rewarding frequency

range. As the harvester become a wide range, the law of diminishing return immediately applies. Nonetheless the best ranges are 22 - 52 Hz and 47 - 102 Hz. A lesser encouraging message from this table is that a very wide band (11 - 102 Hz) tunable harvester with a proof mass of 300 g would be needed to just satisfy over half of all the recordings or machines.

3.4 Discussions and Recommendations on Energy Harvester Design

The statistics suggest vibration amplitudes are generally very small at typical measuring locations and axes of industrial machinery. It is an order of magnitude smaller than the vibration from a small microwave oven, 2.5 m/s^2, that Roundy [14] based on to evaluate his harvesters. The small amplitude comes with no surprise because the majority of sensors are placed on bearing housings, and bearings serve as a fixed node of a rotating shaft. The surveyed database includes measurement of vibrations from 3-axis of machines: axial (front to end), vertical (up and down) and lateral (side to side). For a horizontally mounted machine, the vibration deflection is generally the greatest at the lateral direction [69]. One way to obtain the highest level of vibration from the machine is to place the harvester on the machine casing where the vibration is the greatest, and supply power with wiring to the nearby wireless sensors [69]. Although this strategy increases the likelihood of generating enough power from a machine, the required installation effort makes such a product less attractive than a wireless sensor that has its own built-in energy harvester. To keep the proof mass practically small, it makes more economical sense to position the energy harvester as a product only for machines with moderate amount of vibrations. The bottom 30 % of machines with the lowest vibration levels are typically cooling fans and oil circulating pumps. For such low vibration equipment, alternative energy source should be considered for self-powered sensors. In addition, the results suggest that MEMS harvesters have very little chance to generate enough power from machine vibrations due to its limited proof mass. Exceptions for this are when the required power is a few order of magnitudes smaller than 500 μW or the harvester is only used on specific machines where much higher vibration is available.

A wide bandwidth harvester is a huge step forward compared to a narrow band one in terms of costs, size, complexity, development and testing effort. Based on Table 3.5, judicious decisions can be made whether a wide

bandwidth harvester is necessary or it is sufficient to have different narrow band harvesters to suit different kinds of machinery. The noticeable share of 25 Hz vibrations indicates that 2-pole fixed-drive induction motors are still prevalent in the industry due to their low costs. Therefore, arguably a 25 Hz narrow band harvester could still meet the demand for this market segment in the short term. However, as the cost of energy increases and electronics decreases over time, more and more motors will eventually be fitted a variable speed drive to improve power efficiency. Hence, the need for wide bandwidth harvesters will be increasingly inevitable. The most favorable frequency bands are 22 - 52 Hz or 47 - 102 Hz.

Vibrations measured in wind turbines and their gearboxes cover a very different frequency spectrum. While the range of the main bearing frequency is 0.8 - 1.7 Hz, the majority of gearboxes measured a peak at a frequency below 8 Hz. Many of these low frequency vibrations are at relatively high displacement. Gearbox output shafts are typically measured at around 100 Hz or 900 - 1300 Hz. Speed at each measuring location is relatively constant. Due to the distinct vibration characteristics found in wind turbines, it is more cost effective to have a different set of narrow band harvesters specifically designed for the wind industry.

Last but not least, the most violent vibrations registered in the database are 3 g in acceleration, 511 mm/s in velocity and 22 mm in displacement. This gives a valuable reference to how robust a harvester is required. With a unity safety factor, the harvester should be able to withstand continuous base vibration of all these quantities without experiencing permanent damage.

3.5 Conclusions

In this chapter, an indicator called power transmission factor (κ_{pt}) is introduced to determine the optimal frequency and amplitude in a vibration spectrum recording. It showed that optimal frequency depends on the choice of input quantity that is held constant, and in the case of acceleration, the optimal frequency is equal to the natural frequency of the harvester notwithstanding the present of damping. From a total number of 15586 vibration recordings taken from industrial machinery, it is found that over 97 % of the optimal frequencies of the vibrations are below 500 Hz. The single most dominant frequency is about 25 Hz (half of mains line frequency), reflecting the fact that 2-pole fixed drive induction motors are still prevalent in the industry. As a result, the most favourable frequency band for narrow band

harvester is 24.3 - 25.3 Hz, and for wide band harvesters are 22 - 52 Hz and 47 - 102 Hz. The median *rms* vibration amplitude is 0.48 m/s^2. The statistics show that, when the mechanical and electrical damping are equal to 0.01 and the required power output is 500 μW, a harvester needs to have a minimum proof mass of 300 g and a tunable frequency range between 11 to 102 Hz to generate adequate power from 52 % of surveyed machines. The results indicate that large variations in vibration amplitudes and frequencies are present in machinery, and therefore it is unrealistic to design a one-size-fits-all harvester. In some equipment such as cooling fans and oil circulating pumps, the vibration levels are too low to be usable, unless the proof mass is excessively large. The Majority of vibrations in wind turbines reside in the lower end of the frequency spectrum and have relatively high displacement, hence a different set of harvesters should be designed specifically for the wind industry. For a unity safety factor, a harvester should be able to withstand continuous vibrations of 3 g in acceleration, 511 mm/s in velocity and 22 mm in displacement without experiencing permanent damage. The findings serve as a valuable reference for the design of a practical energy harvester.

4

Modelling of Single Mass Piezoelectric Energy Harvesters

4.1 Introduction

One of the most active areas of research in the energy harvesting community is the modelling of Lead Zirconate Titanate (PZT) cantilevers. Widely adapted dynamic models are the lumped-mass models [14] and the continuum models [31] (sometimes referred to as distributed parameter model [35]). The two types of models vary in complexity and each has its own merits. While the continuum models provide a precise estimation for PZT cantilever dynamics, the lumped-mass models result in a concise solution that is much more convenient for broader high-level analysis. It is often found that the lumped-mass models are commonly preferred at the beginning of the design process for bulk part estimation, and in cases where the energy harvester is treated as a subsystem of a much larger electrical system. On the other hand, continuum models are required when accurate predictions become necessary. Furthermore, continuum models provide information about the mode shapes of the beam and the stress distribution through modal analysis, as well as frequencies of higher vibration modes, which would not be otherwise obtained from lumped-mass models. Since the dynamic model of a single mass PZT cantilever is the building block for any PZT harvester designs, this chapter is dedicated to acquire a solid understanding of the theories, and to build an experimentally validated model. From literature review Section 2.2, it can be seen that the development of modelling in the community is incremental. The lumped-mass [15, 26] model was firstly adopted for general harvesters, but its lack of accuracy has forced researchers to pursue continuum models derived from variational methods. It started with a 2-layer piezoelectric cantilever without a tip mass [31], and then a tip mass was included in the continuum

model introduced by Erturk and Inman [35]. With purely resistive loads, the continuum models show exceptional accuracy from experimental validations. It is believed that the next incremental step is to have a generalised model that embodies all the modelling techniques for linear piezoelectric cantilevers. In this chapter, the commonly used lumped-mass and continuum models for PZT cantilevers are derived and merged to a generalised model. The analytical solution of the generalised model is then represented by a current source circuit, and the Thévenin equivalent circuit for further analysis. To purpose of the generalised model is that any analysis on the model will be backward compatible to both the lumped-mass model and the continuum model. The derived model is experimentally validated on PZT cantilever beams with a range of resistive loads.

This chapter is organised as follows. In Section 4.2 and 4.3, the lumped-mass model and the continuum model are derived and their analytical solutions are presented, respectively. In Section 4.4, the generalised model that incorporates both of the lumped-mass and the continuum model is introduced, and it explains how the model can be treated as a current source circuit and a Thévenin equivalent circuit to simplify further analysis, after which the source impedance of the electromechanical system is derived. In Section 4.5, a case study is presented to show how the source impedance and the electrical loads influence the electrical damping, resonant frequency and power output. Followed by Section 4.6, where experimental validation for a PZT cantilever beam without and with the tip mass is presented. Finally conclusions are given in Section 4.7.

4.2 Lumped-mass Approach

Lumped-mass models are widely used in the literature due to their simplicity, yet being able to capture most of the critical information about the PZT harvester at the beginning of a design process. PZT bimorph, a composite material that consists of two piezoelectric layers separated by a reinforced substrate layer, is commonly used for vibration energy harvesting. When subject to cyclic bending, the compression and tension of the two piezoelectric layers lead to charge separation, which results in an AC voltage. A PZT cantilever bimorph with an tip mass at the free end is illustrated in Figure 4.1. The relative vertical displacement of the mass is denoted by $w_L(t)$ and the base acceleration due to ambient vibrations is $\ddot{w}_b(t)$. In the energy harvesting community, it is a common practice to assume a harmonic base

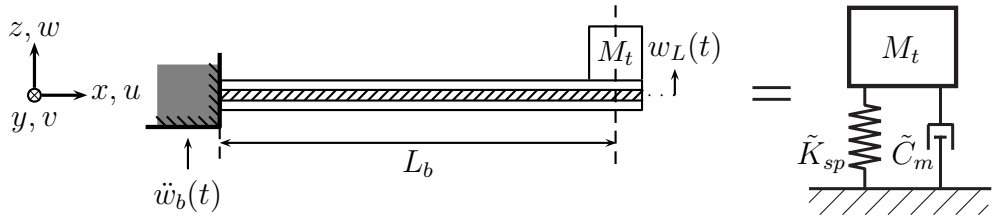

Figure 4.1: A cantilever bimorph with an tip mass. Dimensions are not to scale.

excitation. This is a valid approach since machine vibration is the sum of harmonics in different frequencies. For an input acceleration amplitude A_0 and frequency ω, the base excitation function can be written in the form of a complex function,

$$\ddot{w}_b(t) = A_0 e^{j\omega t}, \tag{4.1}$$

which is a more convenient form for frequency domain analysis. The cross section of the cantilever is depicted in Figure 4.2 assuming the two PZT layers to be of the same thickness. In between a substrate layer is inserted for reinforcement purpose. By applying parallel axis theorem, the second

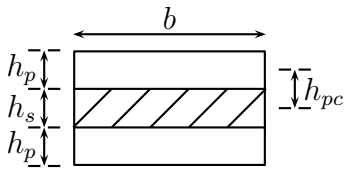

Figure 4.2: Cross section of the bimorph cantilever.

moment of areas for the PZT and the substrate layer are

$$I_p = 2\left(\frac{bh_p^3}{12} + bh_p h_{pc}^2\right) \text{ and } I_s = \frac{bh_s^3}{12}, \tag{4.2}$$

respectively. It is convenient to have I_s scaled so that the overall second moment of area can be written as a single expression

$$I = I_p + \frac{Y_s}{Y_p} I_s, \tag{4.3}$$

where Y_p and Y_s are the Young's moduli of the PZT material and the substrate layer, respectively. With the definition from (4.3), the rigidity of the whole cantilever is simply IY_p. Next, the bending moment of the cantilever needs to be determined. When subject to base vibration, the cantilever experiences various degrees of bending moments along the longitudinal direction (x-axis). It can be determined by having an arbitrary transverse cut on the

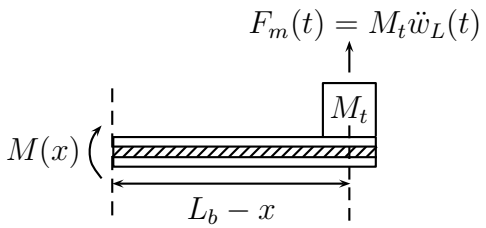

Figure 4.3: The balance of bending moment.

beam (see Figure 4.3) and summing up the overall moment. For the beam to be statically balanced in that instant, the bending moment of the beam at the cut has to counteract the one produced by the tip mass[1], which gives

$$M(x) = F_m(t)(L_b - x). \tag{4.4}$$

Unlike continuum models where the exact stress distribution along the cantilever is determined as eigenfunctions or mode shapes, lumped-mass models use the average stress as an approximation. Since the stress of the beam is

$$\sigma(x) = -\frac{M(x)h_{pc}}{I}, \tag{4.5}$$

integrating the stress over the entire beam and dividing it by the length, the average stress can be obtained as

$$\sigma_{ave}(t) = -\frac{1}{L_b}\int_0^{L_b} \frac{M(x)h_{pc}}{I}\,\mathrm{d}x, \tag{4.6a}$$

$$= F_m(t)/\kappa_a. \tag{4.6b}$$

The coefficient κ_a is defined to relate the vertical force exerted on the tip mass to the average stress of the beam:

$$\kappa_a = -\frac{2I}{h_{pc}L_b}. \tag{4.7}$$

The vertical deflection of the cantilever is obtained based on the Euler-Bernoulli beam theory, thus the following relationship holds:

$$\frac{\mathrm{d}^2w(x)}{\mathrm{d}x^2} = \frac{M(x)}{Y_pI}, \tag{4.8}$$

where $w(x)$ is the relative vertical displacement along the cantilever at x. Integrating the right hand side twice and applying the boundary conditions

[1]Here the mass of the cantilever beam is neglected in the lumped-mass model.

$w(0) = \dot{w}(0) = 0$, the beam deflection as a function of x can be obtained. Since $w_L(t)$ is indeed the deflection at $x = L_b$, substituting this to $w(x)$ yields

$$w_L(t) = w(L_b) = F_m(t)\frac{L_b^3}{3Y_pI}. \tag{4.9}$$

According to Hooke's law, the average strain can be obtained by the average stress given in (4.6b) as

$$\delta_{ave}(t) = \frac{\sigma_{ave}(t)}{Y_p} = -\frac{F_m(t)h_{pc}L_b}{2IY_p}. \tag{4.10}$$

Dividing equation (4.9) by (4.10) and rearranging to express the average strain in terms of the tip displacement, yields a linear equation

$$\delta_{ave}(t) = \kappa_b w_L(t), \tag{4.11}$$

where

$$\kappa_b = -\frac{3h_{pc}}{2L_b^2}. \tag{4.12}$$

Equation (4.11) describes the relationship between the average strain and the tip displacement, with κ_b being the linear constant.

What makes the PZT cantilever dynamics behave differently from an ordinary non-piezoelectric cantilever is the additional coupling force and the induced electric field in the PZT layers. The interaction between the electrical and mechanical variables are governed by the piezoelectric constitutive equations [70]:

$$\sigma_p = Y_pS_1 - d_{31}E_3Y_p, \tag{4.13a}$$

$$D_3 = d_{31}Y_pS_1 + \varepsilon_{33}^S E_3. \tag{4.13b}$$

The variable σ_p is stress, S_1 is longitudinal strain, d_{31} is the piezoelectric constant, E_3 is electric field, D_3 is the electric displacement and ε_{33}^S is the permittivity at constant strain. As a convention of piezoelectricity standard [70], the subscripts 1, 2 and 3 denote the direction x, y and z of Figure 4.1, respectively. The direction 3 is always denoted as the poled direction. The subscripts in d_{31} indicates that the electric field is parallel to direction 3, and the applied mechanical stress is parallel to direction 1. Among the material constants, the piezoelectric constant d_{ij} plays an important role. In energy harvesting context, d_{ij} is the ratio of short circuit charge density and applied mechanical stress, hence it has the unit of coulombs/square meter per newton/square meter. Generally a high piezoelectric constant is preferred

since the material can produce a higher voltage for the same stress. The piezoelectric constant d_{33} is normally two times higher than d_{31}, yet the shear mode d_{15} is the highest among all the modes [71]. However, the 31 mode has the advantage of being more compliant [5] and is the most common mode in commercial bimorphs at the time of writing. Hence, the type of 31 mode is chosen for this study. The analysis presented here is applicable to any other modes.

When the beam deflects, a stress described in (4.13a) is developed. This stress can be expressed in terms of force with the constant κ_a (as described in (4.6b)), yielding the sum of two forces acting on the tip mass. They are the restoring force with a spring constant k_{sp} and the backward coupling force caused by the induced electric field. Introducing mechanical damping, the first equation of motion is derived by summing all the forces acting on the mass:

$$M_t\ddot{w}_L(t) + \tilde{C}_m\dot{w}_L(t) + \tilde{K}_{sp}w_L(t) + \tilde{\Theta}_{bc}v_o(t) = -M_tA_0e^{j\omega t}. \tag{4.14}$$

The coefficients for each term are

$$\begin{aligned} \tilde{C}_m &= 2\xi_m\omega_nM_t, \\ \tilde{K}_{sp} &= \omega_n^2M_t, \\ \tilde{\Theta}_{bc} &= \frac{e_{31}\kappa_a}{h_{pe}}. \end{aligned} \tag{4.15}$$

The tilde symbol is used to distinguish the variables from similar variables appeared later on in other models. The equation of motion is coupled with the voltage output $v_o(t)$ through the backward coupling constant $\tilde{\Theta}_{bc}$. The PZT constant is written as $e_{31} = d_{31}Y_p$, and h_{pe} is the effective PZT layer thickness to accommodate the parallel and series connection. The corresponding definitions can be found in Table 4.1. The second equation of

Table 4.1: Series and Parallel Connections.

Description	Variable	Series	Parallel
Effective PZT layer thickness	h_{pe}	$2h_p$	h_p
Effective PZT area	A_{pe}	bL_b	$2bL_b$
Effective beam width	b_e	b	$2b$

motion is derived from the second piezoelectric constitutive equation (4.13b). Charge generated by the PZT can be evaluated by integrating the charge displacement over the effective area A_{pe}. In equation (4.13b), substituting S_1

for (4.11) and E_3 for $-\frac{v_o(t)}{h_{pe}}$, the charge developed on the piezoelectric layers can be determined as

$$Q = e_{31} w_L(t) \kappa_b A_{pe} - \varepsilon_{33}^S \frac{v_o(t)}{h_{pe}} A_{pe}. \tag{4.16}$$

Differentiating the charge with respect to time yields the load current $i_L(t)$. After rearranging, the second equation of motion can be written as

$$C_{pe} \dot{v}_o(t) - \tilde{\Theta}_{fc} \dot{w}_L(t) = -i_L(t), \tag{4.17}$$

where C_{pe} and $\tilde{\Theta}_{fc}$ are the effective internal capacitance and the forward coupling constant, respectively. They are given by:

$$C_{pe} = \frac{\varepsilon_{33}^S A_{pe}}{h_{pe}}, \tag{4.18a}$$

$$\tilde{\Theta}_{fc} = e_{31} \kappa_b A_{pe}. \tag{4.18b}$$

For a resistive load R_L, the load current is $i_L(t) = \frac{v_o(t)}{R_L}$. The coupled ordinary differential equation (4.14) and (4.17) constitute the lumped-mass model. The dynamics of the PZT beam is determined by solving for the unknowns $w_L(t)$ and $v_o(t)$. As mentioned earlier, the advantage of the lumped-mass model is that the analysis is scalable to a much larger electrical system where the PZT harvester just the sub-system. To take this advantage, the model can be written in the state space form,

$$\begin{bmatrix} \dot{w}_L(t) \\ \ddot{w}_L(t) \\ \dot{v}_o(t) \end{bmatrix} = \begin{bmatrix} 0 & 1 & 0 \\ -\frac{\tilde{K}_{sp}}{M_t} & -\frac{\tilde{C}_m}{M_t} & -\frac{\tilde{\Theta}_{bc}}{M_t} \\ 0 & \frac{\tilde{\Theta}_{fc}}{C_{pe}} & -\frac{1}{R_L C_{pe}} \end{bmatrix} \begin{bmatrix} w_L(t) \\ \dot{w}_L(t) \\ v_o(t) \end{bmatrix} + \begin{bmatrix} 0 \\ -1 \\ 0 \end{bmatrix} A_0 e^{j\omega t}. \tag{4.19}$$

On the other hand, the lumped-mass model can be directly solved using Laplace transform, which yields the solutions

$$w_L(t) = \frac{-A_0 M_t - \tilde{\Theta}_{bc} V_o}{-M_t \omega^2 + \tilde{C}_m \omega j + \tilde{K}_{sp}} e^{j\omega t}, \tag{4.20a}$$

$$v_o(t) = \frac{I_p}{C_{pe} \omega j + \frac{1}{Z_p} + \frac{1}{R_L}} e^{j\omega t}, \tag{4.20b}$$

where I_p and Z_p

$$I_p = -\frac{\tilde{\Theta}_{fc} A_0 \omega M_t j}{-M_t \omega^2 + \tilde{C}_m \omega j + \tilde{K}_{sp}}, \tag{4.21a}$$

$$Z_p = \frac{-M_t \omega^2 + \tilde{C}_m \omega j + \tilde{K}_{sp}}{\tilde{\Theta}_{fc} \tilde{\Theta}_{bc} \omega j}, \tag{4.21b}$$

are the equivalent current source and characteristic impedance of the electromechanical system, respectively. The time domain steady state solutions presented in (4.20a) and (4.20b) are expressed as complex functions, which give information for both amplitude and phase.

4.3 Continuum Approach

In a continuum model, the piezoelectric cantilever beam with or without the tip mass is represented by a dynamic system with infinite degrees of freedom. The model predicts the dynamics of any point along the beam at any time. As a result, the unknown relative displacement is a function of both space and time $w_{rel}(x,t)$. The derivation presented here is for a PZT cantilever beam with a tip mass, however, it can be applied to a cantilever beam without the tip mass by simply setting M_t to zero. Following the approach of the continuum modelling approach [72], the governing equations of the PZT system with base excitation shown in Figure 4.1 can be obtained as:

$$\begin{aligned} m\ddot{w}_{rel}(x,t) + c_s I \dot{w}''''_{rel}(x,t) + Y_p I w''''_{rel}(x,t) + \vartheta v_o(t) \\ \times \left[\frac{\mathrm{d}\delta(x)}{\mathrm{d}x} - \frac{\mathrm{d}\delta(x-L_b)}{\mathrm{d}x}\right] = -f_{ext}(t), \end{aligned} \tag{4.22}$$

where m is the mass per unit length of the beam, c_s is the equivalent strain rate damping constant, $v_o(t)$ is the output voltage and $f_{ext}(t)$ is the external forcing function. The notations "prime" and "dot" are used for partial derivatives with respect to x and t, respectively. The purpose of the term with Dirac Delta functions is to secure the survivability of the term when it is integrated with respect to x. The electromechanical coupling term $\vartheta v_o(t)$ is the direct result of applying the piezoelectric constitutive equation (4.13a). The electromechanical backward coupling term ϑ in (4.22) can be written as [72]

$$\vartheta = \frac{e_{31} b_e}{2h_p}\left[\frac{h_s^2}{4} - \left(h_p + \frac{h_s}{2}\right)^2\right], \tag{4.23}$$

where $e_{31} = d_{31} Y_p$, and h_p and h_s are thickness of the PZT and the substrate layer as can be referred to Figure 4.2. The parameter b_e is the effective width of the PZT beam depending on whether the PZT layers are connected in series or parallel. The corresponding definitions can be found in Table 4.1. When subject to base excitation, the beam experiences forces due to the continuously distributed mass of the beam as well as the rather concentrated

tip mass M_t. This is included by the external forcing term $f_{ext}(t)$ in (4.22) as

$$f_{ext}(t) = A_0\Big[m + M_t\delta(x - L_b)\Big]e^{j\omega t}. \tag{4.24}$$

Although the function $f_{ext}(t)$ is called external forcing function, its unit is in fact in *force* per unit *length*.

Applying the method of separation of variables [32], the solution for the partial differential equation (4.22) can be written in the form of a summation of all vibration modes,

$$w_{rel}(x,t) = \sum_{r=1}^{\infty} \phi_r(x)\eta_r(t), \tag{4.25}$$

where $\phi_r(x)$ here is the mass normalised eigenfunction determined from the cantilever boundary conditions, and $\eta_r(t)$ is the time dependent amplitude of the rth mode of vibration. With the procedures detailed in Appendix Section A.1, the mass normalised eigenfunction $\phi_r(x)$ is determined as [35]

$$\phi_r(x) = C_r\theta_r(x), \tag{4.26}$$

where $\theta_r(x)$ is

$$\theta_r(x) = \cos\frac{\lambda_r}{L_b}x - \cosh\frac{\lambda_r}{L_b}x + \zeta_r\left(\sin\frac{\lambda_r}{L_b}x - \sinh\frac{\lambda_r}{L_b}x\right), \tag{4.27}$$

and ζ_r is

$$\zeta_r = \frac{\sin\lambda_r - \sinh\lambda_r + \lambda_r\frac{M_t}{mL_b}(\cos\lambda_r - \cosh\lambda_r)}{\cos\lambda_r + \cosh\lambda_r - \lambda_r\frac{M_t}{mL_b}(\sin\lambda_r - \sinh\lambda_r)}. \tag{4.28}$$

The modal amplitude constant C_r in (4.26) can be evaluated as

$$C_r = \frac{1}{\sqrt{m\int\limits_0^{L_b}\theta_r^2(x)\,\mathrm{d}x + M_t\theta_r^2(L_b) + I_t\left[\left(\frac{\mathrm{d}\theta_r(x)}{\mathrm{d}x}\right)^2\right]_{x=L_b}}}, \tag{4.29}$$

where I_t is the moment of inertia of the tip mass about the y-axis. The eigenvalues of the system λ_r are obtained by solving the characteristic equation

$$\begin{aligned} &1 + \cos\lambda\cosh\lambda + \lambda\frac{M_t}{mL_b}(\cos\lambda\sinh\lambda - \sin\lambda\cosh\lambda) \\ &- \frac{\lambda^3 I_t}{mL_b^3}(\cosh\lambda\sin\lambda + \sinh\lambda\cos\lambda) \\ &+ \frac{\lambda^4 M_t I_t}{m^2 L_b^4}(1 - \cos\lambda\cosh\lambda) = 0, \end{aligned} \tag{4.30}$$

and the natural angular frequency for the rth mode is determined from λ_r through the relationship

$$\omega_r = \lambda_r^2 \sqrt{\frac{Y_p I}{m L_b^4}}. \tag{4.31}$$

To obtain the ODE of $\eta_r(t)$, Galerkin method [32] is applied. Substituting (4.25) to (4.22), multiplying $\phi_r(x)$ and integrating with respect to x on both sides of the equation, yields a 2nd order ODE of $\eta_r(t)$

$$\ddot{\eta}_r(t) + 2\xi_r\omega_r\dot{\eta}_r(t) + \omega_r^2\eta_r(t) + \chi_r v_o(t) = -f_r(t), \tag{4.32}$$

using the orthogonal properties of the eigenfunctions, where ξ_r is the mechanical damping ratio of the rth mode and the modal electromechanical coupling term is

$$\chi_r = \vartheta\phi_r'(L_b). \tag{4.33}$$

Note that in the RHS of equation (4.32), compared to the same equation in [35], the negative sign has been taken out from $f_r(t)$. The external forcing function becomes

$$\begin{aligned} f_r(t) &= \int_0^{L_b} f_{ext}(t)\phi_r(x)\,\mathrm{d}x, \\ &= F_r e^{j\omega t}, \end{aligned} \tag{4.34}$$

where

$$F_r = A_0\left[m\int_0^{L_b}\phi_r(x)\,\mathrm{d}x + M_t\phi_r(L_b)\right]. \tag{4.35}$$

Equation (4.32) describes the electromechanical coupling of the system from the mechanical perspective. The second equation of motion that describes the electrical behaviours and its influence towards the mechanical system is derived from the second piezoelectric constitutive relation (4.13b). For a pure resistive load R_L, the second coupled equation of motion can be written in the form

$$C_{pe}\dot{v}_o(t) - \sum_{r=1}^{\infty}\varphi_r\dot{\eta}_r(t) = -\frac{v_o(t)}{R_L}. \tag{4.36}$$

C_{pe} is the effective capacitance and has the same definition as (4.18a). The forward coupling constant φ_r that dictates the current generated by the PZT can be written as

$$\varphi_r = -\frac{e_{31}\,(h_p + h_s)\,b_e}{2}\phi_r'(L_b). \tag{4.37}$$

It should be noted that due to the generalisation of series and parallel formulation here, the effective width b_e is used to define φ_r. Thus it appears

different from the parallel case in [73]. The b_e in (4.37) is necessary to provide the correct factor for the equation of motion (4.36) for both series and parallel cases. This generalising approach leads to the equality of the backward and forward coupling constants χ_r and φ_r. The coupled ordinary differential equations (4.32) and (4.36) form the dynamic model of the PZT cantilever with a single tip mass. They can be solved analytically using Laplace transform. Assuming the solution for the output voltage to be of the form $v_o(t) = V_o e^{j\omega t}$, solving (4.32) for $\eta_r(t)$ gives

$$\eta_r(t) = \frac{-F_r - \chi_r V_o}{\omega_r^2 - \omega^2 + j2\xi_r\omega_r\omega} e^{j\omega t}. \tag{4.38}$$

Therefore, the analytical solution for the *relative* displacement $w_{rel}(x,t)$ under harmonic base excitation is obtained by substituting (4.38) into (4.25), yielding:

$$w_{rel}(x,t) = -\sum_{r=1}^{\infty} \frac{-F_r - \chi_r V_o}{\omega_r^2 - \omega^2 + j2\xi_r\omega_r\omega} \phi_r(x) e^{j\omega t}. \tag{4.39}$$

The solution for the output voltage can be determined by substituting (4.38) to (4.36) and rearranging for $v_o(t)$, which gives

$$v_o(t) = \frac{I_p}{C_{pe} j\omega + \frac{1}{Z_p} + \frac{1}{R_L}} e^{j\omega t}, \tag{4.40}$$

where the source current and the characteristic impedance of the PZT cantilever system are

$$I_p = -\sum_{r=1}^{\infty} \frac{j\omega F_r \varphi_r}{\omega_r^2 - \omega^2 + j2\xi_r\omega_r\omega}, \tag{4.41a}$$

$$Z_p = \frac{1}{\sum_{r=1}^{\infty} \frac{j\omega\chi_r\varphi_r}{\omega_r^2 - \omega^2 + j2\xi_r\omega_r\omega}}, \tag{4.41b}$$

respectively. As can be seen, the solution shares similarity to the one derived in the lumped-mass model. Indeed, if only the first vibration mode is considered, the solution of the continuum model has the same *mathematical form* as that of the lumped-mass model. In light of this, it is possible to develop a dynamic model that generalises the two models.

4.4 Derivation of a Generalised Model

Comparing the coupled equations of motion derived from the lumped-mass and the continuum models, (4.14), (4.17), (4.32) and (4.36), it can be found

that they share the same mathematical structure. If a generalised formulation of the two models exists, a common solution can be reached, and any further analysis will be consistent to both models. As can be seen in Figure 4.4, the purpose of the generalised model is to form a single formulation that enables all the subsequent analysis to be backward compatible to both the lumped-mass model and the continuum model, which are the two types of models that dominate the piezoelectric energy harvesting arena. The method to obtain

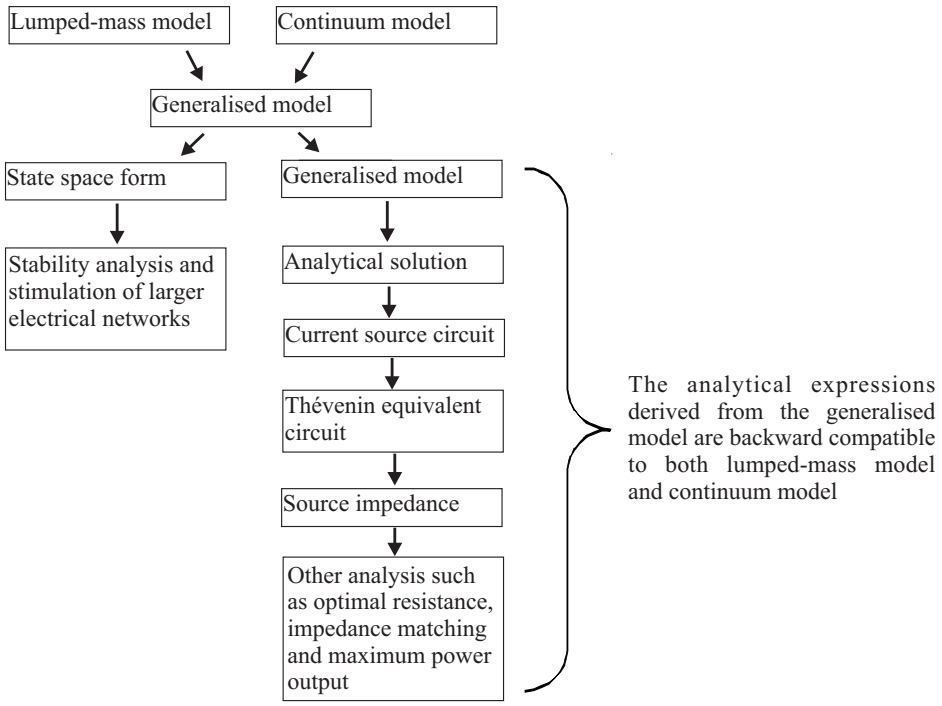

Figure 4.4: The purpose of the generalised model.

the generalised model is to compare the equations of motion of the lumped-mass model with that of the continuum model, and introduce a common equation of motion with terms that can be defined by either model. To resemble the form of the lumped-mass model, only the fundamental mode of the continuum model is included. This however, does not compromise accuracy when the cantilever is excited near resonant frequency, which is the frequency region of primary interest for energy harvesting applications. Using the superscript "$\wedge$" to denote single vibration mode, the displacement at $x = L_b$ can be written in different forms: $w_L(t) = \hat{w}_{rel}(L_b, t) = \phi_r(L_b)\eta_r(t)$. Hence (4.32) can be expressed as

$$\phi_r(L_b)\ddot{\eta}_r(t)+2\xi_r\omega_r\phi_r(L_b)\dot{\eta}_r(t)+\omega_r^2\phi_r(L_b)\eta_r(t)+\phi_r(L_b)\chi_r v_o(t) = -\phi_r(L_b)f_r(t). \tag{4.42}$$

In addition, both (4.32) and (4.36) can be rewritten in terms of the tip displacement

$$\ddot{w}_L(t) + 2\xi_r\omega_r\dot{w}_L(t) + \omega_r^2 w_L(t) + \frac{\bar{\Theta}_{bc}}{\bar{M}_{eq}} v_o(t) = -\phi_r(L_b) f_r(t), \tag{4.43a}$$

$$C_{pe}\dot{v}_o(t) - \bar{\Theta}_{fc}\dot{w}_L(t) = -i_L(t). \tag{4.43b}$$

The bar symbol is used for variables associated with the continuum model. Essentially the continuum model is derived from variational methods such as Hamilton's principle [31]. As discussed earlier in Section 4.3, since the backward and forward coupling constants χ_r and φ_r defined in (4.33) and (4.37) are equal, it leads to

$$\bar{\Theta}_{bc} = \bar{\Theta}_{fc} = \frac{\chi_r}{\phi_r(L_b)} = \frac{\varphi_r}{\phi_r(L_b)}. \tag{4.44}$$

It should be noted that despite the equality of the forward and backward coupling constants in the continuum model, it is not the case in the lumped-mass model. This is because in the lumped-mass model, approximation methods are used to evaluate the average strain and stress of the cantilever, as opposed to energy methods employed by the continuum method, through which the exact stress and strain distribution are determined. Since essentially (4.42) and (4.43a) are the same equation, by equating the forth term and using the relationship of (4.44), the equivalent mass can be determined as:

$$\bar{M}_{eq} = \frac{1}{\phi_r^2(L_b)}. \tag{4.45}$$

By using abstract terms for the coupled equations of motion to maintain the same mathematical structure, the generalised model can be written as

$$M_{eq}\ddot{w}_L(t) + C_{eq}\dot{w}_L(t) + K_{eq}w_L(t) + \Theta_{bc}v_o(t) = -\mu_c\ddot{w}_b(t)M_{eq}, \tag{4.46a}$$

$$C_{pe}\dot{v}_o(t) - \Theta_{fc}\dot{w}_L(t) = -\frac{v_o(t)}{R_L}, \tag{4.46b}$$

where μ_c is the correction factor. By substituting the abstract terms by the corresponding definitions in Table 4.2, it can become either the lumped-mass model or the continuum model. Furthermore, the effective variables in table 4.1 still apply to the generalised model to include both series and parallel connections of PZT bimorph cantilevers.

The generalised model is a system of ordinary differential equations. Depending on the subsequent analysis, it can be rewritten to the state space

Table 4.2: Term definitions for the generalised model.

Parameter	Lumped-mass model	Continuum model
ω_n	$\sqrt{\frac{2Y_pI}{L_b^3M_t}}$	Roots of characteristic equation (4.30)
M_{eq}	M_t	$\frac{1}{\phi_r^2(L_b)}$
C_{eq}	$2\xi_m\omega_nM_{eq}$	$2\xi_r\omega_rM_{eq}$
K_{eq}	$\omega_n^2M_{eq}$	$\omega_r^2M_{eq}$
Θ_{bc}	$\frac{d_{31}Y_p\kappa_a}{t_{pe}}$	$\frac{\varphi_r}{\phi_r(L_b)}$ or $\frac{\chi_r}{\phi_r(L_b)}$
Θ_{fc}	$d_{31}Y_p\kappa_bA_{pe}$	
μ_c	1	$\phi_r(L_b)\left[m\int_0^{L_b}\phi_r(x)\,\mathrm{d}x + M_t\phi_r(L_b)\right]$

form, or it can be solved directly in the frequency domain. Applying the latter method and assuming a harmonic input displacement $\ddot{w}_b(t) = A_0e^{j\omega t}$, the analytical solution for (4.46) is

$$w_L(t) = \frac{-\mu_cA_0M_{eq} - \Theta_{bc}V_o(\omega)}{-M_{eq}\omega^2 + C_{eq}\omega j + K_{eq}}e^{j\omega t}, \tag{4.47a}$$

$$v_o(t) = \frac{I_p}{C_{pe}\omega j + \frac{1}{Z_p} + \frac{1}{R_L}}e^{j\omega t}. \tag{4.47b}$$

The source current and the characteristic impedance of the PZT beam are

$$I_p = -\frac{\Theta_{fc}\mu_cA_0\omega M_{eq}j}{-M_{eq}\omega^2 + C_{eq}\omega j + K_{eq}}, \tag{4.48a}$$

$$Z_p = \frac{-M_{eq}\omega^2 + C_{eq}\omega j + K_{eq}}{\Theta_{fc}\Theta_{bc}\omega j}, \tag{4.48b}$$

respectively. Of particular interest is the voltage output in (4.47b), which coincides with the output voltage of a current source circuit shown in Figure 4.5. The three current streams flowing from the piezoelectric crystal are clearly labelled according to (4.46b). In the circuit, the capacitor C_{pe} is the well understood PZT internal capacitance formed between the PZT electrodes. Great emphasis is given to the characteristic impedance Z_p because

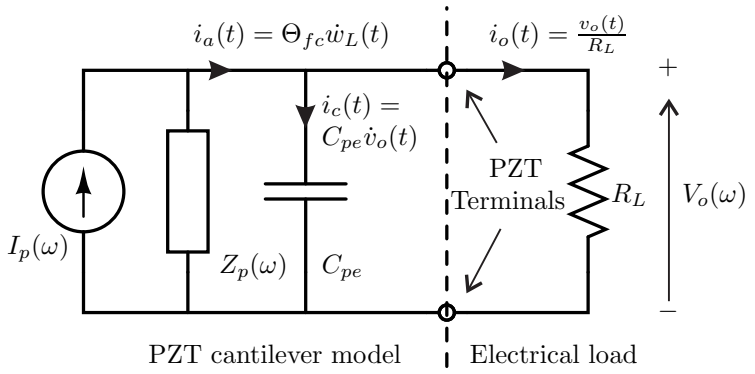

Figure 4.5: Current source circuit representation of the PZT continuum model connecting a resistive load.

it exhibits a significant but often neglected electrical attribute of the PZT cantilever system. Equation (4.48b) clearly shows how the source impedance is related to the excitation frequency, as well as to the cantilever's geometry and material properties through the backward and forward coupling constants. Hence it is possible to design the impedance to a desirable range by manipulating the parameters. Combining with the internal capacitance, the total source impedance of the system is illustrated in the Thévenin equivalent circuit shown in Figure 4.6. The source voltage of the circuit is

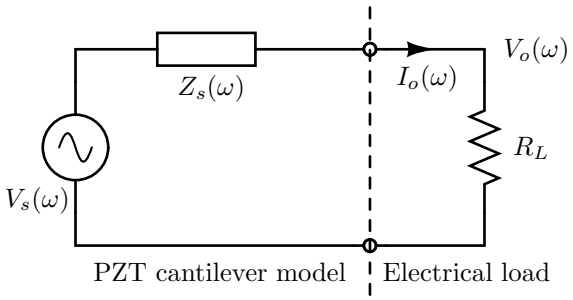

Figure 4.6: Thévenin equivalent circuit of the electromechanical system.

$V_s = I_p Z_s$. The source impedance Z_s is essentially the total impedance of C_{pe} and Z_p connecting in parallel. After some mathematical simplifications, the analytical expression of the source impedance is reduced to:

$$Z_s(\omega) = \frac{\left(M_{eq}\omega^2 - C_{eq}\omega j - K_{eq}\right) j}{\omega\left(-C_{pe}M_{eq}\omega^2 + C_{pe}C_{eq}\omega j + C_{pe}K_{eq} + \Theta_{bc}\Theta_{fc}\right)}. \tag{4.49}$$

As a significant result from the analysis of the generalised model, the equation (4.49) explicitly indicates how the resultant electrical impedance is dependent

on many of the mechanical parameters of the PZT system. Moreover, it gives important information such as resonant frequency, optimal load resistances and maximum power output. The resonant frequency is the root at which the imaginary part of Z_s becomes zero. Substituting that frequency into the real part of Z_s gives the optimal load resistance, combined with the voltage output given in (4.47b), the maximum power output can be determined.

4.5 Case Study

In this section, a case study is carried out showing the relationship between the source impedance and the power output, with respect to the driving frequency and load resistance. Applying the generalised model in the lumped-mass mode, the case study simulates a series connected cantilever bimorph with geometry and material properties listed in Table 4.3. First, a range

Table 4.3: Case study parameters & material properties.

Description	Symbol	Value
Mass dimension	$w \times h \times l$	$8 \times 8 \times 8$ mm^3
Mass density	ρ_m	7800 kg/m^3
Beam width	b	6 mm
Beam length	L	20 mm
Thickness of single PZT layer	h_p	0.13 mm
Thickness of substrate	h_s	0.12 mm
PZT density	ρ_p	7800 kg/m^3
Substrate density	ρ_s	7200 kg/m^3
Substrate elastic modulus	Y_s	120 GPa
PZT elastic modulus	Y_p	62 GPa
Relative permittivity	ε_r	3800 F/m
PZT constant	d_{31}	-320×10^{-12} m/V
Mechanical damping ratio	ξ_m	0.02

of load resistance is substituted to identify the optimal value and maximum power when the cantilever is excited at resonant frequencies. It should be noted that resonant frequency is different from natural frequency because the former gives the maximum response in the presence of damping and backward coupling force. Since both the damping and backward coupling force change with different load resistance, so does the resonant frequency. The power output at resonance corresponding to the resistance values is shown in Figure

4.7. For this PZT system two optimal load resistances are found: 35 kΩ and

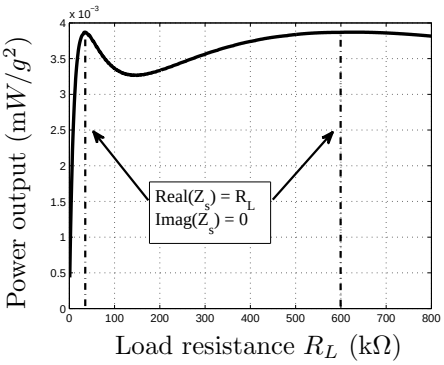

Figure 4.7: Power output at resonance for various load resistance.

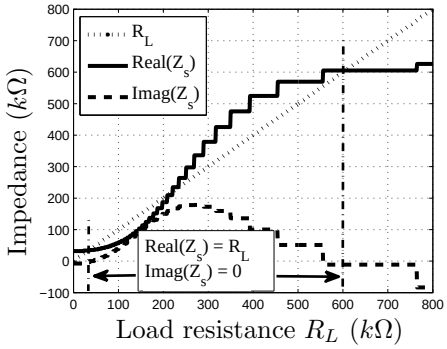

Figure 4.8: Source impedance at resonance for various load resistance.

600 kΩ. Figure 4.8 illustrates how the source impedance varies as the load resistance and resonant frequency changed. It can be verified in Figure 4.8 that both optimal resistances give zero reactance for Z_s as well as having their values equal to the real part of Z_s. In other words, both of the two optimal resistive loads lead to a conjugate matched system. The zero source reactance implies that the reactance of C_{pe} and Z_p gets cancelled, forming an electrically resonating system. An important remark to be pointed out is that a mechanically resonant PZT cantilever does not necessarily deliver its maximum potential power to the load. Both mechanical and electrical resonance (impedance matched) are required to obtain the maximum power transfer from the source vibration to the electrical load. Discussions in this work, the terms conjugate matching and impedance matching deemed the same, and they are used interchangeably herein.

The equivalent electrical damping ratio is closely related to the cause of the dual maximum power outputs. By equating the backward coupling term in (4.47a) to the conventional electrical damping, i.e. $\Theta_{bc}v_0(t) = 2\xi_e\omega_n M_{eq}\dot{w}_L(t)$, the equivalent electrical damping can be determined. The output voltage and tip velocity are not necessarily in phase. Hence the result is a complex number, of which only the real part contributes to the electrical damping. Thus it yields the expression:

$$\xi_e = \text{Real}\left(\frac{\Theta_{bc}v_0(t)}{2\omega_n M_{eq}\dot{w}_L(t)}\right). \tag{4.50}$$

Comparing the mechanical damping with the electrical damping in Figure 4.9, it becomes obvious why the maximum power appears at the two resistance values. Since both of the two optimal resistances can impose an

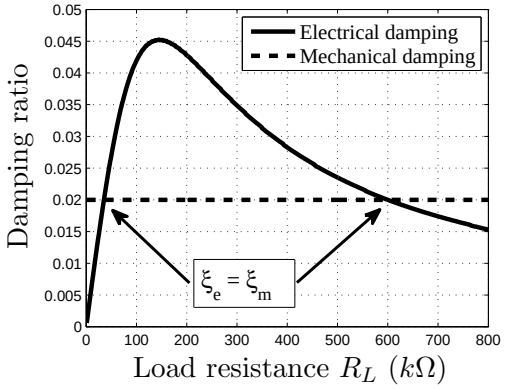

Figure 4.9: Mechanical and electrical damping ratio at resonance.

electrical damping that is equal to the mechanical damping, the maximum power condition is fulfilled. A useful indication from Figure 4.9 is the impact on the optimal resistances by the mechanical damping ratio. As the mechanical damping becomes lower, the two optimal resistances become more extreme. For a very low mechanical damping, the second optimal resistance can be too large to be achieved. Therefore considerations have to be taken to realize a practical impedance matching system.

Next, the simulation is examined from a slightly different view. Three load matching strategies and their power outputs are compared: a fixed optimal resistive load, a variable resistive load for modulus matching, and a variable complex load for conjugate matching. As can be seen in Figure 4.10, the response of the PZT system with the optimal load of 600 kΩ has a narrow bandwidth and is resonating at the open circuit frequency Ω_{oc}, where maximum power is obtained. A modulus matched system is achieved by varying

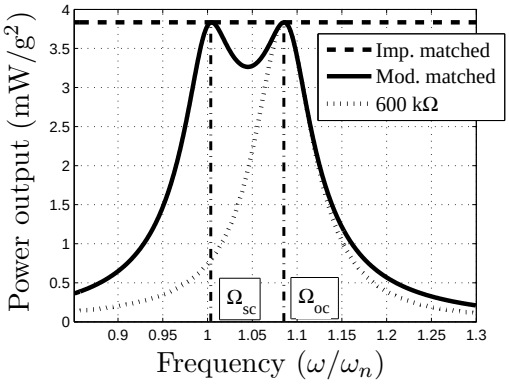

Figure 4.10: Power output for different load matching strategies.

the resistance of the load R_L and making it equal to the modulus (or amplitude) of the source impedance Z_s. As being observed in Figure 4.10, modulus matching results in a significant improvement in frequency range compared to the fixed optimal resistance system. The comparison shows that the modulus matched system is able to enhance the effective excitation frequency to a range between the short and open circuit resonant frequencies Ω_{sc} and Ω_{oc}. The required load resistances to achieve the modulus matching are shown in Figure 4.11. Although devising a variable load for self-adjusting mod-

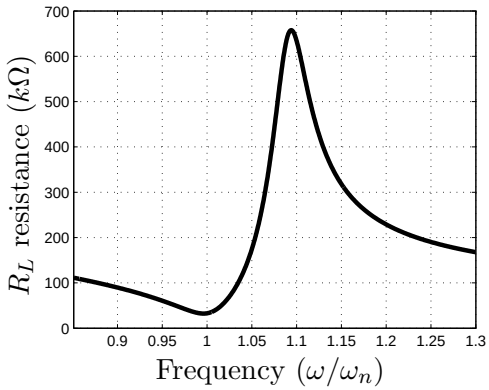

Figure 4.11: Resistive value of R_L for modulus matching.

ulus matching is not a trivial exercise, a circuit to achieve it is proposed by Kong et al. [57]. The only concern is the overhead incurred to operate the circuit, which has to be weighed against the power (or frequency range) gained. Maximising the effective frequency range can help justify such overhead. According to Chapter 3 of [73], the range between Ω_{sc} and Ω_{oc} is solely dependent on the electromechanical coupling coefficient k_{31}, which is defined as:

$$k_{31}^2 = \frac{d_{31}^2 Y_p}{\varepsilon_{33}^T}. \tag{4.51}$$

The permittivity at constant stress ε_{33}^T relates to the one at constant strain as $\varepsilon_{33}^T = \varepsilon_{33}^S + d_{31}^2 Y_p$ [70]. Approximately the normalized short and open circuit frequency can be defined by

$$\Omega_{sc} = 1, \quad \Omega_{oc} = \sqrt{1 + k_{31}^2}. \tag{4.52}$$

The fact that k_{31}^2 is the property associated with the PZT material shows the limitation on the frequency range a modulus matched system can achieve. For example the PZT-5H[2] material has an electromechanical coupling coefficient

[2]Type 5H4E (Industry Type 5H, Navy Type VI), available from Piezo System, Inc.

$k_{31} = 0.44$, which limits the frequency range for modulus matching to about 10% of the natural frequency.

If the load resistor R_L in Figure 4.6 is replaced by a complex load whose value is conjugate to the source impedance Z_s, then a conjugate matched system is obtained. As shown in Figure 4.10, the model deduces that a conjugate matched system always yield maximum power output regardless of the excitation frequency. The same result is obtained by Luo and Hofmann [59]. Mathematically this is because the excitation frequency term has been eliminated along with the complex component of the power output. An impedance matched circuit dramatically increases the energy circulation of the entire electromechanical system. When input frequency is far away from the natural frequency, resonance is maintained by feeding the electrical energy back to the mechanical system. Note that the model assumes ideal electrical components, therefore losses are not included in the power output curve. The impedance of the complex load required to achieve conjugate matching is shown in Figure 4.12. A positive imaginary load indicates that

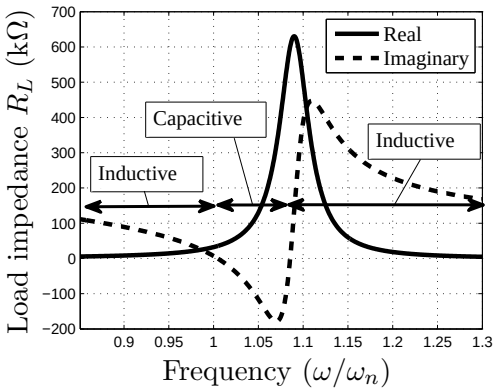

Figure 4.12: Real and imaginary part of R_L required for conjugate matching.

the load is inductive. Since $Z_L = L\omega j$, unless the frequency is very high, the inductance value required for the matching is prohibitively large. Having said that, the gain in the frequency range given by an impedance matched system seems enormous. In an RLC circuit, the required inductance for electrical resonance is $L = \frac{1}{C\omega^2}$, thus connecting the two piezoelectric layers in parallel and/or adding more capacitance in parallel can significantly reduce the required inductance. Due to the non-ideal characteristics of electrical components, there will be losses in real circuit. Therefore, in reality the final power obtained against input frequency is unlikely to be a constant. Instead, it will be inevitably curved down on both sides of the natural frequency as a result of the losses. This phenomenon will be discussed in detail in Chapter

6 with the help of an improved continuum model. Referring back to Figure 4.12, interestingly, there is a frequency region where a capacitive load is required. Since $Z_C = -\frac{j}{C\omega}$, impedance matching in this region is easily achievable due to the availability of a wide range of capacitance.

4.6 Experimental Validation

Upon the development of the generalised model, computer programs are created in Matlab to solve the system of differential equations. For the continuum model, the characteristic equation is solved numerically. It is very important to validate the model against experiments before its usage for energy harvester design purposes. Experimental validation not only verifies the credibility of the model, but also helps explain unknown phenomena and new insights. The lower accuracy associated with lumped-mass models compared to the continuum models is well understood [30], therefore, in this section only the experimental validation of the continuum model is presented. The instruments involved in the experiment are shown in Figure 4.13. The schematics showing how the instruments are connected is illus-

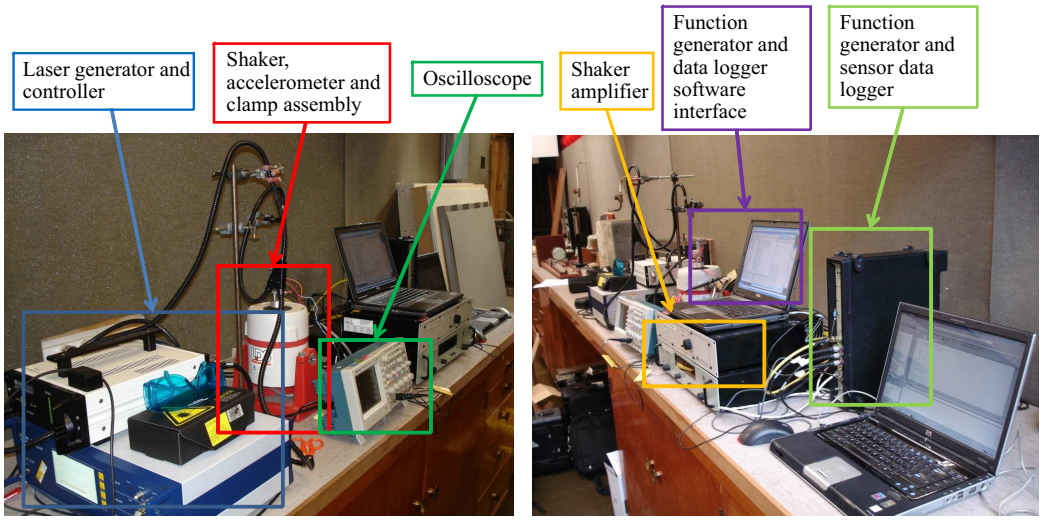

Figure 4.13: Instruments and experimental set-up.

trated in Figure 4.14. The piezoelectric beam is shaken vertically by an electromagnetic shaker. The three measurements from the response of the piezoelectric beam are base acceleration, tip velocity and output voltage. An industrial accelerometer from Wilcoxon Research is fastened under the beam to measure base acceleration. The laser vibrometer measures the velocity of

the beam deflection. The output voltage is directly measured from the two piezoelectric layers. All sensing signals and the driving signal are connected to the instrument called Pulse, which is controlled by the provided interface software programme running in a laptop. Pulse gives both time waveform and Fast Fourier Transform (FFT) measurements, which can be saved in csv format for post processing. It should be noted that the FFT resolution given by Pulse is limited to 1 Hz, which corresponds to sampling time of 1 second. The effects of aliasing is eliminated by the anti-aliasing filters built-in to the

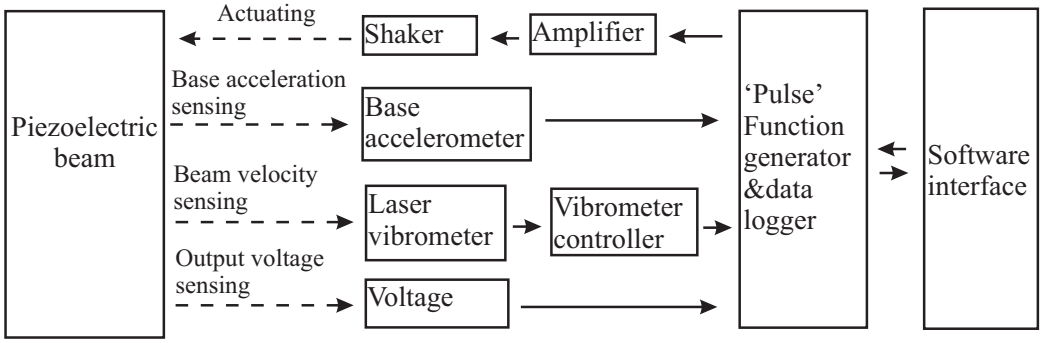

Figure 4.14: Schematics of experimental set-up.

sampling modules. Lastly, to align with the practice of the energy harvesting community, all results are represented in terms of Frequency Response Function (FRF), which is determined by scaling the response by the base acceleration.

4.6.1 Piezoelectric beam with no tip mass

Figure 4.15(a) shows the assembly of the clamp with a piezoelectric beam, and the accelerometer underneath the clamp for base acceleration measurement. Figure 4.15(b) shows the vibrometer measuring the velocity of the tip of the piezoelectric beam. Setting the tip mass to zero in the model, the dynamic response of the piezoelectric beam can be determined and compared with the experimental measurement. The beam dimensions and material properties used in this experiment can be found in Table B.1 of Appendix B. For each excitation frequency, the beam is shaken for 5 second to reach steady state, then an FFT recording takes place. This process is repeated for a range of pre-set excitation frequencies and resistive loads. The FRF results for the measured velocity and voltage output are shown in Figure 4.16. The overlaid solid curves are the results predicted by the continuum model. As can be seen, both velocity and voltage output predicted by the model are closely matched with the experimental measurement for the whole range of chosen resistive loads. Due to the constraint on FFT resolution (sampling time),

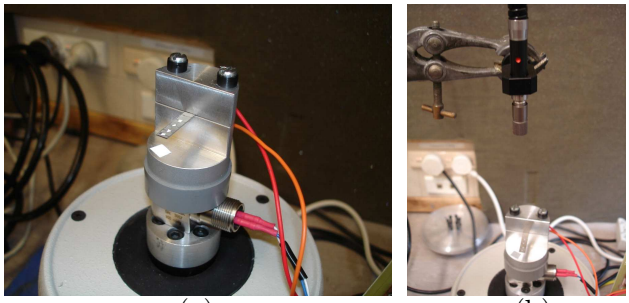

(a) (b)

Figure 4.15: Experimental set-up of a piezoelectric beam with no tip mass. (a) shows the clamp assembly and the accelerometer. (b) shows the vibrometer for velocity measurement.

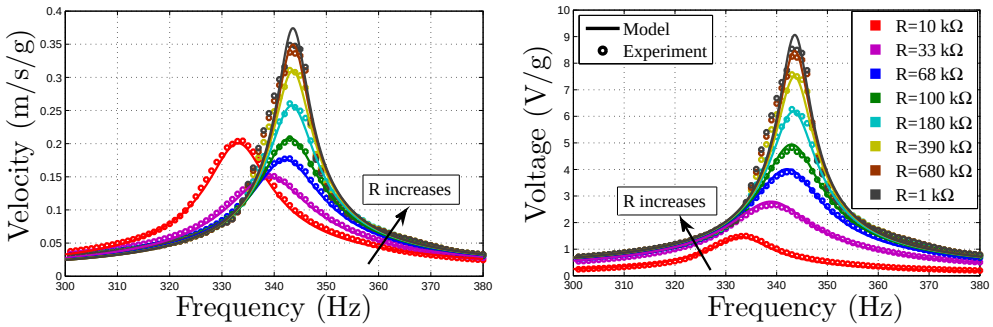

Figure 4.16: Comparison of Frequency Response Functions for velocity and voltage of a PZT cantilever beam without tip mass.

not all the peaks were measured, which could be the reason for the slight mismatch found around some resonant peaks. Nonetheless, it shows that the model can accurately predict the shift of resonant frequencies as the load resistance is changed. Overall speaking, the modelling results are very satisfactory.

4.6.2 Piezoelectric beam with a tip mass

In this experimental validation process, a piezoelectric beam with a mass at the free end is fitted to the clamp assembly, which can be seen in Figure 4.17. The material properties and dimension of the PZT beam used in this experiment can be found in Table B.2 of Appendix B. Measurement procedures described in the previous section is repeated to obtain the FRF of velocity and voltage output for a range of resistive loads. The results are presented in Figure 4.18. Quantitatively, the modelling results are in good agreement with the measurement. In the velocity validation with the 10 and 33 kΩ load resistances, small discrepancy is observed between experiment and the model. However, for the same load resistances the voltage outputs and the modelling results are closely correlated. The overall validating results should be sufficient to conclude that the continuum model can

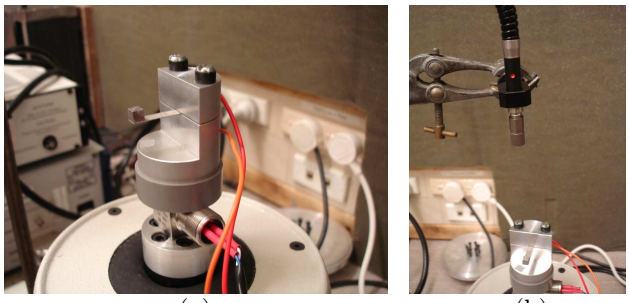

(a) (b)

Figure 4.17: Experimental set-up of a piezoelectric beam with a tip mass.

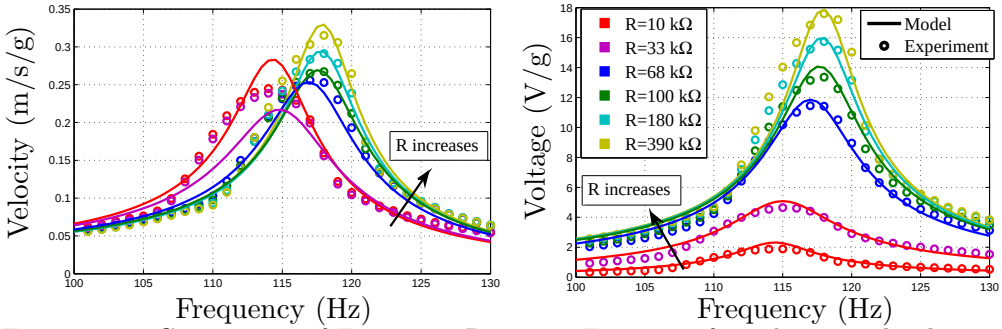

Figure 4.18: Comparison of Frequency Response Functions for velocity and voltage of a PZT cantilever beam with a tip mass.

produce credible predictions for a piezoelectric cantilever beam with a tip mass.

4.7 Conclusions

In this chapter, a generalised model for piezoelectric cantilever beams is derived. By substituting the appropriate definitions of the constant terms, the model can be used as either the lumped-mass model or the continuum model. Series and parallel connections of the two piezoelectric layers are also incorporated into the model. This model is considered to be an incremental refinement from the existing models for piezoelectric cantilevers. The main purpose of the generalised model is to enable any further analysis on the model to be backward compatible to both lumped-mass and continuum model, which are the two dominating types of models in the piezoelectric energy harvesting arena. In addition, the equivalent current circuit and the Thévenin equivalent circuit of the model are presented. The analysis leads to the analytical expression of the source impedance. As explained in Section 4.4, the expression explicitly shows how the source impedance is related to the mechanical and electrical parameters of the system, and it provides the information of resonant frequency, optimal load resistances and power output. All of which are of particular interest to the designer. In light of the electrical attribute

of the electromechanical system, a case study is carried out to investigate the effects of electrical loads on the frequency range and power output of the harvester. In other studies, it is well known that, without using a complex load, there can be two optimal load resistances that give maximum power output for a piezoelectric harvester. The case study explains why this happens. It reveals that each of the two optimal load resistances matches the system's impedance entirely, and results in an electrical damping that is equal to the mechanical damping. Therefore the conditions for maximum power are fulfilled. The case study also shows that modulus matching can tune the resonant frequency of the harvester. The tuning range is solely dependent on the coupling coefficient of the PZT material. For the commonly available PZT-5H crystal, the tuning range is about 10 % of the natural frequency. The case study also suggests that an impedance matched system can potentially achieve a wide tuning range of resonant frequency. To achieve impedance matching, a capacitive load is required between the short circuit and open circuit frequencies, whereas, for frequencies outside this region, an inductive load is required. Finally, experimental validations are performed on PZT cantilever beams with and without a tip mass. Quantitatively, the frequency response of the beam velocity and power output predicted by the model for a whole range of load resistances are in excellent agreement with observations. It is confidant that the model can serve as a reliable tool for the purposes of energy harvester design.

5

Modelling of Double-mass Piezoelectric Energy Harvesters

5.1 Introduction

One way to solve the narrow bandwidth issue of vibration-based energy harvesters is through multi-modal structures. The multi-modal approach does not necessarily require extra mechanical components and control effort, making it a simple and reliable solution. Adding multiple masses on a PZT beam is one way to implement the multi-modal approach. Moreover, a multi-mass beam array can be employed instead of the conventional single mass beam array to better utilize the proof masses and space. Indeed the concept of mounting multiple masses on a PZT beam to widen the bandwidth has been proposed and attempted by several researchers [74, 44]. It has been demonstrated by Soobum et al. [44] that for a tapered two-mass piezoelectric beam, the usable bandwidth of the harvester is significantly improved due to the two resonant peaks in the frequency range between 20 to 120 Hz.

Amongst the models presented in the literature there is a lack of an analytical model for a PZT beam mounted with multiple masses. Such a model is useful to the design of a multi-modal structure that has specific resonant frequencies. Other than boundary conditions considered in a single-mass beam, transition conditions emerge in the multiple-mass beam, which is clearly demonstrated in the derivation of the double-mass PZT beam model. In addition, the eigenfunctions that arise from modal analysis are of particular importance to piezoelectric benders. Given that the strain is proportional to the output voltage, the polarity change of strain along the piezoelectric beam associated with high vibration modes can result in voltage cancellation. This effect can be minimised by segmenting the electrodes on the beam where the strain is zero. Accurate mode shapes obtained from eigenfunctions can pinpoint the zero-strain locations for each vibration mode.

This chapter starts with solving the homogeneous problem of free vibration of a double-mass cantilever, from which the undamped equation of motion is derived using Hamilton's principle. This is followed by a modal analysis, from which eigenfunctions and natural frequencies are determined. A forced vibration problem is then considered and solved analytically for output voltage and relative displacement of the PZT cantilever. It then shows how the electrode segmentation can be incorporated into the model. Finally, results for experimental validation are presented, followed by conclusions.

5.2 Model Derivation

PZT bimorph, a composite material that consists of two piezoelectric layers separated by a reinforced substrate layer, is commonly used for vibration energy harvesting. When subject to cyclic bending, the compression and tension of the two piezoelectric layers lead to charge separation, which results in an AC voltage. Figure 5.1 shows a two-mass bimorph cantilever. In the development of the mathematical model, the cantilever is considered as two serially connected single-mass beam segments of lengths L_1 and L_2. Each associates coordinates x_1 and x_2 respectively as shown in Figure 5.1. M_{tn} is the mass and I_{tn} is the mass's

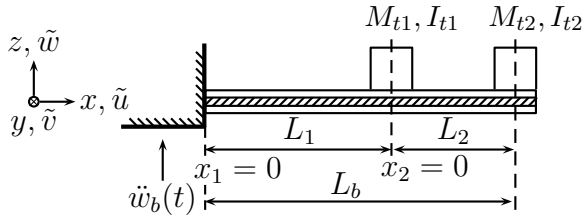

Figure 5.1: Two-layer PZT cantilever with two end masses.

moment of inertia with respect to their central axis that is parallel to the y-axis, where the subscript n is the index of the two beam segments. The linear density (mass per unit length) of the beam is assumed to be constant m_n. The absolute and relative vertical displacement for each segment are denoted by $\tilde{w}_n(x,t)$ and $w_n(x_n,t)$, respectively. The base of the beam is subject to acceleration $\ddot{w}_b(t)$ in the vertical direction. Note that the absolute displacement is the sum of the base displacement and the relative beam displacement, i.e. $\tilde{w}_n(x_n,t) = w_b(t) + w_n(x,t)$. The cross section of the cantilever is the same as the sketch depicted in Figure 4.2, therefore, the following relationship for the second moment of area in (4.3) still holds. Up to this point, the premise is that each segment of the PZT beam may have a different second moment of area I_1 and I_2. This applies to a beam with variable cross sectional profile such as a tapered beam.

5.2.1 Hamilton's Principle

Hamilton's principle is a variational method in which multi-physics modelling can be easily incorporated. Due to the multi-physics nature of vibration-based energy harvesting, the generalised Hamilton's principle is a suitable method to derive the model from the mechanical and electrical energy, and the external work applied. The derivations for a PZT beam with no proof mass are detailed by Sodano et al. [31] for the Rayleigh Ritz formulation and De Marqui et al. [36] for the FEM routines. Compared to a double-mass PZT beam, the major difference lies in the eigenfunctions. Since for the undamped homogeneous problem the electromechanical equations are decoupled, only the mechanical system of the double-mass beam is considered in the derivation using Hamilton's principle. This approach allows us to focus on deriving the eigenfunctions while keeping the mathematics more manageable. The electromechanical coupling effects, mechanical damping and external excitations are considered after the eigenfunctions are derived. In the absence of external excitations, the equations of motion, boundary and transition conditions for the homogeneous problem are derived from Hamilton's principle,

$$\delta \int_{t_1}^{t_2} (T - U)\,\mathrm{d}t = 0, \tag{5.1}$$

where T is the total kinetic energy including both translational and rotational energy of each mass, and U is the internal strain energy. In the succeeding equations, the notations "prime" and "dot" are used for partial derivatives with respect to x_i and t, respectively. The expression for the kinetic energy is

$$\begin{aligned} T = {} & \frac{1}{2}\int_0^{L_1} m_1 \dot{w}_1^2(x_1,t)\,\mathrm{d}x_1 + \frac{1}{2} M_{t1}\dot{w}_1^2(L_1,t) + \frac{1}{2} I_{t1}\dot{w}_1'^2(L_1,t) \\ & + \frac{1}{2}\int_0^{L_2} m_2 \dot{w}_2^2(x_2,t)\,\mathrm{d}x_2 + \frac{1}{2} M_{t2}\dot{w}_2^2(L_2,t) + \frac{1}{2} I_{t2}\dot{w}_2'^2(L_2,t), \end{aligned} \tag{5.2}$$

and the strain energy of the beam U is defined as

$$U = \frac{1}{2}\int_0^{L_1} Y_{p1} I_1 w_1''^2(x_1,t)\,\mathrm{d}x_1 + \frac{1}{2}\int_0^{L_2} Y_{p2} I_2 w_2''^2(x_2,t)\,\mathrm{d}x_2. \tag{5.3}$$

To solve this fourth order coupled partial differential equations (PDEs), a total of four boundary conditions and four transition conditions are required. Among which, two boundary conditions at $x_1 = 0$ and two transition conditions at $x_1 = L_1$ need to be imposed based on the mechanical configuration. In the case of a cantilever, these two boundary conditions are

$$w_1(0,t) = 0,\ w_1'(0,t) = 0. \tag{5.4}$$

At the transition where the two segments are joined, the displacements and deflection angles are equal for all time. This leads to the following transition conditions

$$w_1(L_1,t) = w_2(0,t),\ w_1'(L_1,t) = w_2'(0,t). \tag{5.5}$$

By substituting these four conditions (5.4) and (5.5) into (5.1), Hamilton's principle yields the equation of motion

$$m_n \ddot{w}_n(x_n,t) + Y_{pn} I_n w_n''''(x_n,t) = 0 \quad \forall\, n = 1,2, \tag{5.6}$$

the other two transition conditions

$$Y_{p1} I_1 w_1'''(L_1,t) - Y_{p2} I_2 w_2'''(0,t) - M_{t1} \ddot{w}_1(L_1,t) = 0, \tag{5.7}$$

$$Y_{p1} I_1 w_1''(L_1,t) - Y_{p2} I_2 w_2''(0,t) + I_{t1} \ddot{w}_1'(L_1,t) = 0, \tag{5.8}$$

and the other two boundary conditions

$$Y_{p2} I_2 w_2'''(L_2,t) - M_{t2} \ddot{w}_2(L_2,t) = 0, \tag{5.9}$$

$$Y_{p2} I_2 w_2''(L_2,t) + I_{t2} \ddot{w}_2'(L_2,t) = 0. \tag{5.10}$$

5.2.2 Modal Analysis

To recapitulate, a total of ten partial differential equations have been obtained, consisting of two equations of motion (5.6), four boundary conditions (5.4), (5.9) and (5.10), and four transition conditions (5.5), (5.7) and (5.8). The aim is to find the solutions for the two equations of motion that satisfy all the eight boundary and transition conditions. This can be done analytically by separating the spatial and temporal domains and hence express the ten equations as ordinary differential equations (ODE). In modal analysis most attention is given to the spatial domain boundary and transition conditions, because they contain information of natural frequencies and coefficients of the eigenfunctions. Note that the modal analysis is based on the mechanical part of the undamped and homogeneous problem of (5.6). The relative displacement of each beam segment can be expanded as

$$w_n(x_n,t) = \sum_{r=1}^{\infty} \phi_{rn}(x_n)\eta_{rn}(t) \quad \forall\, n = 1,2, \tag{5.11}$$

where $\phi_{rn}(x)$ is the mass normalized eigenfunction and $\eta_{rn}(t)$ is the time dependent amplitude of the rth mode of vibration. So far the two beam segments can have a different linear density m_n and flexural rigidity $Y_{pn}I_n$. To proceed with the analysis, however, keeping the property of each segment distinct can lead to complicated expressions that require computer aid programs to solve (both symbolically and numerically). For the purpose of showing the derivation without having to deal with the unnecessary complexity, the linear density and the flexural rigidity of the two segments are assumed to be constant and identical, i.e.

$$\frac{m_1}{Y_{p1} I_1} = \frac{m_2}{Y_{p2} I_2} = \frac{m}{Y_p I}. \tag{5.12}$$

In practice, these assumptions correspond to a rectangular PZT beam with two identical masses on any arbitrary locations. Furthermore, it is convenient to define β_r as

$$\beta_r^4 = \frac{m}{Y_p I}\omega_r^2. \tag{5.13}$$

Substituting (5.11) - (5.13) into (5.4) - (5.10) yields the ODE

$$\phi_{rn}''''(x_n) - \beta_r^4 \phi_{rn}(x_n) = 0 \quad \forall\, n = 1, 2, \tag{5.14}$$

subject to boundary conditions

$$\phi_{r1}'(0) = 0, \tag{5.15}$$

$$\phi_{r1}(0) = 0, \tag{5.16}$$

$$\phi_{r2}'''(L_2) + \beta_r^4 \frac{M_{t2}}{m}\phi_{r2}(L_2) = 0, \tag{5.17}$$

$$\phi_{r2}''(L_2) - \beta_r^4 \frac{I_{t2}}{m}\phi_{r2}(L_2) = 0, \tag{5.18}$$

and transition conditions

$$\phi_{r1}(L_1) - \phi_{r2}(0) = 0, \tag{5.19}$$

$$\phi_{r1}'(L_1) - \phi_{r2}'(0) = 0, \tag{5.20}$$

$$\phi_{r1}'''(L_1) - \phi_{r2}'''(0) + \beta_r^4 \frac{M_{t1}}{m}\phi_{r1}(L_1) = 0, \tag{5.21}$$

$$\phi_{r1}''(L_1) - \phi_{r2}''(0) - \beta_r^4 \frac{I_{t1}}{m}\phi_{r1}'(L_1) = 0. \tag{5.22}$$

Equation (5.14) derived from the equations of motion is the classic Euler-Bernoulli beam equation , whose general solution can be expressed in the form

$$\begin{aligned}\phi_{rn}(x_n) = {} & a_{n1}\sin(\beta_r x_n) + a_{n2}\cos(\beta_r x_n) \\ & + a_{n3}\sinh(\beta_r x_n) + a_{n4}\cosh(\beta_r x_n).\end{aligned} \tag{5.23}$$

To find the specific solution, coefficients $\mathbf{a} = [a_{11} \dots a_{24}]^T$ are determined such that all boundary and transition conditions are satisfied. Substituting (5.23) to (5.15) - (5.22) yields a linear system of equation in the form

$$\mathbf{K}\mathbf{a} = \mathbf{0}, \tag{5.24}$$

where $\mathbf{K}$ is a 8×8 matrix. In order to have a non-trivial solution, the determinant of $\mathbf{K}$, i.e. the characteristic equation must be equal to zero. Solving this equation for β_r, the undamped natural frequencies ω_r can be obtained from (5.24) with (5.13). Merging the two coordinates x_1 and x_2 used for each segment, the eigenfunctions of the complete beam $\phi_r(x)$ can be written with Heaviside functions as

$$\phi_r(x) = \phi_{r1}(x)H(L_1 - x) + \phi_{r2}(x - L_1)H(x - L_1), \tag{5.25}$$

where x is the coordinate of the entire beam from $x = 0$ to $x = L_b$. Since the determinant of $\mathbf{K}$ is zero, there are infinitely many solutions for $\mathbf{a}$. The eigenfunctions can be massed normalized to give a unique solution, which fulfils the following orthogonality conditions

$$\begin{aligned} &\phi_{s1}(L_1)M_{t1}\phi_{r1}(L_1) + \phi'_{s1}(L_1)I_{t1}\phi'_{r1}(L_1) \\ +\ &\phi_{s2}(L_2)M_{t2}\phi_{r2}(L_2) + \phi'_{s2}(L_2)I_{t2}\phi'_{r2}(L_2) \\ +\ &\int_0^{L_b} m\phi_s(x)\phi_r(x)\,dx = \delta_{rs}, \end{aligned} \tag{5.26}$$

where δ_{rs} is equal to unity for $r = s$ and zero for $r \neq s$.

5.2.3 Solution for Base Excitation

To derive the analytical solution with the presence of cyclical base excitation, a harmonic input function is assumed, which has the from

$$\ddot{w}_b(t) = A_0 e^{j\omega t}. \tag{5.27}$$

To determine the forcing response, it is necessary to consider the mechanical damping and piezoelectric effects. Substitution of this approach into the equation of motion (5.6) gives [72] :

$$\begin{aligned} m\ddot{w}(x,t) + c_s I\dot{w}''''(x,t) + Y_p I w''''(x,t) + \vartheta v_o(t) \\ \times\left[\frac{\mathrm{d}\delta(x)}{\mathrm{d}x} - \frac{\mathrm{d}\delta(x-L_1)}{\mathrm{d}x}\right] = -f_{ext}(t), \end{aligned} \tag{5.28}$$

where c_s is the equivalent strain rate damping constant, $v_o(t)$ is the voltage output and $f_{ext}(t)$ is the external forcing function. Definition of the electromechanical backward coupling term ϑ is exactly the same as (4.23). When subject to base excitation, the beam experiences forces due to the continuously distributed mass of the beam itself as well as the two rather concentrated proof masses. This is included by the external forcing term $f_{ext}(t)$ in (5.28) as

$$f_{ext}(t) = \ddot{w}_b(t)\left[m + M_{t1}\delta(x-L_1) + M_{t2}\delta(x-L_b)\right]. \tag{5.29}$$

The external forcing function has an unit of *force* per *length*. Using the eigenfunctions $\phi_r(x)$ given by (5.25), the solution for the displacement of the *entire* double-mass beam is written as

$$w(x,t) = \sum_{r=1}^{\infty} \phi_r(x)\eta_r(t). \tag{5.30}$$

Next, the ODE of the time domain function $\eta_r(t)$ is obtained by Galerkin method [32]. After substituting (5.30) to (5.28), multiplying $\phi_r(x)$ and integrating with respect to x in both sides of (5.28), the equation of motion is reduced to

$$\ddot{\eta}_r(t) + 2\xi_r\omega_r\dot{\eta}_r(t) + \omega_r^2\eta_r(t) + \chi_r v_o(t) = -f_r(t), \tag{5.31}$$

where ξ_r is the rth mode damping ratio and

$$\chi_r = \vartheta\phi_r'(L_b). \tag{5.32}$$

The external forcing function becomes

$$\begin{aligned} f_r(t) &= \int_0^{L_b} f_{ext}(t)\phi_r(x)\,\mathrm{d}x, \\ &= F_r e^{j\omega t}, \end{aligned} \tag{5.33}$$

where

$$F_r = A_0\left[m\int_0^{L_b}\phi_r(x)\,\mathrm{d}x + M_{t1}\phi(L_1) + M_{t2}\phi(L_b)\right]. \tag{5.34}$$

Equation (5.31) describes the electromechanical coupling of the system from the mechanical perspective. Another equation is needed to describe the electrical behaviors and its influence towards the mechanical system. This equation is derived from the second piezoelectric constitutive relation [70]:

$$D_3 = d_{31}Y_pS_1 + \varepsilon_{33}^S E_3, \tag{5.35}$$

As detailed by Erturk and Inman [72], for a pure resistive load R_L, the second coupled equation of motion can be written in the form

$$C_{pe}\dot{v}_o(t) - \sum_{r=1}^{\infty}\varphi_r\dot{\eta}_r(t) = -\frac{v_o(t)}{R_L}. \tag{5.36}$$

The definition of C_{pe} and φ_r can be found in (4.18a) and (4.37), respectively. The coupled ordinary differential equations (5.31) and (5.36) form the mechanical and electrical dynamic model of the double-mass PZT cantilever. They can be solved analytically using Laplace transform. Assuming the solution for the output voltage to be in the form $v_o(t) = V_o e^{j\omega t}$, solving (5.31) for $\eta_r(t)$ gives

$$\eta_r(t) = \frac{-F_r - \chi_r V_o}{\omega_r^2 - \omega^2 + j2\xi_r\omega_r\omega}e^{j\omega t}. \tag{5.37}$$

Therefore, the analytical solution for the *relative* displacement $w(x,t)$ under harmonic base excitation is obtained by substituting (5.37) and (5.25) into (5.30). The solution for voltage output can be determined by substituting (5.37) to (5.36) and rearranging for $v_o(t)$, which gives

$$v_0(t) = \frac{I_p}{C_{pe}j\omega + \frac{1}{Z_p} + \frac{1}{R_L}}e^{j\omega t}, \tag{5.38}$$

where I_p and Z_p, given by

$$I_p = -\sum_{r=1}^{\infty} \frac{j\omega F_r \varphi_r}{\omega_r^2 - \omega^2 + j2\xi_r\omega_r\omega}, \tag{5.39a}$$

$$Z_p = \frac{1}{\sum_{r=1}^{\infty} \frac{j\omega\chi_r\varphi_r}{\omega_r^2 - \omega^2 + j2\xi_r\omega_r\omega}} \tag{5.39b}$$

are the generated current and characteristic impedance, respectively. The beauty of this derivation is that its solution has a consistent form with the single mass PZT beam model derived in Chapter 4, therefore, the current source representation shown in Figure 5.2 still applies. Compare to the single mass model, the major

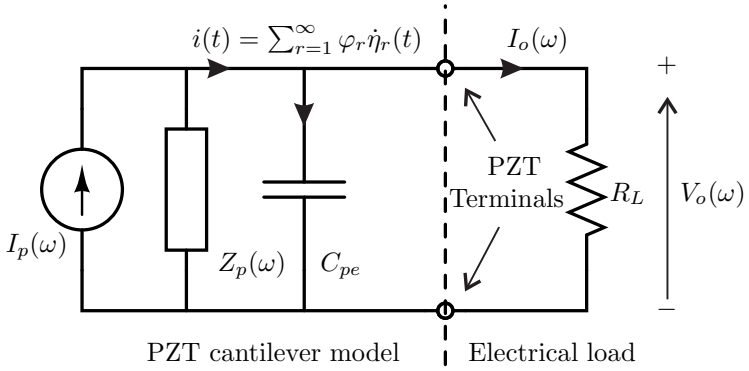

Figure 5.2: Electrical circuit representation of the double-mass PZT model connecting a resistive load.

difference of the double-mass model is the eigenfunctions $\phi_r(x)$ that satisfies the boundary and transition conditions. As a result, the expressions of the current output and characteristic impedance derived in the single mass PZT beam are directly applicable to the double-mass model.

5.2.4 Electrode Segmentation

According to the constitutive equations of piezoelectricity [70], the charge generated by the PZT material is proportional to the strain developed. For a cantilever, any vibration mode that is higher than the fundamental mode has a zero strain crossing. The change in polarity of strain leads to charge cancellation, reducing the power output of the second resonant frequency. This effect can be minimised by segmenting the electrodes on the PZT cantilever where the strain is zero. Note that in the first mode the voltage of the two segments are in phase, and the second mode out of phase as illustrated in Figure 5.3.

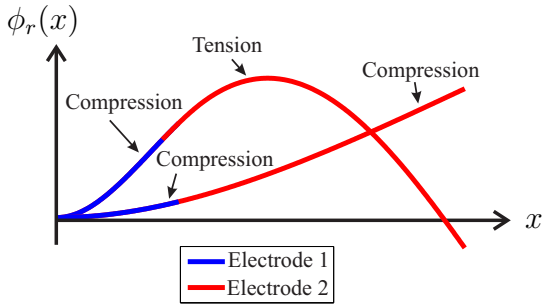

Figure 5.3: Eigenfunctions indicate polarities of the segmented electrodes in first mode are the same, but opposite in second mode.

In order to avoid charge cancellation for both vibration modes, the electrodes of each segment have to be rectified to DC before they merge. As illustrated in Figure 5.4, the beam is segmented at $x = L_s$ where strain is zero at second mode. The AC voltage of each segment is converted to DC through a bridge rectifier before being connected in series. The purpose of the the capacitor C_s is to minimize

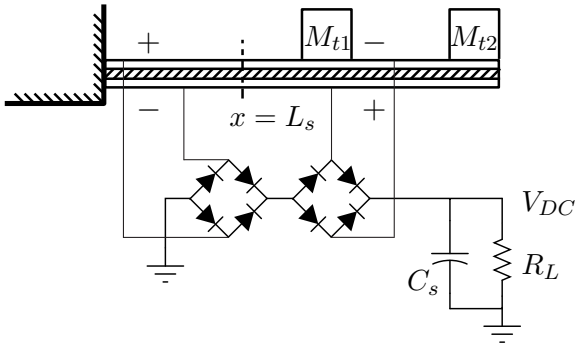

Figure 5.4: AC voltage from each segment of the cantilever is rectified to DC before connecting in series. Instantaneous direction of polarization for the 2nd vibration mode is shown.

the ripples of the DC voltage V_{DC}. To incorporate electrode segmentation in the model, it requires to re-examine the proportionality constant φ_r of the PZT source current in (5.36). According to (4.37), φ_r is proportional to $\phi_r'(L_b)$, which is the sum of area under the curve $\phi_r''(x)$ depicted in Figure 5.5. Given that the strain is proportional to $\phi_r''(x)$ such that

$$S_1(x) = -h_{pc}\phi_r''(x), \tag{5.40}$$

the charge cancellation is indeed caused by the subtraction of the areas A_{I} and A_{II}. To impose the two areas to the same polarity, the constant $\phi_r'(L_b)$ has to be modified to

$$\phi_{r,seg}'(L_b) = \Big[\big|\phi_r'(L_s)\big| + \big|\phi_r'(L_b) - \phi_r'(L_s)\big|\Big] \times \mathrm{sign}\Big(\phi_r'\left(L_b\right)\Big). \tag{5.41}$$

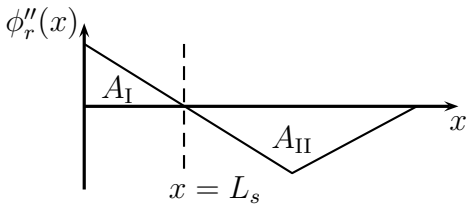

Figure 5.5: Strain equals zero at $x = L_s$, area cancellation is due to opposite polarities.

In (5.41) the polarities of $\phi'_{r,seg}(L_b)$ and $\phi'_r(L_b)$ are kept the same to assure the correct summation of $\phi'_{r,seg}(L_b)$ for all vibration modes. As a result, the polarity of individual term in the summation may appear different, indicating that charge cancellation of higher than the second mode still takes place within each segment. The harvester is expected to be operated within the first two vibration modes, where the charge cancellation of higher order modes is negligible. Hence the electrode segmentations for higher order modes are deemed unnecessary.

5.3 Experimental Validation

5.3.1 Stainless Steel Cantilever beam

A series of experiments were conducted to validate the analytical model derived in this chapter. As an initial investigation, a rectangular stainless steel beam mounted with two identical iron cubes was tested. Experiments conducted on this beam allows the validation to be focused on the eigenfunctions derived from the Hamilton's principle. Although the model was derived for piezoelectric beams, setting the voltage to zero would allow it to model stainless steel beams. The experimental set-up is shown in Figure 5.6. The key instruments involved in the experiment are: the laser vibrometer (A) that measures the velocity of an arbitrary point on the beam, the electromagnetic shaker (C) that generates base excitation, and the accelerometer (D) sits underneath of the clamp to measure the input acceleration. The damping ratios were determined using the logarithmic decrement technique based on the time waveform of an impulse response. The PULSE instrument was used to drive the shaker and log the measurement. The parameters and material properties used in the experiment are given in Table B.3 in Appendix B. The chosen beam has an aspect ratio of 13.2, hence it is reasonable to neglect the shear deformation and the rotary effects, which is in accordance with the assumptions of Euler-Bernoulli beam theory. In addition, the base acceleration was kept below 50 mg to preserve the linearity of the beam dynamics. Applying the same procedure as described in Section 4.6, the frequency response and mode shapes of the beam were measured. Figure 5.7 and 5.8 show the velocity frequency response of M_{t1} and M_{t2}, respectively. Note that the vibrometer measures the *absolute* velocity.

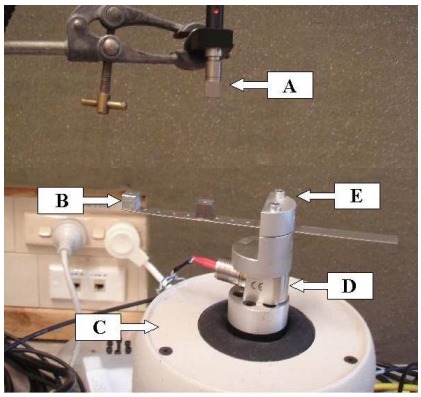

Figure 5.6: Experimental set-up of double mass stainless steel cantilever beam. (A) Vibrometer. (B) Two-mass beam. (C) Electromagnetic shaker. (D) Accelerometer. (E) Clamps

The results show that, quantitatively, both the frequencies and amplitudes pre-

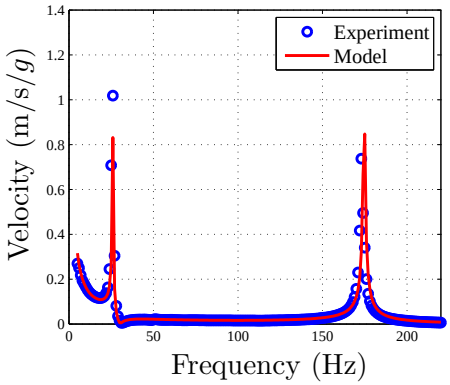

Figure 5.7: Velocity FRF of the first mass M_{t1}. The lower frequency peak is the 1st mode and the higher frequency peak is the 2nd mode.

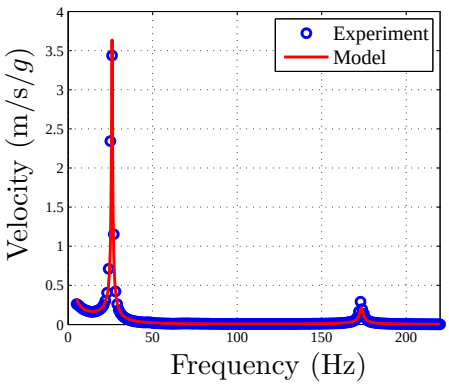

Figure 5.8: Velocity FRF of the second mass M_{t2}. The lower frequency peak is the 1st mode and the higher frequency peak is the 2nd mode.

dicted by the model agreed well with observation. It is interesting to see that the anti-resonance is very close to the low frequency peak at the first mode, but does not exist in the second mode.

Next, the mode shapes of the first two resonant modes are to be validated. This is done by separately exciting the beam at each of the two resonant frequencies. The velocity was then measured at several points along the beam where reflective tape was fitted. The mode shapes measured by this procedure, however, are not the mode shapes of the beam in a snapshot, but are rather the maximum velocity of each measured location. Therefore it corresponds to the absolute value of the

complex velocity solution in the model. The measurements of the first and second vibration modes are shown in Figure 5.9 and 5.10, respectively. In the mode shape

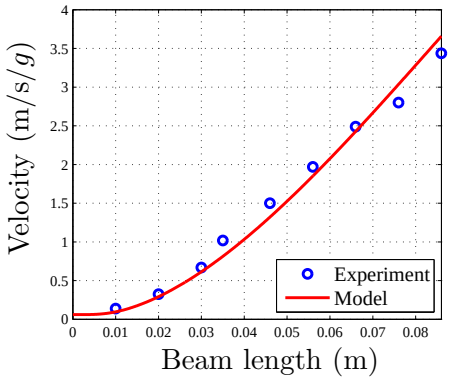

Figure 5.9: Mode shape at the 1st resonant frequency.

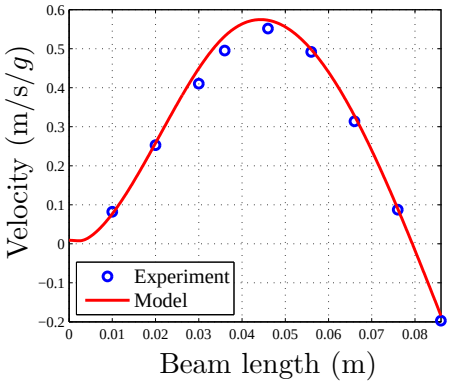

Figure 5.10: Mode shape at the 2nd resonant frequency.

measurements, the non-zero velocity at $x = 0$ corresponds to the *absolute* velocity of the vibrating base. In both figures, the experimental results of the mode shapes are in close agreement with the model. The experimental validation on the stainless steel beam provides the evidence that the eigenfunctions derived in this chapter can accurately determine the natural frequencies and frequency response of any point along the beam.

5.3.2 Piezoelectric Cantilever beam

To fully validate the derived double-mass model, experiments with a piezoelectric beam was conducted. The beam was made from a 5A4E 2-layer series poled piezoelectric sheet[1] from Piezo Systems, Inc. Two identical iron cubes are glued on the beam. The experimental set-up is shown in Figure 5.11. The PZT beam is fixed by a rigid aluminium clamp, which also serves as conductors for the electrodes on each side of the beam. Nylon bolts are used to secure the clamp while keeping it electrically insulated. Since the main interest is to validate the frequencies, mode shapes and the voltage output, the electrodes of the PZT beam are not segmented for power optimization. The instruments involved are the same as the ones used by the previous experiments, with the exception that LabVIEW™ with differential input and output modules from National Instruments™. are used to drive the shaker and log measurement results.The parameters and material properties involved in the experiment can be found in Table B.4 of Appendix B.

To measure the frequency response, firstly a swept-sine input is used to quickly identify the two resonant frequencies. To assure a steady state response, the beam

[1] 1 Part number T220-A4-503X.

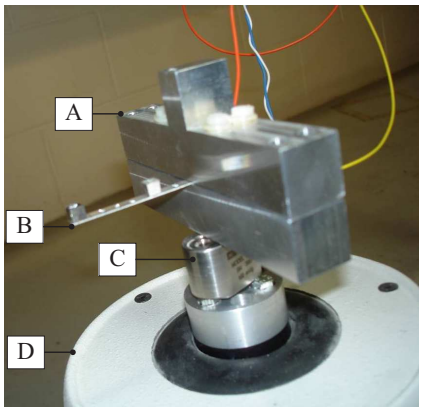

Figure 5.11: Experimental set-up. (A) Clamp. (B) Double-mass PZT beam. (C) Accelerometer. (D) Electromagnetic shaker.

is then excited sinusoidally with a fixed frequency for at least 2 seconds. The excitation frequency is incremented in steps of 10 Hz in the non-resonant region and 1 Hz around the resonant peaks, and the velocity of each mass and the voltage output are measured. Figures 5.12 and 5.13 show the velocity FRF of M_{t1} and M_{t2}, respectively. As can be seen, for both masses the overall velocity response

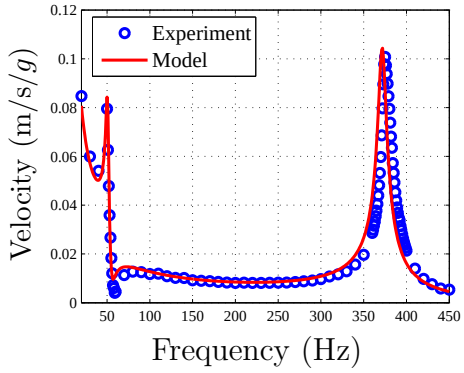

Figure 5.12: Velocity FRF of the first mass M_{t1}. The lower frequency peak is the 1st mode and the higher frequency peak is the 2nd mode.

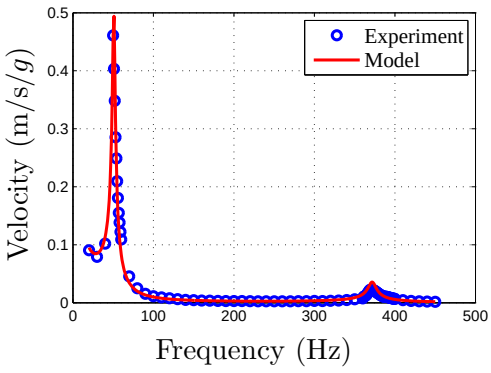

Figure 5.13: Velocity FRF of the second mass M_{t2}. The lower frequency peak is the 1st mode and the higher frequency peak is the 2nd mode.

and resonant frequencies closely match the experimental measurements. It is interesting to see that M_{t2} has very little amplitude at the second mode, this is due to its proximity to the stationary location of the beam as indicated in Figure 5.15. One major source of uncertainty is the mechanical damping ratios. It was observed that mechanical damping could vary noticeably for different excitation frequencies and amplitudes. Applying logarithmic decrement technique, the aver-

age mechanical damping ratios around the first and second resonant frequencies were determined. The exact position where the velocity was measured also contributed to the errors. This is because the laser spot that measures the velocity is approximately 2 mm in diameter, which results in a ±1 mm uncertainty. If the beam's gradient is relatively large at the measuring position, the error can be significant. Slight adjustments have been made to the model to compensate for these measurement uncertainties. In Figure 5.14, excellent agreement is also found between the measured voltage output and the model. cantilevers that are not in resonance contribute very little to the power output. This is also true for multimodal harvesters. In voltage validation, the low frequency peak has a higher value

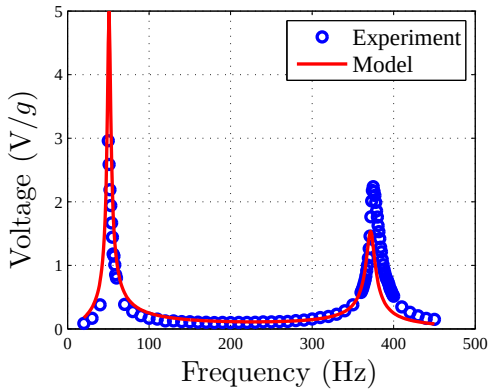

Figure 5.14: Voltage FRF, electrode segmentation was not implemented hence charge cancellation did occur.

than experiment and the high frequency peak a lower value than experiment. One of the major source of errors is the capacitance, which has a direct effect on the voltage output. The capacitance in the model is calculated based on the geometry parameters and properties provided by the PZT manufacturer. The already small capacitance (typically around 10 to 20 nF) can be changed dramatically due to the beam's condition and external factors. The electrode on each side of the beam, whose area is proportional to the capacitance, is a conductive layer of nickel with a thickness of only 0.5 μm. The actual area could be reduced if the nickel layer is wiped off sporadically during handling. Moreover, the total capacitance can be altered by the set-up of the experiment. In the presented set-up, the aluminium clamp and nylon bolts add extra capacitance to the circuit. These factors have not been taken into account in the estimation of the capacitance. Nonetheless, the model is able to produce satisfactory results that are valuable for design purposes.

With the same procedure carried out before, the mode shapes were constructed by the velocity measurement along the piezoelectric beam. The first and second mode shapes shown in Figure 5.15 are normalized by the velocity FRF of the free end. Although the *relative* velocity of the fixed end is zero, the non-zero velocities at the fixed end in Figure 5.15 correspond to the *absolute* velocity FRF of the vibrating

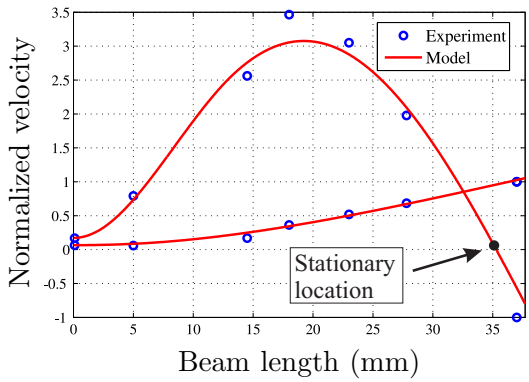

Figure 5.15: Normalised mode shapes of 1st and 2nd mode.

base. The uncertainty in laser positions mentioned earlier also contributed to the small inconsistency of the mode shape validation. Yet, the calculated mode shapes closely resemble the actual measurements.

5.4 Conclusions

While vibration-based energy harvesting technologies have become ever promising, narrow bandwidth is still the major challenge. Adding more proof masses is a cost effective and reliable way to enhance the usable bandwidth of a harvester. In this chapter, a continuum-based model for a double-mass bimorph cantilever is presented. By applying Hamilton's principle, the equations of motion together with all necessary boundary and transition conditions are derived. Undamped natural frequencies and the mass normalized eigenfunctions are determined through modal analysis. The steady state solution for harmonic base excitation is obtained. Both series and parallel connection for the bimorph are incorporated in the model through the definitions of some geometric variables. In addition, electrode segmentation for power output enhancement is incorporated into the model. As an incremental investigation, the derived model was firstly experimentally validated on a stainless steel beam with two masses. The results confirmed that the eigenfunctions can accurately determined the natural frequencies and amplitude of the beam. The model was then validated experimentally on a 2-layer piezoelectric beam with two proof masses. In the experiment, the resonant frequencies, velocity frequency response, voltage output and the mode shape of the first two vibration modes are measured and compared with modelling results. In all quantities com-

pared, the model showed excellent agreement with the actual measurements. High credibility means this model can be used to quickly evaluate the performance of a double-mass energy harvester, and design the two resonant frequencies and the power output to desired specifications. Depending on the required bandwidth, a broadband energy harvester can be implemented by an array of double-mass PZT beams for more compactness compared to its single-mass counterpart. The development of this model is an important step forward to solving the optimization problem of double-mass PZT harvesters, and to deriving a generalised model for a PZT beam with any number of proof masses.

6

Resonance Tuning by Impedance Matching

6.1 Introduction

While cantilever arrays do achieve a wide bandwidth response, they do not utilise the proof masses efficiently due to the fact that the cantilevers that are not in resonance contribute very little to the power output. This is also true for multi-modal harvesters, when they are excited in certain vibration modes, some segments of the beam contribute very little power compared to the others. Since fundamentally power output is proportional to the weight of the resonating proof mass, it is important to maximise the proof mass within the allowable space and weight limits where possible. A tunable harvester that can shift its resonant frequency with a single proof mass is desirable to eliminate the redundancy. Moreover, the harvester can also be detuned away from resonance to protect the PZT beam from excessive bending, in the event of excessive vibration levels. A resonance tuning system can be realised either mechanically or electrically. As briefly discussed in the literature review, Chapter 2, the resonant frequency of a PZT beam can be shifted electrically by impedance matching, which can be further categorised into modulus and conjugate matching. The former refers to an electrical load whose impedance is the same as the modulus of the PZT impedance, whereas the latter refers to an electrical load whose impedance is the conjugate of the PZT impedance. Compared to a mechanical implementation, an electrical tuning system can greatly simplify the mechanical design, and eliminate moving parts for the tuning purpose, hence it is generally more reliable and of lower cost. Kong et al. [57] implemented a circuit to automatically match the modulus of the PZT cantilever, resulting in a tuning range of about 12 % of the central frequency. Luo and Hofmann [59] demonstrated a conjugate matched system that has a tunable frequency range of about 14 % of the central frequency. Despite the fact that these presented systems use an active tuning implementation that consumes power at all time, they are the evidence that

resonance tuning can be realised electrically. This chapter explores the feasibility of an electrically semi-active tuning scheme. Of particular notice from the literature is that the frequency range by electrical tuning is relatively small compared to a mechanical tuning implementation. An improved PZT continuum model derived in this chapter explains why the tuning range is so limited and how to maximise the range. Despite the limited tuning range, the advantages of an electrically tuning system renders it an attractive solution for small frequency range harvesters and for fine tuning purposes to complement a mechanical tuning system.

This chapter is organised as follows: in Section 6.2, an improved continuum PZT cantilever model is derived. In Section 6.3, the experimental validations of the model on a modulus matched load and a rectifier with a capacitive load are presented. The concept of a semi-active conjugate matching circuit is proposed in Section 6.4. The performance and load requirements of the system are discussed based upon the modelling results. Lastly, conclusions are given in Section 6.5.

6.2 An Improved Continuum Model

In Section 4.3 of Chapter 4, a continuum model of PZT cantilevers was derived. To recap, the model is for an two-layer PZT cantilever beam with a tip mass shown in Figure 6.1, whose base experiences a vertical vibration $\ddot{w}_b(t)$. The continuum

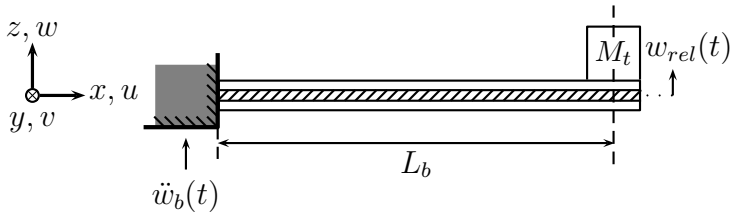

Figure 6.1: A cantilever bimorph with an end mass, sketch not to scale.

model that describes the dynamic response is the system of ordinary differential equations:

$$\ddot{\eta}_r(t) + 2\xi_r\omega_r\dot{\eta}_r(t) + \omega_r^2\eta_r(t) + \chi_r v_o(t) = -f_r(t), \tag{6.1}$$

$$C_{pe}\dot{v}_o(t) - \sum_{r=1}^{\infty}\varphi_r\dot{\eta}_r(t) = -\frac{v_o(t)}{R_L}. \tag{6.2}$$

Solving the ODEs for $\eta_r(t)$ and $v_o(t)$, the velocity and voltage response of the PZT cantilever can be determined. The analytical solutions are

$$\eta_r(t) = \frac{-F_r - \chi_r V_o}{\omega_r^2 - \omega^2 + j2\xi_r\omega_r\omega}e^{j\omega t}, \tag{6.3}$$

$$v_o(t) = \frac{I_p}{C_{pe}j\omega + \frac{1}{Z_p} + \frac{1}{R_L}} e^{j\omega t}. \tag{6.4}$$

The voltage output is equivalent the to electrical circuit in Figure 6.2.

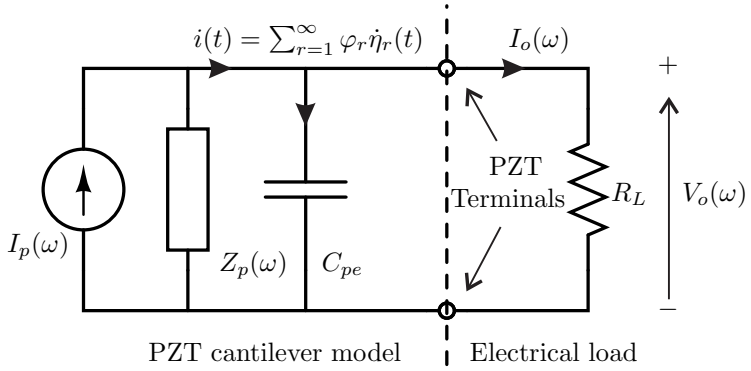

Figure 6.2: Current source circuit representation of the PZT continuum model connecting a resistive load.

Compared to conjugate matching, modulus matching is relatively easier to implement but gives a smaller tuning range. Although the continuum model was validated with resistive loads showing excellent accuracy, applying the model to a conjugate matched system will give unrealistic results. To prove that is the case, the resistive load R_L in Figure 6.2 can be substituted by a conjugate matched load Z_L, and a constant[1] power output for all excitation frequencies is obtained. This is due to the fact that the continuum model did not consider the losses, which were negligible with a purely resistive load but significant for a conjugate matched load due to the relatively high voltages developed across the PZT material. Therefore, modification is needed to take the losses into account for a conjugate matched system.

In any piezoelectric energy harvesters, two major losses associated with the PZT layer are the polarisation and contact ohmic losses. Polarisation losses are due to the non-ideal dielectric property of the PZT crystal. Unrealistic prediction of a constant power output over the whole range of frequency for a conjugate matched system is also obtained by Luo and Hofmann [59], who used an alternative circuit model. Without identifying the composition of the losses, they imposed a percentage efficiency on the system. Polarisation losses have been recognised by several researchers [75, 76] who added a constant resistor in parallel with the circuit in their models.

In fact, polarisation losses are frequency dependent. For non-ideal dielectric materials, there exist resistive as well as reactive components in its polarisation current

[1]Constant power when only the first mode of vibration is used, and near constant power when higher vibration modes are included

[77]. The ratio of the two components is called loss tangent $\tan\theta_{LT}$, which is the reciprocal of the quality factor Q. Either of these quantities is usually provided by the material manufacturer. polarisation losses are caused by the resistive component, they can be modelled by a frequency dependent resistor $R_p(\omega)$ in *parallel* with the circuit in Figure 6.2, where

$$R_p(\omega) = (1 + Q^2)\frac{\tan\theta_{LT}}{\omega C_{pe}}. \tag{6.5}$$

Ignorance of polarisation losses is not unreasonable, because the PZT internal resistance is normally in the order of 10 MΩ. Under normal condition (not conjugate matching) the losses are negligible.

The contact ohmic losses, on the other hand, are due to the resistance on the very thin conducting layer of the piezoelectric material, these losses are independent of input frequency. On both sides of a PZT layer, a layer of conducting material is applied to serve as the electrical terminals. The thickness of this conducting layer is typically less than one micron, making it potentially a significant source of ohmic losses. In a normal configuration, the terminal wires are connected to the end of the beam on the conducting layer (see Figure 6.3 (A)). The conducting layers

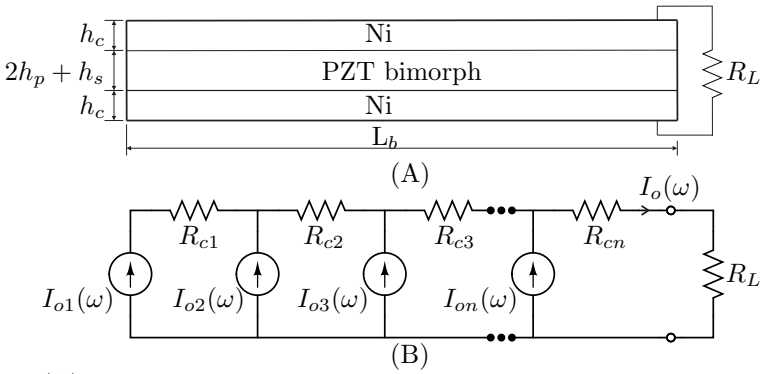

Figure 6.3: (A) Showing a PZT bimorph with a nickel conducting layer on both sides, sketch not to scale. A load resistor is connected at one end of the electrodes. (B) Showing the equivalent current propagation circuit model.

that are in contact with the conductive substrate have a much larger thickness so the resistance is negligible. As the produced current propagates from the left hand side of the beam towards the electrical wires, the current gets higher, so do the ohmic losses. This can be modelled by a circuit with infinitely many current sources and resistors shown in Figure 6.3 (B). The resistance of both conducting layers combined is denoted by R_c,

$$R_c = 2\rho_e\frac{L_b}{b_e h_c}, \tag{6.6}$$

where ρ_e is the resistivity of the material. For nickel, it is 6.99×10^{-8} Ω·m at $20\,^oC$. The effective width b_e is used in (6.6) to comply with both series and parallel

connection cases. The following two constants, average current per length i_x and average resistance per length R_{cx}, can be determined as

$$i_x = \frac{I_o}{L_b} \text{ and } R_{cx} = \frac{R_c}{L_b}, \tag{6.7}$$

respectively. The power losses can be evaluated from the integral

$$P_L = \int_0^L (i_x x)^2 R_{cx} \, \mathrm{d}x = \frac{1}{3} I_o^2 R_c. \tag{6.8}$$

Since power losses can be also expressed by an effective resistance as $P_L = I_o^2 R_{ce}$, comparing it to (6.8) the following relationship can be drawn

$$R_{ce} = \frac{1}{3} R_c. \tag{6.9}$$

Including the polarisation losses and ohmic contact losses, and with a general electrical load Z_L, the circuit representation of the improved PZT model is shown

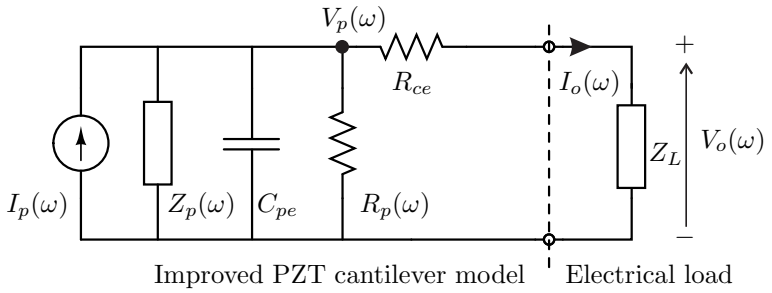

Figure 6.4: Current source circuit representation of the improved PZT distributed parameter model that includes polarisation and ohmic losses. The PZT beam connects to an electrical load with arbitrary impedance Z_L.

in Figure 6.4. The improved model is described by the coupled system of ODEs

$$\ddot{\eta}_r(t) + 2\xi_r \omega_r \dot{\eta}_r(t) + \omega_r^2 \eta_r(t) + \chi_r v_p(t) = -f_r(t), \tag{6.10a}$$

$$C_{pe} \dot{v}_p(t) - \sum_{r=1}^{\infty} \varphi_r \dot{\eta}_r(t) + \frac{v_p(t)}{R_p(\omega)} = -\frac{v_p(t)}{R_{ce} + Z_L}. \tag{6.10b}$$

In the frequency domain, the solution for the PZT voltage $V_p(\omega)$ becomes

$$V_p(\omega) = \frac{I_p(\omega)}{C_{pe} j\omega + \frac{1}{Z_p(\omega)} + \frac{1}{R_p(\omega)} + \frac{1}{R_{ce}+Z_L}}. \tag{6.11}$$

The output current and voltage are

$$I_o(\omega) = \frac{V_p}{R_{ce} + Z_L} \text{ and } V_o(\omega) = I_o(\omega) Z_L, \tag{6.12}$$

respectively. The relative displacement of the beam can be determined by substituting (6.11) into (6.10a) and solving for $\eta_r(t)$. Although the value of $R_p(\omega)$ is relatively high, and R_{ce} is relatively very low, if the electrical load is a frequency varying complex load that conjugately matches the impedance of the PZT beam at all frequencies, the voltage and current are growing higher as the excitation frequency deviates from resonance. In these circumstances, modelling results will not be valid if the polarisation and ohmic losses are not taken into account. Combining the losses with the internal capacitance, the Thévenin equivalent circuit shown in Figure 6.5 can be obtained. The total source impedance $Z_s(\omega)$ for the improved

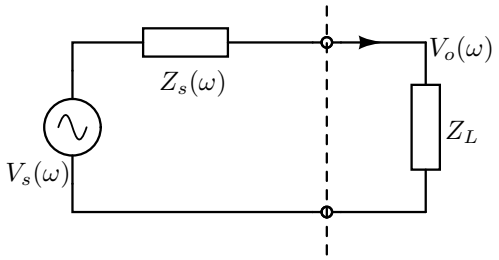

Figure 6.5: Thévenin equivalent circuit of the improved PZT cantilever model.

model can be expressed as

$$Z_s(\omega) = \frac{1}{C_{pe}j\omega + \frac{1}{Z_p(\omega)} + \frac{1}{R_p(\omega)}} + R_{ce}, \tag{6.13}$$

and the source voltage is determined by $V_s(\omega) = I_p(\omega)Z_s(\omega)$. Even with the losses included, the improved model is formulated in a way that is compatible with the generalised model developed in Section 4.4. Therefore, much of the analysis carried out in that section can be directly applied to the improved model.

6.3 Experimental Validation

6.3.1 Mechanical set-up

To validate the PZT cantilever model and its analytical solution derived in this chapter, experiments are performed on a piezoelectric cantilever beam with a single tip mass, which is shown in Figure 6.6. The set-up of the experiment consists of two parts: the PZT cantilever beam (mechanical) and the interfacing circuit (electrical). The mechanical set-up is identical to the one that validates the single mass PZT beam. A 2-layer series poled piezoelectric transducer from Piezo Systems, Inc., part number T220-A4-203X is fasten by the aluminium clamp. The accelerometer measures the base acceleration, and the vibration source is provided

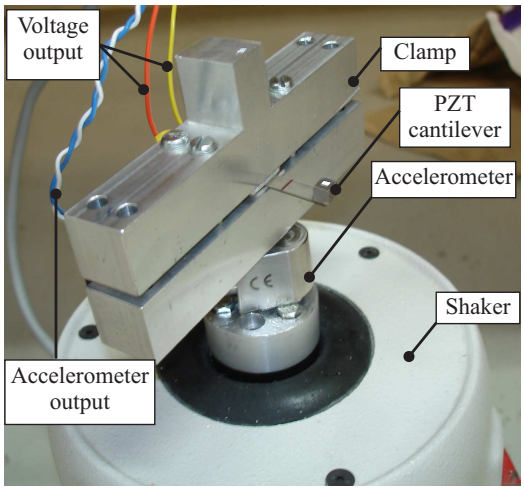

Figure 6.6: Experimental set-up of the PZT cantilever beam.

by the electromagnetic shaker. The velocity response of the tip mass is measured by the laser vibrometer (not shown in figure). The experiment is conducted using LabVIEW™ and differential input module NI 9239 and output module NI 9269 from National Instruments™. A LabVIEW™ program is created to take measurement automatically over a specified frequency range at a resolution of 1 Hz. For each excitation frequency, LabVIEW™ drives the shaker for 5 seconds for the PZT beam to reach steady state, then it takes a recording of the time waveform for all channels. In run time, the recorded time waveforms are converted to Fast Fourier Transform (FFT) spectrum. The data is then logged to csv files for post processing in Matlab®. For the electrical part, as will be explained later in this chapter, validating a conjugate matched system can be very challenging. Since the aim here is to validate the improved PZT model, two much more achievable circuits are chosen: the optimal resistive load for modulus matching and a bridge rectifier with a capacitive load. The hypothesis is that if the circuit representation of the improved model in Figure 6.4 can accurately predict the dynamics of the PZT at high voltages, then the model is reliable for the analysis of a conjugate matched system, or any electrical load that is connected to the PZT by applying circuit theories.

6.3.2 Optimal resistive load for modulus matching

Modulus matching refers to a system with an optimal resistive load that always matches the modulus of the source impedance for all excitation frequencies. For each frequency, the optimal resistance value is the modulus of Equation (6.13). The main purpose of this experiment is to show that, by considering both polarisation and contact losses, the accuracy of the model is improved at the *high voltage* region.

In addition, the experiment is also aimed to confirm the effectiveness of shifting the resonant frequency by modulus matching. The dimension and material properties of the PZT beam can be found in Table B.5 of Appendix B. The only components in the real electrical circuit are a 1 kΩ resistor and a 1 MΩ potentiometer. When they are connected to the PZT beam, the circuit representation of the overall system is shown in Figure 6.7. By manually tuning the potentiometer, R_L is optimised

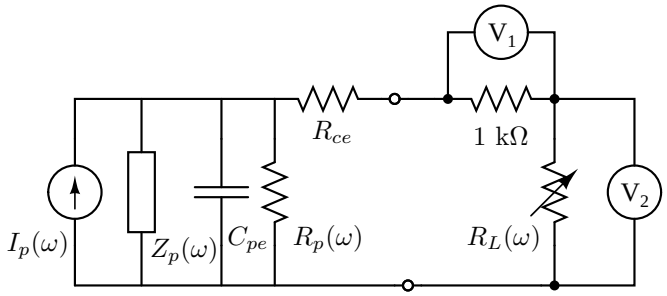

Figure 6.7: The circuit for modulus matching experimental validation, V_1 measures load current, and V_2 measures load voltage. The circuit includes polarisation losses $R_p(\omega)$ and ohmic losses R_{ce}. For each excitation frequency, $R_L(\omega)$ is adjusted to maximise power output.

for each frequency. Due to the high value of R_L, the actual load resistance can be distorted by the input impedance of the instruments and the probes. Hence the 1 kΩ resistor is used for sensing the load current. The actual load resistance is then obtained from the ratio of output voltage and current. In this experiment, four input data streams are logged simultaneously, they are the relative velocity of the tip mass, the base acceleration, the output voltage and current. The results are summarised in Figure 6.8. In the power and velocity response, the two peaks correspond to short and open circuit resonant frequencies. The absence of the first peak from the experiment is due to the limited sampling resolution, which is 1 Hz. Nonetheless, all four quantities of the improved model quantitatively agree well with the experiment. The original model, however, predicted a higher value for all four quantities around the frequency region where the output voltage is high. This has demonstrated the importance of considering the losses at high voltages. According to the power parameter values in Table B.7 of Appendix B, for the PZT beam used in the experiment, the ohmic losses R_{ce} only account for less than 0.5 % of the total losses. The frequency dependent PZT internal resistance $R_p(\omega)$ determined by the model is shown in Figure 6.9.

It is interesting to see that, at about 140 Hz, even R_p is as high as 12 MΩ, the total losses can be as much as 5.4 % of the total power produced by the harvester (according to Table B.7). This ratio can become much higher for a conjugate matched system at non-natural frequencies, which is detailed later in this chapter. As the input frequency keeps increasing, the claim by the PZT manufacturer that the PZT internal resistance is in the order of 10 MΩ becomes

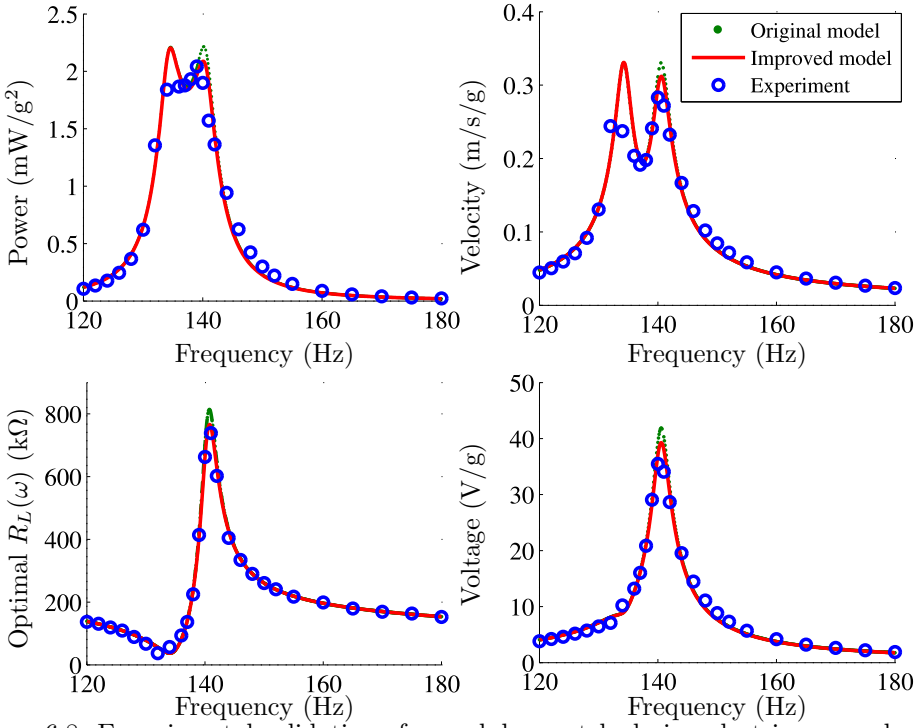

Figure 6.8: Experimental validation of a modulus matched piezoelectric energy harvester. Base acceleration applied is between 0.16 to 0.185 g. Each recorded point is the peak value of the FFT measurement at the responding frequency.

increasingly untrue. The lower of the PZT internal resistance, the higher the polarisation losses. In summary, both high voltage and high frequency can cause the PZT internal resistance a significant source of losses.

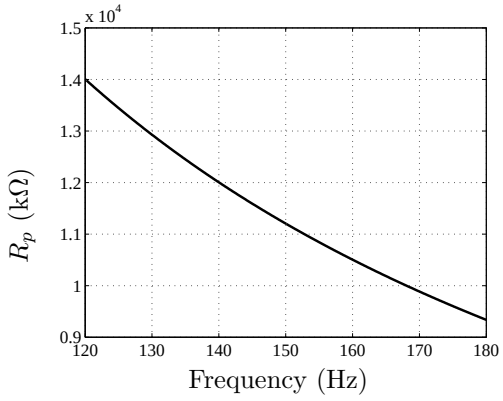

Figure 6.9: PZT internal resistance versus input frequency.

For frequency tuning, the experiment has verified that modulus matching is effective only for a limited frequency range. As explained in the theoretical study in

Section 4.5, the range of the two peaks in *relative terms* does not depend on the dimensions of the beam, but solely on the PZT material property: the coupling coefficient k_{31}. Thus the frequency range given by the PZT material PSI-5A4E chosen in the experiment is limited to 6 % from Ω_{sc} to Ω_{oc} by modulus matching. The load resistance curve indicates that from short to open circuit resonant frequency, the load resistance has to go through the extreme values, which can present a challenge to the implementation of automatic tuning. Nonetheless, a buck-boost converter that does modulus matching is proposed by Kong et al. [57]. Instead of modelling the system, Kong et al. obtained the load resistance v.s. frequency curve experimentally, whose profile is very similar to the one in Figure 6.8.

6.3.3 Capacitive load with bridge rectifier

To demonstrate that the improved model can simulate the PZT beam with any electrical load, a bridge rectifier and a capacitive load are connected to the PZT terminals. Figure 6.10 illustrates the circuit with a ceramic capacitor load whose internal series resistance is modelled explicitly by R_{esr}. This circuit is the most

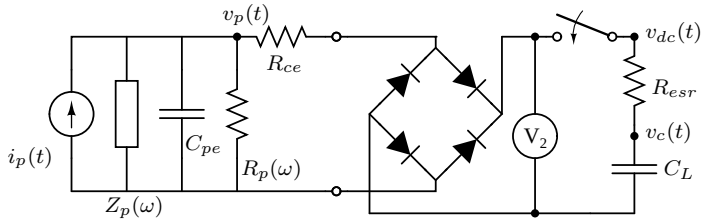

Figure 6.10: Current source circuit representation of the PZT beam model connects to bridge rectifier followed by a capacitive load.

likely to be used in practice. In energy harvesting systems where power efficiency and simplicity are the top priorities, passive bridge rectifiers are generally preferred over Pulse Width Modulation (PWM) rectifiers. A low loss capacitor is then used as an intermediate energy storage. Only when the capacitor's voltage is above a threshold the energy is extracted by enabling a DC-DC converter (not shown in circuit) in a very brief time, to transfer the energy to a bulk storage. This configuration is recommended by the manufacturers of the energy harvesting power conditioning ICs MAX17710 and LTC3588-1. The circuit in Figure 6.10 is the linkage where the mechanical and electrical domain interact. Therefore, understanding the dynamic behaviour of this circuit is important for the design of the overall electrical circuit.

To model this system, modifications have to be made to the equations of motion developed in the earlier section. The forward voltage drop per diode is denoted by

V_F. Starting from initial conditions as the switch is closed, when the diodes are not conducting, i.e. $|v_p(t)| - 2V_F \leqslant v_{dc}(t)$, the second coupled equation of motion (6.10b) needs to be rewritten as

$$C_{pe}\dot{v}_p(t) - \sum_{r=1}^{\infty} \varphi_r \dot{\eta}_r(t) + \frac{v_p(t)}{R_p(\omega)} = 0, \tag{6.14}$$

and

$$v_{dc}(t) = v_c(t),\ C_L\dot{v}_c(t) = 0. \tag{6.15}$$

which is just an open circuit condition with the polarisation losses included. The voltage of the capacitor remains the same. When the diodes are conducting, i.e. $|v_p(t)| - 2V_F > v_{dc}(t)$, the second coupled equation of motion becomes

$$C_{pe}\dot{v}_p(t) - \sum_{r=1}^{\infty} \varphi_r \dot{\eta}_r(t) + \frac{v_p(t)}{R_p(\omega)} = -\frac{v_p(t) - 2V_F - v_c(t)}{R_{ce} + R_{esr}}, \tag{6.16}$$

$$v_{dc}(t) = \frac{v_p(t) - 2V_F - v_c(t)}{R_{ce} + R_{esr}} R_{esr} + v_c(t), \tag{6.17}$$

$$C_L\dot{v}_c(t) = \frac{v_p(t) - 2V_F - v_c(t)}{R_{ce} + R_{esr}}. \tag{6.18}$$

Including the first coupled ODE (6.10a) and (6.14) - (6.18), a system of ODEs can be established and solved by numerical methods. A relatively small step size should be used, or it renders the solution noisy or even unstable.

The numerical values for the experimental set-up can be found in Table B.6 of Appendix B. The diode full bridge rectifier used in the circuit is DF005S, and the ceramic load capacitor measurement is presented in Table 6.1. An experimental

Table 6.1: Parameters & material properties of the PZT beam.

Description	Symbol	Value
Capacitor ESR	R_{esr}	0.54 Ω
Load capacitance	C_L	4.554 μF
Vol. drop per diode	V_F	0.6 V

validation of dynamic response in time waveform can be challenging due to the transient response. The transient response of the simulation is ideal but that of the experiment is compounded with signals from the transience of the shaker and the driving electronics in the experiment. Hence a switch is added to the test circuit to synchronise the transient response. The recorded data is processed in a way that at t = 1 s, the switch is turned on. The validation results for the input normalised tip mass velocity and output voltage are presented in Figures

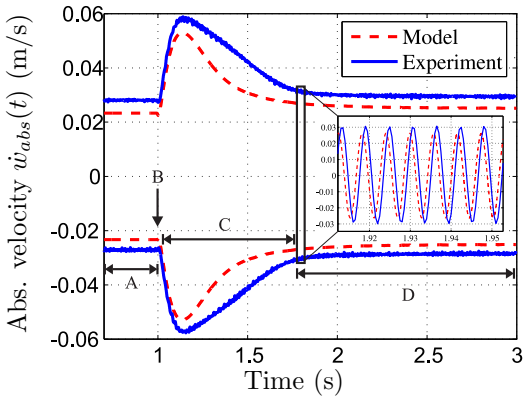

Figure 6.11: Validation results for the velocity time waveform of the tip mass. Both curves are the envelopes of the sinusoidal waveforms. Base acceleration is 0.2613 g at 171.3 Hz.

6.11 and 6.12, respectively. Unlike any of the previous presented measurement, the recordings in these two figures are *not* scaled by the base acceleration. This is because the measurement involved a bridge rectifier that has a fixed voltage drop, the output DC voltage cannot be simply scaled by the base acceleration. Therefore, the actual measured values for 0.2613 g of base acceleration are used.

As can be seen, quantitatively the model agree well with the experiments. Interesting observations on electrical and mechanical damping can be made in Figure 6.11. Looking at the energy flow of the system (in Figure 6.13) can help understand what has happened to the harvester before and after the switch has closed. During period A of Figure 6.11, the PZT is an open circuit, hence the damping consists of both mechanical and electrical damping. This can be reflected by the relatively low velocity amplitude. At the moment B when the switch is closed, the PZT is short circuited forcing the electrical damping to zero. However, the velocity of the mass cannot increase instantaneously because it requires time for the kinetic energy to build up and reach steady state. During period C when the load capacitor is charging, the electrical damping starts recovering. Firstly the proof mass starts to build up its momentum due to the reduced electrical damping. The interaction of velocity, voltage and electrical damping causes the velocity to reach maximum and then decrease. Over the whole period C, the electrical damping is changing due to the change of the output voltage. This is continued until the capacitor is fully charged up as can be seen in period D, where the PZT is back to open circuit condition.

Figure 6.12 shows the rectified DC voltage output. A zoom-in of the plot confirms that the pattern of the curves from the model and experiment are very consistent. From the design point of view, it is important to identify the capacitor voltage at which maximum power transfer occurs. This voltage corresponds to the point where $\frac{\mathrm{d}v(t)}{\mathrm{d}t}v(t)$ is maximum [78] as the capacitor being charged up. Keeping the

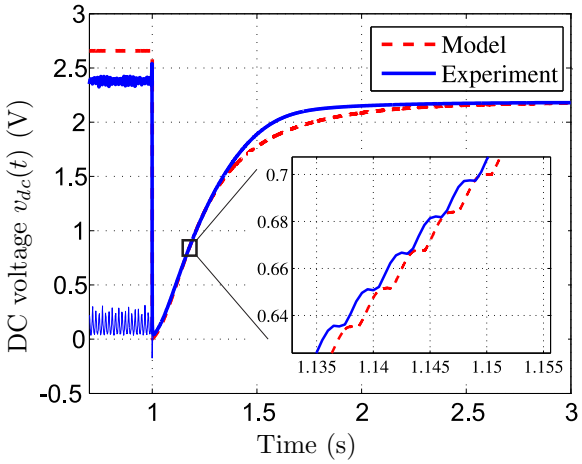

Figure 6.12: Validation results for the DC output voltage time waveform. Before 1s the plot shows the envelopes of the sinusoidal waveforms. Base acceleration is 0.2613 g at 171.3 Hz.

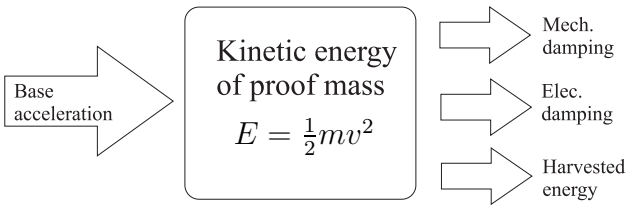

Figure 6.13: Energy flow of the energy harvesting system. Here the harvested energy is the energy stored in the load capacitor.

capacitor around this voltage by a hysteresis loop can significantly improve power extraction.

For the validation results, there are obvious discrepancies between the model and experiment. One of them is the small phase shift found in the zoom-in views, which is caused by the small mismatch of resonant frequencies (less than 0.4 Hz) between the model and the experiment. The other obvious discrepancy is during the period C, when the capacitor is charging. It is deduced that the total damping predicted by the model does not completely match that of the actual system. The validation from the modulus matching circuit demonstrated the model's ability to predict the electrical damping with the change of the output voltage. This makes the mechanical damping a potential source of mismatch. Figure 6.14 confirms that the mechanical damping in the model is close to the actual mechanical damping of the PZT beam for the base acceleration of 0.2613 g. This is because mechanical damping ratio can be estimated as the ratio of the FWHM to the natural frequency. However, the bending frequency response of the measured velocity suggests that the non-linearity of the PZT start to take effect. As elaborated by

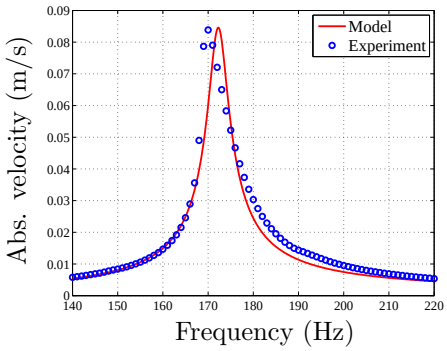

Figure 6.14: Relative velocity of the PZT beam in short circuit condition. Base acceleration is 0.2613 g at 171.3 Hz.

Wolf and Gottlieb [79], the amplitude bending to the left is a non-linear softening behaviours. While the mechanical damping used by the model is constant, it is believed that the *actual* mechanical damping is changing due to the change of velocity. As the velocity decreases, the system becomes less non-linear and hence the mechanical damping decreases. That explains why the measured velocity in period C in Figure 6.11 is higher than expected. Subsequently, this hypothesis is confirmed by experiments, from which the results are shown in Figure 6.15. Although the experiments were carried out on a PZT beam with a different length

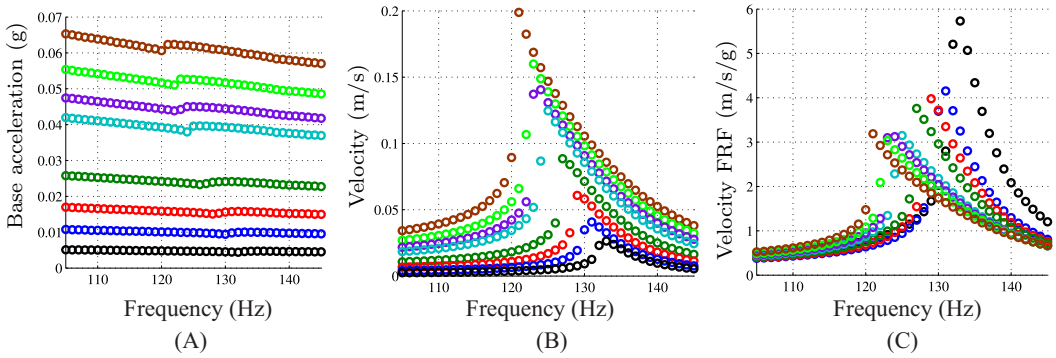

Figure 6.15: Measured velocities for a PZT beam in short circuit. As the base acceleration increases, velocity increases but velocity per g decreases. (A) indicates different level of base acceleration. (B) shows the velocity response for the corresponding base acceleration in (A). (C) shows the FRF velocity response for the corresponding base acceleration in (A). [color only]

($L_b = 23$ mm), it is evident that when the base acceleration increases, the velocity of the proof mass increases, but the velocity FRF actually decreases. This is an indication that the mechanical damping indeed increases as the PZT beam become more non-linear. If the PZT beam is excited in its linear region, the model's accuracy should be improved. Overall speaking, the validation results presented

in Figures 6.11 and 6.12 are satisfactory. Lastly, by comparing Figures 6.15 and 6.11, the electrical damping has caused the velocity to reduce from 0.8 m/s to 0.3 m/s. This implies the electrical damping has a huge influence to the dynamic of the system. It reconfirms that electrical tuning, which is a way to manipulate the electrical damping, is an effective means to shift the resonant frequency of the system.

6.4 A Proposed Impedance Matched System

6.4.1 Ideal inductor

Compared to modulus matching, the frequency range can be further increased by conjugately matching the load and the source impedance. Cammarano et al. [80] has demonstrated a wide tuning range by conjugate matching on an electromagnetic energy harvester. This case study shows that a significant tuning range can also be achieved by conjugate matching on a piezoelectric energy harvester even with non-ideal components. As being deduced in Figure 4.12, outside the open and short circuit resonant frequencies, the piezoelectric harvester behaves like a capacitive power source. Hence the most direct approach to implement conjugate matching is to connect an variable inductor in parallel or series with a variable resistor (acts as the load that absorbs power). However, the model predicts that the inductance required for either of these configurations is prohibitively large. Fortunately, the required inductance can be significantly reduced if additional capacitors are connected to the piezoelectric beam in parallel based on the relationship $L_{total} = \frac{1}{C_L(\omega)\omega^2}$, where L_{total} includes the PZT equivalent inductance and the added inductance. Furthermore, it is more practical to have a fixed inductance and a variable capacitance and resistance for frequency tuning. As a result, a passive tuning concept showing in Figure 6.16 is conceived. For the first approach to

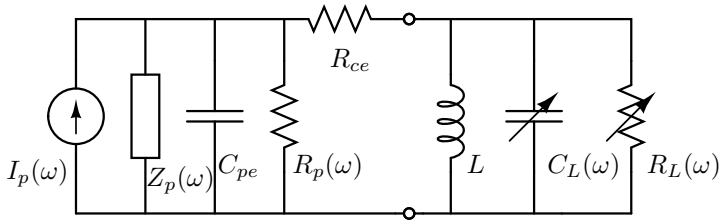

Figure 6.16: Proposed conjugate matching circuit, a fixed value inductor and a variable capacitor and resistor that change with excitation frequency. L is chosen to be 200 mH. R_{ce} is calculated to be 0.177 Ω.

evaluate this concept, the inductor L is assumed to be ideal. The analysis for an non-ideal inductor is carried out in the next subsection. In practice, the variable

capacitor $C_L(\omega)$ can be implemented by a parallel array of capacitors and MOSFETs. Different combinations of capacitors can be switched on or off to obtain a range of capacitance. Since the circuit only consumes power at the moment when the capacitance is changing, the frequency tuning mechanism is semi-active.

To better understand the dynamic of this resonance tuning concept, a case study that is based on the same mechanical set-up as in Section 6.3.2 is carried out, the numerical values for the mechanical set-up can be found in Table B.5. In the presented analysis, the value of the inductance does not affect power output and bandwidth as long as the impedance of the system is matched. Therefore, an optimal inductance value does not exist. The inductance value only affects the required capacitance. L = 200 mH is chosen because the required capacitance values are easily available. In this set-up the electrical load is

$$Z_L = \frac{1}{\frac{1}{Lj\omega} + C_L(\omega)j\omega + \frac{1}{R_L(\omega)}}. \tag{6.19}$$

The optimal $C_L(\omega)$ and $R_L(\omega)$ can be determined by equating the load impedance (6.19) to the conjugate of the source impedance (6.13). By substituting (6.19) into (6.11), the power absorbed by the load $R_L(\omega)$ is obtained, which is shown in plot 3 of Figure 6.17. In the same figure, it also shows the power output from

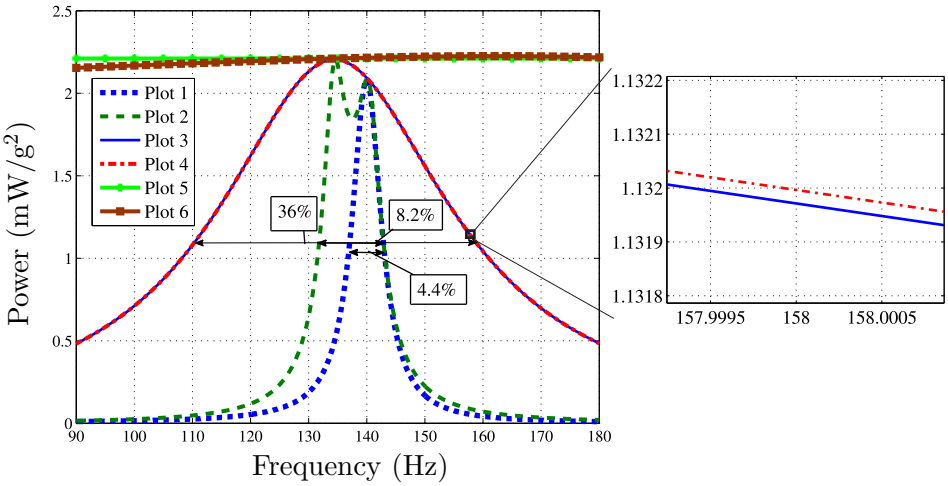

Figure 6.17: Frequency range comparison for different electrical loads. Plot 1: Fixed value optimal resistive load. Plot 2: Modulus matched load. Plots 1 and 2 are experimentally validated in Figure 6.8. Plot 3: Conjugate matched load. Plots 1 - 3 include both $R_p(\omega)$ and R_{ce} losses. Plot 4: Conjugate matched load only includes $R_p(\omega)$. Plot 5: Conjugate matched load including first 3 modes of vibration, $R_p(\omega) = R_{ce} = 0$. Plot 6: Conjugate matched load including only the first mode of vibration, $R_p(\omega) = R_{ce} = 0$.

the original distributed parameter model and other electrical load optimization techniques for frequency range comparison purposes. With the polarisation losses of the PZT material included, plot 3 shows a power reduction as the excitation

frequency drifts away from resonance. Despite the losses, the conjugate matched system can potentially give a 36 % frequency range that is more than 4x of the modulus matched system and 8x of the system with a fixed optimal load. The range of frequency response is defined as the full width at half maximum (FWHM) divided by the central frequency, where FWHM is the frequency range at which the power is above half of its maximum. A zoom-in view of Plot 4 suggested that the ohmic losses of the PZT only account for less than 0.1 % of the total losses, whereas the polarisation losses are responsible for the rest at 158 Hz. These losses are caused by a substantial voltage being generated across the PZT beam at that frequency. Plots 5 and 6 show the results obtained from the original model derived in Section 4.3. In plot 5, the inclusion of higher vibration modes shows both a constructive and destructive manner to the final power output. This is due to the superposition of the output voltage on each mode. By only taking the fundamental vibration mode, a flat line of plot 6 is obtained, which suggests a lossless system that gives maximum power output at all frequencies. Apparently, neither of plots 5 and 6 are realistic. The comparison demonstrates the importance of including the polarisation losses for a conjugate matched system.

For the chosen inductor, the required capacitance and resistance to keep the system in tune is shown in Figure 6.18. The FWHM frequency range that is aimed to

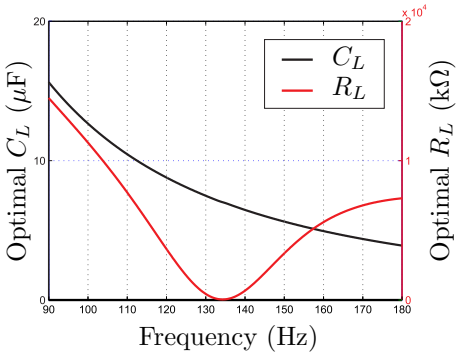

Figure 6.18: The required capacitance and resistance to tune to a conjugate matched system for L = 200 mH.

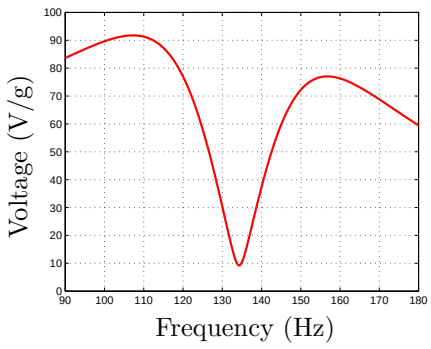

Figure 6.19: Frequency response function of voltage output.

achieve corresponds to 110 and 160 Hz. This translates to a capacitance range from 5 to 11 μF, which is very common in electronic components. It is estimated that the required load resistance is between 40 Ω to 8 MΩ. Figure 6.19 predicts the output voltage for the frequency range, which provides information about the requirement for voltage rating of the electrical components. The voltage graph also gives insight of where the energy goes as the harvester is kept in tune over the frequency range. When the harvester is shaken near its natural frequency, the voltage is low as it requires very little energy to keep the PZT beam in tune. As the excitation frequency deviates to either sides of the natural frequency, higher

voltage is needed to keep the PZT beam in tune as more energy is needed to circulate through the PZT to give enough influence. When the excitation frequency is further away from the natural frequency (at lower than 105 Hz or more than 155 Hz in Figure 6.19), more than half of the energy is lost through the polarisation losses R_p leading the voltage to decrease.

6.4.2 Non-ideal inductor

While the study of a conjugate matched system with an ideal inductor is very optimistic, further study reveals that the real challenge of this electrical tuning concept lies in the inductor. Although assuming an ideal inductor is appropriate for the analysis of many electrical circuits, it is certainly not the case for this proposed concept. This is because the energy (or power) available to the circuit is very little, and losses are further elevated in a high voltage high current condition as the circuit is tuned to resonance. These two reasons suggest the consideration of the inductor losses is absolutely vital for the assessment of the electrical tuning concept. The major losses associated with an inductor are the winding losses and the core losses. The former are traditionally modelled as a series resistor and the latter a parallel resistor. Normally the winding losses dominate at low frequencies and the core losses dominate at high frequencies. For convenience, the total losses are implemented by an equivalent series resistor R_{esr} in the subsequent analysis. The circuit that includes the inductor losses is shown in Figure 6.20. In this

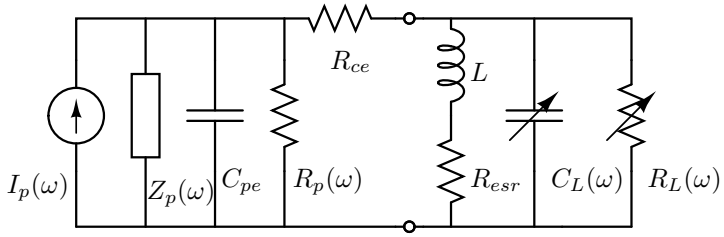

Figure 6.20: Proposed conjugate matching circuit, a fixed value *non-ideal* inductor and a variable capacitor and resistor that change with excitation frequency.

scenario, the total load impedance becomes

$$Z_L = \frac{1}{\frac{1}{Lj\omega + R_{esr}} + C_L(\omega)j\omega + \frac{1}{R_L(\omega)}}. \tag{6.20}$$

Following the same procedure as previously mentioned, the optimal $C_L(\omega)$ and $R_L(\omega)$ can be determined by equating the load impedance (6.20) to the conjugate of the source impedance (6.13). The power absorbed by the load $R_L(\omega)$ is determined by substituting (6.20) into (6.11). Figure 6.21 shows how the ESR losses

of the electrical circuit affect the tuning range of the power output. With the inductor losses considered, the frequency range of the power output is reduced. The simulation sheds light on the fact that it is not the absolute value of the R_{esr} but the ratio of R_{esr} to L that influences the tuning range. The first three plots from

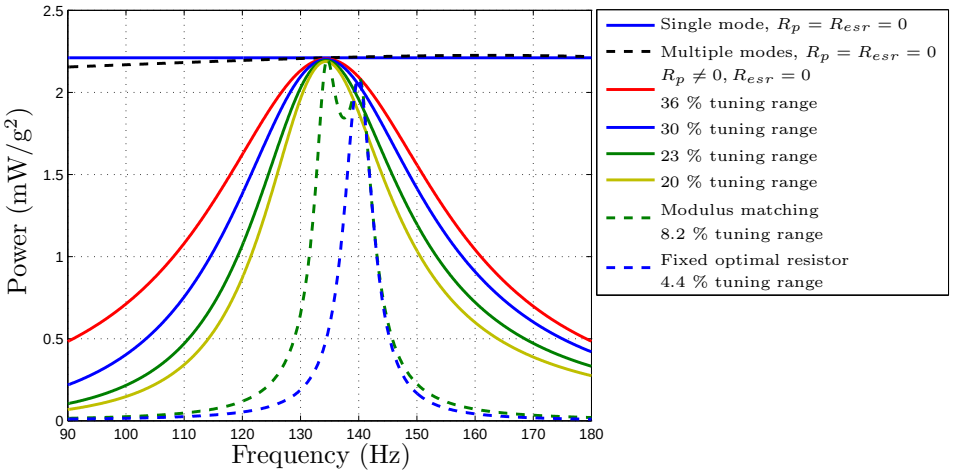

Figure 6.21: Inductor ESR in a conjugate matched system influences frequency tuning range.

the top of Figure 6.21 and the plots for modulus matching and a fixed optimal resistance load were discussed in the previous subsection. The highlights of Figure 6.21 are the three plots that represents the three tuning ranges: 30 %, 23 % and 20 %, they are obtained by increasing the R_{esr} of the inductor while holding L constant. In other words, the tuning range keeps decreasing as R_{esr}/L increases, and it will eventually reach a point where a conjugate matched system does not bring any benefit in frequency range compared to a modulus matching system or even a system with a fixed optimal resistive load.

For each tuning range, the corresponding capacitance and load resistance with respect to the excitation frequency are shown in Figure 6.22. The axis on the left is the capacitance value, and it can be seen that the required capacitance is identical to the system with an ideal inductor. The axis on the right is the resistance value. The plots show that the required optimal load resistance required for conjugate matching decreases as the tuning range decreases. Figure 6.23 indicates the higher the resultant tuning range, the higher the output voltage. Again, the information gives the voltage rating requirement for the electrical components. To maintain the same frequency range on power output, higher inductance value allows more ESR. The ESR versus inductance value for the corresponding frequency range is given in Figure 6.24, which clearly shows the relationship among the inductor, the ESR and the resulting tuning range. The curve in red is the ideal inductor, which gives a 36 % tuning range, as the ESR with respect to the inductance increases,

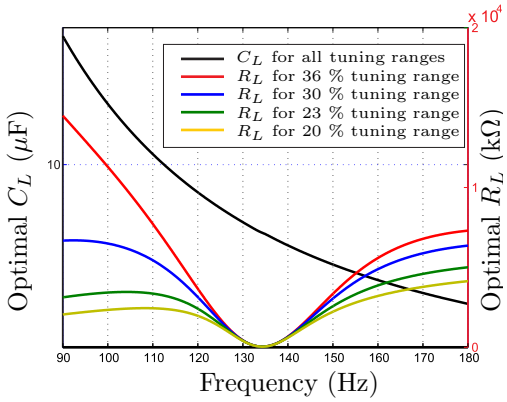

Figure 6.22: Required capacitances and resistances for conjugate matching.

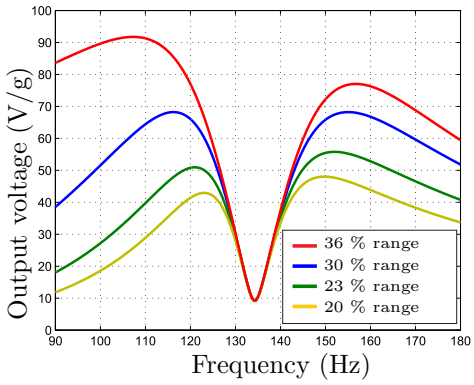

Figure 6.23: Frequency response function FRF of output voltage.

the tuning range decreases. The curve in black represents a typical profile of the inductance and the winding ESR of a ferrite toroid core inductor, when the number of turns increases. Since the natural frequency of the system in simulation is relatively low (140 Hz), only the winding resistance losses are considered. Overlapping these curves results in intriguing findings. It can be seen that it is very difficult to achieve conjugate matching if a low inductance is used, because the required ESR is impractically small. As the inductance increases, the allowable ESR increases much faster than the increase of ESR due to the addition of more windings in the inductor. In the other words, conjugate matching is more practical to be implemented by an inductor that has a very high inductance value but a very low ESR to inductance ratio. This translates to an inductor whose core has high permeability and low core losses, and has many number of turns with relatively large wire diameter. Due to the difficulty in obtaining an inductor with the required specifications, the simulation results cannot be validated by experiments. Nonetheless, a procedure for the design of a conjugate matching system is developed. For any PZT harvester, the simulation predicts the frequency tuning range of power output, and the required specifications of the electrical components. The model suggests that with commonly available PZT material and inductors today, conjugate matching can only be implemented in a low mass, medium frequency and very low power output PZT harvester. When the frequency is too low, the required inductance to ESR ratio is too high. When the frequency is too high, although the inductance to ESR ratio is greatly reduced, the ESR of the inductor core losses can be unacceptably high. The hurdles of implementing a practical conjugate matching system lie in the limitations on currently available PZT materials and inductors. The losses due to the PZT material (loss tangent) is the single largest hit, followed by the losses of the inductor. However, the incremental advances in PZT material and inductor technologies will make this conjugate matching concept much more achievable for high power and low frequency harvesters.

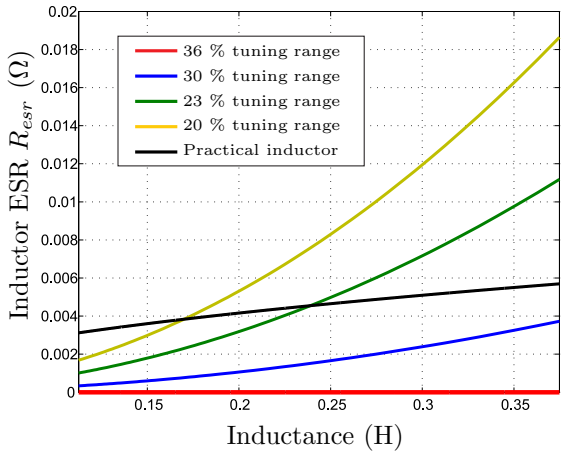

Figure 6.24: Inductor requirements for each frequency tuning range. The practical inductor is 3C90 ferrite toroid core from Ferroxcube.

6.5 Conclusions

This chapter presents an improved continuum model for PZT cantilever beams. The model takes into account of polarisation losses and electrode layer ohmic losses. The inclusion of these losses is essential for a conjugate matched system where relatively high voltage and current are circulating among passive elements in the circuit. The model is experimentally validated on a modulus matched circuit, and on a circuit of a bridge rectifier with a capacitive load. It has demonstrated that, compared to the original model, the improved model produced a more accurate results at the frequency region where the voltage of the PZT is high. A 8.2 % frequency tuning range was obtained from the experiments on modulus matching. The experimental validation on a full bridge rectifier with a capacitive load demonstrates that the improved model can simulate a PZT beam with any electrical load (linear/non-linear and of any impedance). All experimental observations quantitatively agree well with the model.

The study has shown that electrical tuning is only effective for small frequency range. Even with this limitation, the advantages of an electrically tuning system renders it an attractive solution for small frequency range harvesters or for fine tuning purposes to complement a mechanical tuning system. To maximise the tuning range, a concept for a conjugate matched system is proposed. The circuit consists of a fixed value inductor and a variable capacitor and a load resistor. The case study reveals that the contact losses for the particular PZT beam are negligible while the polarisation losses account for most of the losses in the conjugate matched system. With polarisation losses considered, the theoretical maximum frequency range can be achieved by a conjugate matched system is 36 %, but the range dimin-

ishes as the inductor ESR losses increased. It is found that it is not the absolute value of the R_{esr} but the ratio of R_{esr} to L that influences the tuning range. This means conjugate matching is more practical to be implemented by an inductor that has a very high inductance value but a very low ESR to inductance ratio. In the presented analysis, a procedure is developed to deduce the requirements of the inductor and the required capacitance and resistance values. The simulation results suggest that with commonly available PZT material and inductors today, conjugate matching can only be implemented for a small mass, medium frequency and very low power output PZT harvester. The challenges are the loss tangent of the PZT material and the ESR to inductance ratio of inductors. Nonetheless, as material science and manufacturing technologies incrementally improved, the concept presented in this chapter for conjugate matching will eventually become more achievable for high power and low frequency harvesters.

7

Resonance Tuning by Mechanical Actuation

7.1 Introduction

Applying mechanical actuation is perhaps the most direct approach towards resonance tuning of a harvester. Compared to electrical tuning, a much wider frequency range is more achievable by mechanical tuning. In the simplest form of a piezoelectric energy harvester consisting of a cantilever beam and a tip mass, conceptually there are several ways to shift the fundamental frequency of such a structure. These include but not limit to changing the position of the mass relative to the beam, changing the weight of the tip mass, changing the effective length of the beam and applying variable forces to modify the overall stiffness of the structure. While none of these concepts seem to end up with a simple harvester design in practice, the additional complexities should be justified by the *continuous* tuning range and efficacy for operating in the real world environment. In this chapter, several concepts on adjusting the resonant frequency mechanically are presented and their merits and potential issues are discussed. Compared to multi-modal and electrical tuning, mechanical tuning introduces relative movements between parts hence it is more vulnerable to mechanical damping. If not properly designed, the relative movements can dramatically increase the mechanical damping and decrease power output. In such a case, even an extremely wide tuning range would lose its significance. Therefore, to assess the concepts, emphasis is given to the potential mechanical damping. In addition, emphasis is also given to practicality and how well it will work in a typical machine condition monitoring environment. While the presented concepts are all applicable to adaptive tuning mechanism, a semi-active tuning mechanism can be implemented by using an electric motor for actuation, which is controlled by intelligent circuitry with sensor feedback. In particular, two novel concepts are proposed. Based on which detail design and prototypes are produced and performance evaluated. The testing results shed light

on the effectiveness of the concept and possible improvements if they were to be developed into commercial products.

This chapter is organised as follows. In Section 7.2, a few concepts for mechanical resonant tuning at the basic level are discussed. In Section 7.4, a concept is proposed to tune the frequency by changing the pivot point(s) between the proof mass and the beam. Two prototypes were built and tested, and possible improvements were suggested. In Section 7.5, a concept is proposed to tune the frequency by changing the overall stiffness, and two prototypes were built and tested, and possible improvements were suggested. Conclusions are given in Section 7.6.

7.2 Preliminary Concepts

7.2.1 Mass shifting

For a piezoelectric energy harvester, as the mass is shifted relative to the beam, the effective beam length is changed and therefore the resonant frequency of the structure is adjusted. As illustrated in Figure 7.1 (A), mass shifting can be achieved by mounting rollers on two piezoelectric cantilever beams, and the mass is shifted along the rollers between the two beams. For this concept to work satisfactorily,

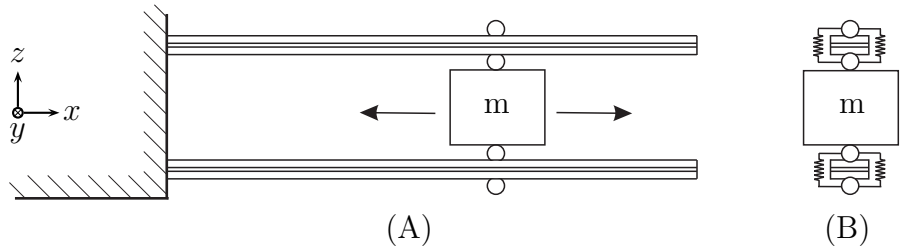

Figure 7.1: Preliminary concept: resonance tuning by mass shifting. (A) Side view. (B) Front view, springs are in tension.

the coupling between the beams and the mass is critical. While the harvester is experiencing vertical vibrations, ideally, there should be no relative movement between the mass and the beams in *all* 3 axes for minimum mechanical damping operation. As illustrated in Figure 7.1 (B), this can be achieved by holding each of the roller with two tension springs to constrain the vertical movement (z-axis), and having a grove on the beam to constrain the lateral movement (y-axis). To constrain the longitudinal movement (x-axis), the correct materials are chosen to obtain a high friction between the roller and the beam's surfaces, and the gearbox that the motor drives the rollers must have relatively high gear ratio. With these conditions met, when the motor is not activated, the relative longitudinal movement between the mass and the beams are restricted. The high friction

between the roller and the beam's surfaces also help eliminate slipping when the rollers are being driven, which reduces power consumption of the motor.

7.2.2 Length varying

Instead of shifting the mass at the free end of the beam(s) as mentioned in the previous sub-section, the effective length can also be altered by shifting the clamping position of the fixed end. The concept for such a mechanism is illustrated in Figure 7.2. Based on a piezoelectric cantilever beam where the tip mass is mounted at

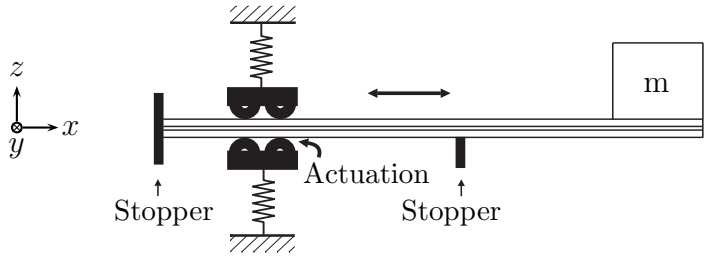

Figure 7.2: Length shifting: use a roller to shift the effective length of a cantilever beam with spring loaded guiders.

the free end, four rollers are used to create the boundary at the fixed end of the beam, and at least one of the rollers is driven by an electrical motor to adjust the effective beam length for frequency tuning. To minimise mechanical damping, it is imperative that the rollers are spring loaded against the beam. Since the springs are the connection between the beam and the base, they should have a relatively high spring constant to minimise losses of vibrations conveyed from the base to the cantilever. In other words, the resonant frequency of the springs should be much higher than that of the vibration to be harvested. However, if the spring constant is excessively high, more power input to the electrical motor is required to overcome the friction between the rollers and the beam. Trade-offs like this will need to be determined in the design phrase. Further more, mechanisms should be in place to constrain the beam movement relative to the rollers in the x and y axes. From the practicality point of view, the potential issue of this concept is compactness. The current presentation of the concept is not the best way to utilise space because the width of the housing needs to be twice of the length of the beam. A radical design is necessary if this concept is chosen for product development.

7.2.3 Mass transfer

It is well known that the stiffness of a cantilever structure depends upon the weight of the end mass. The heavier the mass, the lower the frequency and vice

versa. Based on this principle, a couple of concepts for mass transfer is conceived. Showing in Figure 7.3 (A) is a concept that achieves mass transfer by a hydraulics mechanism, in which the weight of the liquid serves as the proof mass. For a

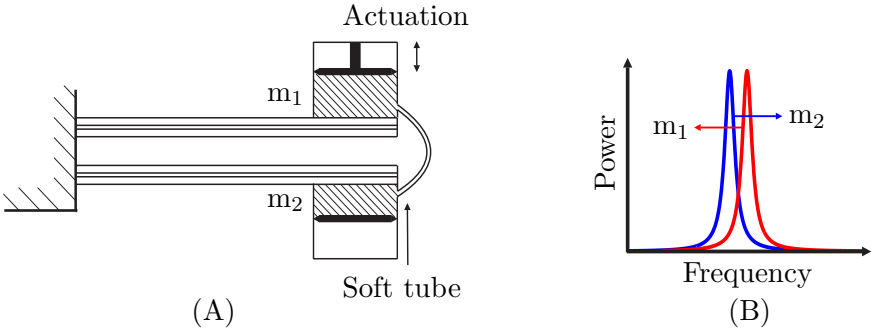

Figure 7.3: Preliminary concept: mass transfer by pumping. (A) Mass can be either liquid and/or micro-metal beads. (B) Slight overlapped in the frequency response of the two masses, as the mass is transferred, the two frequencies shift away from each other.

mass transfer mechanism as such, there must be at least two reservoirs where the exchange of mass takes place. Instead of putting one of the reservoirs on the fixed base that contributes neither power output nor tuning range, a second cantilever beam is added and both reservoirs are functioned as proof mass for each of the beams. In this arrangement, the tuning range can be extended even though there may be only one of the two beams at resonance for a given excitation frequency. The linkage between the two reservoirs should be a soft tube or a coil tube that isolates the dynamics of the two beams as much as possible. It should be noted that for a maximum tuning range, the stiffness of the two beams should not be identical. Figure 7.3 (B) shows the frequency response for both beams when one of the reservoir is full and the other is empty. As the piston gets actuated, the liquid is transferred from the full reservoir to the empty one, shifting the resonant frequency of both beams away from each other. The presented hydraulics mechanism will work regardless of the orientation of the device relative to gravity. The biggest advantage of this concept is that it completely eliminates the moving parts between the proof mass and the beam. As a result, wear and tear is greatly reduced and very low mechanical damping can be achieved. The only additional source of mechanical damping is the soft tube, which can be easily managed by proper design.

However, the biggest challenge for this concept is the density of the proof mass. For applications where small form factor is not required, such as sensors that harvest ocean wave energy, the nearby water can be used as the mass. Whereas for machine condition monitoring applications where a small form factor is an important feature, using water as the mass will not be effective due to two reasons: 1) power is proportional to proof mass; and 2) The higher the density, the larger the tuning range. Water is simply not dense enough to meet both the power requirement and the tuning range in a compact size of an industrial sensor. In fact,

the densities of most liquids are too low to make this concept effective. With one exception is mercury, which is over 13× heavier than water. Unfortunately mercury is poisonous in both liquid and vapour forms, and many countries have banned products that contain mercury. Ideally, the liquid should be some compound that is very dense and harmless to people and the environment. An example is a mixture of tungsten micro beads and liquid (e.g. oil) that form a mud type of fluid. Tungsten is the heaviest metal with density of 19.25 kg/m^3. The grain of the beads must be fine enough to allow free flow of the mixture through the tube(s).

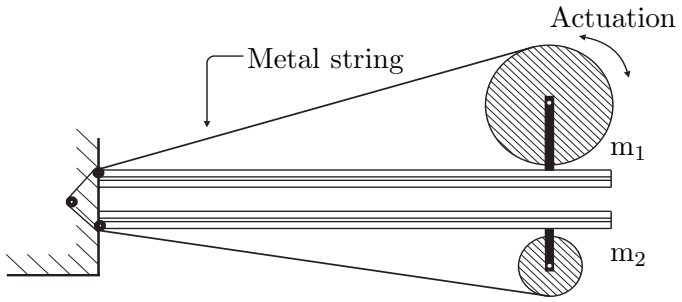

Figure 7.4: Mass transfer by winding: the mass on the cantilever beam can be transferred by winding a metal chain.

As illustrated in Figure 7.4, the second concept for mass transfer is by winding a metal string between two reels that serve as the mass reservoir of each cantilever beams. For the very same reason, using two piezoelectric beams would extend the tuning range of the harvester. The primary proof mass is the string, hence, a dense material such as metal would give a wider tuning range and a higher power output. The string is in tension and is anchored on the fixed ends of the beams to minimise the influence on the beam vibration. The tension of the string has to be set judicially or it can dramatically increase the stiffness of the two beams. The advantage of this concept is that does not use liquid or mud medium as proof mass, which reduces the implementation complexity. Moreover, the concept is more compatible with miniature motors instead of linear actuators. In terms of cost, performance and power efficiency, miniature motors are generally more superior than their linear actuator counterparts.

7.3 Schemes for Evaluating Concepts and Prototypes

In order to design an effective semi-active tuning mechanism, the structure should not be constrained by cantilever beams. An ideal mechanism should have very

low mechanical damping ratio and a wide tuning range in relative terms (i.e. in percentage of the central frequency), and the proof mass can be scaled up if required and no power should be consumed to maintain the tuned frequency when the mechanism is not activated. In addition, from a commercial viewpoint, compactness is also an important consideration. For concepts of very different structures, so many parameters come into play, such as proof mass and thickness of piezoelectric layers. As a result, comparing the effectiveness among them can be very difficult. Merely comparing power output is not sufficient because for the same concept the power can be increased by mounting a bigger proof mass on a stiffer piezoelectric beam to maintain the same frequency. Imposing the same proof mass to all the prototypes is unrealistic because the resonant frequencies of the resulting prototype may be in a very different range based on the nature of the design. Despite the various frequency range, proof mass among prototypes, the scheme to compare them is mainly based on mechanical damping. Having a low mechanical damping ratio is particularly critical because it directly dictates power output at resonance. A 10 % reduction on mechanical damping means a 10 % gain in power output or a 10 % reduction on the required proof mass. Either way, mechanical damping is one of the key factors that determine the performance of a semi-active tuning harvester. From the basic mass spring damper model derived in Section 3.2, the general expression for the relative velocity FRF (velocity *per* acceleration) can be written as (c.f. 3.3)

$$\Big|\frac{\dot{Z}(\omega)}{A_0}\Big| = \Big|\frac{\omega}{-\omega^2 + 2\xi_m\omega_n\omega j + \omega_n^2}\Big|, \tag{7.1}$$

where $A_0 = Y_0(j\omega)^2$. To measure the relative velocity FRF due to mechanical damping alone, the electrical damping can be eliminated by shorting the piezoelectric layers. From equation (7.1) it should be noted that, for the same resonant frequency, the higher the relative velocity FRF, the lower the damping. This relationship holds regardless of the size of the proof mass and the thickness of the piezoelectric layers. Therefore, the relative velocity FRF is a good indicator of mechanical damping ratio and should be used to compare different prototypes for the corresponding frequencies. Another aspect to compare is the tuning range in *relative terms*, that is the percentage of the central frequency. For a harvester whose frequency limits are F_H and F_L, the tuning range is defined as

$$F_{range} = 2\frac{F_H - F_L}{F_H + F_L}. \tag{7.2}$$

Therefore, an infinite tuning range corresponds to $F_{range} = 1$. Comparison of relative term removes the bias for energy harvesters that are designed for a different frequency range. To evaluate the concept, not only the measured tuning range, but also the requirements to extend the tuning ranging should be taken into consideration. The reason is that the tuning range is more scalable in some concepts than the others, which is an important consideration.

7.4 Concept on Varying Length

With an overview of options available for mechanical tuning, some concepts are selected and refined. As a result, a novel concept that is a hybrid of mass shifting and length varying is proposed. Figure 7.5 is a simplified illustration of the concept, where it is assumed that the pivot roller rigidly couples the proof mass and the beam, and it can be shifted from L_1 to L_2. This hybrid concept overcomes

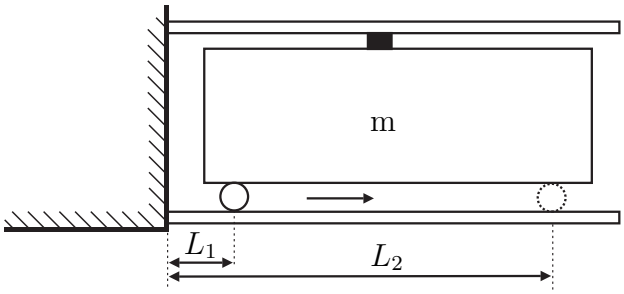

Figure 7.5: The frequency tuning range of concept A depends on the ratio of L_1 and L_2.

the drawbacks of the two individual concepts: for mass shifting, it requires a lot of energy to shift the heavy mass, and for length varying, it requires a lot of space to allow the beam to be shifted. The upper beam is to anchor the proof mass, and the lower beam is to function as a spring with variable spring constant, depending on the position of the pivot point. The tuning mechanism of the concept is achieved by adjusting the pivot point between the mass and the lower bender. For a fully functional version, piezoelectric layers can be placed on both of the benders. The biggest advantage of the concept is to allow all the mechanical and electrical components to be embedded to the proof mass, maximising space usage. As a result, other than the two benders and the housing, all parts are utilised as the proof mass. Sliding the pivot along instead of the more intuitive way of moving the proof mass minimises the size and range of the moving parts, hence reduces power consumption. To maximise the frequency tuning range, the spring constant of the lower beam should be much larger than that of the upper beam. If the spring constant of the upper beam is assumed to be zero and the cross section of the lower beam to be constant with respect to the length of the beam, the frequency can be estimated by the lumped mass model $\omega = \frac{3YI}{mL^3}$. According to the definition in (7.2), the frequency range of this concept can be simplified to

$$F_{range} = 2\frac{1 - \sqrt{(\frac{L_1}{L_2})^3}}{1 + \sqrt{(\frac{L_1}{L_2})^3}}. \tag{7.3}$$

The expression (7.3) gives an indication of how the L_1 to L_2 ratio relates to the frequency range. To minimise mechanical damping, great attention must be paid to the coupling of the roller to the mass and the beam in the design process.

7.4.1 Prototype A1 design

As the first investigation of concept A, the basic design shown in Figure 7.6 is proposed. It consists of two cantilever steel benders and an iron mass block with a

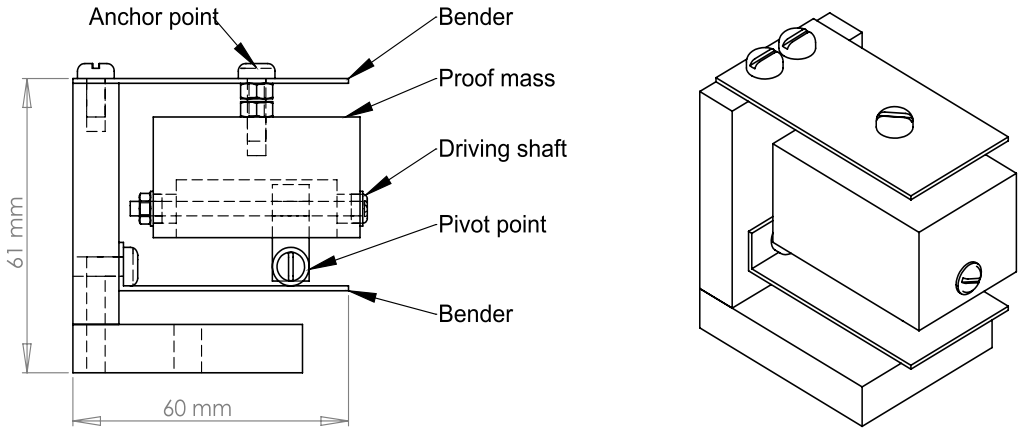

Figure 7.6: 3D model of prototype A1.

threaded shaft that drives a roller pivot. The pivot roller is driven by a threaded shaft rotating in the proof mass, which can be driven by an electric motor for semi-active tuning. The vertical coupling of the mass and the benders is achieved by pre-loading the two benders towards the mass. Flanged bearings are fitted to both end of the shaft to minimise friction for tuning. However, the frequency is tuned by rotating the shaft manually. The prototype does not include the piezoelectric layers and the electrical motor. Even without these elements, the prototype embodies the main characteristics of the concept, and is sufficient to demonstrate the tunability of the mechanism.

7.4.2 Prototype A1 testing

Experiment is carried out to evaluated the performance of the prototype. The experiment set-up includes an electromagnetic shaker that provides the base vibration, an accelerometer beneath of the prototype that measures input accelerations, and a laser vibrometer that measures the dynamic response of the upper bender. A total of five trails were conducted in the experiment. In each trail the pivot point was shifted to four positions that included the limits of the travelling range. For each position the velocity of the upper bender was measured. The snap shots of the prototype in various pivot positions are shown in Figure 7.7. The upper and lower bender are made of stainless steel and the proof mass is mild steel with a dimension of 25 mm $\times$ 30 mm $\times$ 45 mm. The velocity amplitude and tuning

Figure 7.7: Prototype A1 was manufactured and tested on the shaker.

range of the five trials are very consistent , and one of the results are shown in Figure 7.8, where the circles are the actual recorded points. It is evident that the resonant frequency is shifted from 64 to 92 Hz as the pivot was shifted from the free end to the fixed end of the bender. Without any optimisation of tuning range

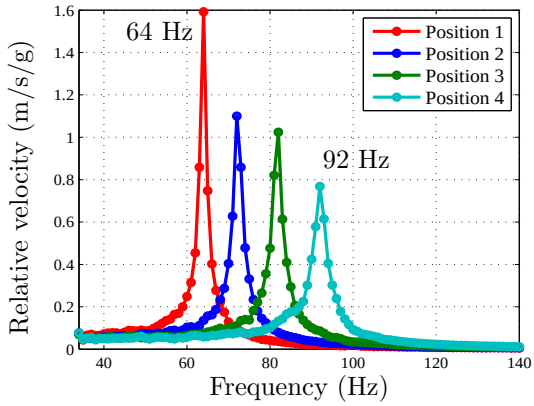

Figure 7.8: Measured relative velocity FRF of prototype A1. Position 1 is when the moveable pivot is closest to the free end. Position 4 is when the moveable pivot is closest to the fixed end. Tuning range is from 64 to 92 Hz, or 78 Hz ±18 %.

considered in the design of the prototype, the variance in frequency obtained is 28 Hz, or 36 % of the central frequency. This confirms that the proposed concept is effective for wide tuning range. A wider tuning range can be simply achieved by extending the length of the benders. The mechanical damping for the resonant peaks are estimated in Table 7.1. As suggested by Roundy [14], the mechanical damping of a 1 cm^3 piezoelectric cantilever is normally between 0.01 to 0.02. Using this as a reference, the damping of the prototype for its frequency range is considered very low. It was found that the vertical coupling of the pivot to the lower bender is critical to the proper functioning of the whole device. To simplify

Table 7.1: Mechanical damping ratio of prototype A1.

Frequency (Hz)	Mech. damping ratio ξ_m
64	0.0077
72	0.0096
82	0.0093
92	0.0108

the construction, the pivot of the prototype was relied on pre-load tension of the benders to provide the vertical coupling force. While the pre-load tension was adequate for prototyping, it is not reliable in practice. This is because the tension force varied noticeably when the pivot point slides along the bender in the aim to change the spring constant. The tension force also adds considerable friction on the pivot in the longitudinally direction, making it more energy consuming to slide along. Hence an alternative mechanism that keeps the pivot point and the bender securely coupled under vibration will make the device much more robust. This can be achieved by having two rollers clamping the lower bender to provide a very secure coupling force vertically while keeping the pivot free from sliding longitudinally when they are driven by the motor. The other place for improvement is that, as the pivot point gets shifted, the proof mass is anchored in an asymmetric manner. As a result, the proof mass is vulnerable to wobbling or rocking motion when subject to vertical vibration. This is undesirable because it creates rubbing motion between the pivot point and the lower bender, which can increase damping.

7.4.3 Prototype A2 design

With the lessons learned from prototype A1, a design of a second version of the prototype is produced, whose Solidworks model is shown in Figure 7.9. The overall dimensions of length, height and width are 95mm, 100mm and 35mm, respectively. One of the major improvements of this prototype is that there are two lower benders to support the proof mass instead of one. This arrangement allows the proof mass to be mounted in a balance manner for all positions as the rollers slide along the benders, hence eliminating the rocking motion. Another major improvement is the pivot mechanism. In this prototype, the vertical coupling no longer relies on pretension of the benders. Instead, the coupling is provided by the four bearings that clamp the lower bender, whose detailed view can be seen in Figure 7.10. The two bearing on the top are radial bearings and they are vertically spring loaded. The bearings on the bottom are flanged bearings that guide the motion of the pivot along the beam. This prototype, however, is still manually operated for frequency tuning, and there is no piezoelectric material bonded on the benders. Since the primarily focus are the frequency tuning range

	Parts
1	Beam 2
2	Mass
3	Beam 1
4	Rod
5	Spring
6	Bearings

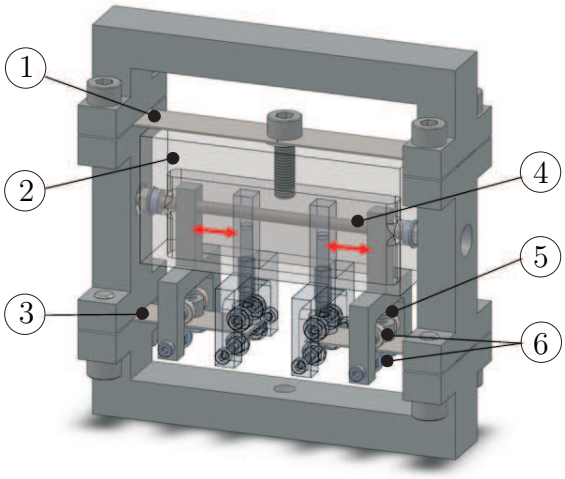

Figure 7.9: 3D Model of Prototype A2.1.

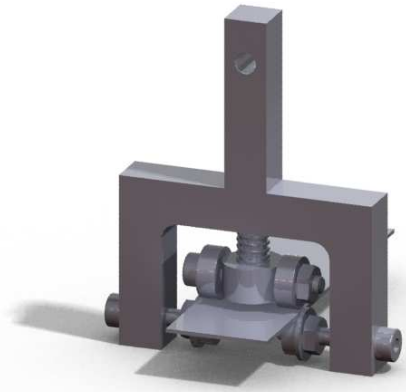

Figure 7.10: Detail view of the clamping mechanism of prototype A2.1.

and the mechanical damping, the prototype was considered sufficient for concept evaluation purposes.

A lumped-mass model is employed to estimate the frequency range of this prototype. It is assumed that the bending moment of the beam on the pivot roller is zero. In other words, the two lower benders are modelled as perfect cantilever beams with the effective length being from the fixed end to the pivot roller. The upper bender is modelled as a beam with a fixed-fixed boundary condition. Based on these assumptions, the overall stiffness is the sum of the stiffness contributed by each individual beam, and therefore the fundamental natural frequency can be calculated as [34]

$$\omega = \sqrt{\frac{\frac{192YI}{L_1^3} + 2\frac{3YI}{L_{2e}^3}}{M_t}}. \tag{7.4}$$

The detailed dimensions and material properties can be found in Table B.8 of Appendix B. Using (7.4) as an approximation, the frequency range calculated is 49.3 Hz - 108.6 Hz, or about 37 % of the central frequency.

7.4.4 Prototype A2.1 testing

Figure 7.11 shows the actual prototype A2.1 that was built. The frame and the bender clamps are made of aluminium and the proof mass and benders are made of steel. By applying the same procedure, this prototype was tested on the shaker

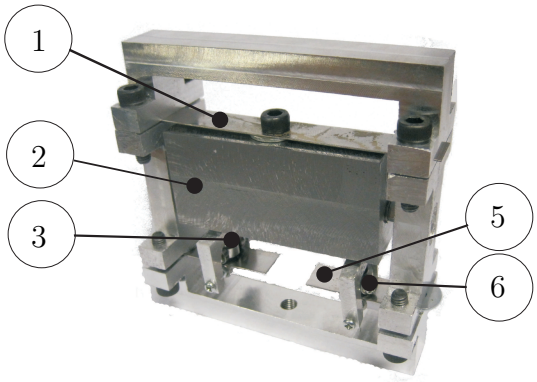

Figure 7.11: Prototype A2.1 was manufactured and assembled.

with LabVIEW™. The recorded relative velocity for different position of the rollers is shown in Figure 7.11. The results turned out that a tuning range of 49 - 67 Hz was observed, which corresponds to 55 % of the central frequency. The dependency is believed to be caused by a few factors. The assumptions made to evaluate the stiffness of the individual beam are not entirely valid. The prototype was not manufactured to the desired precision, and the rollers failed to clamp the beam tightly tight enough. Due to the limited sampling time, the exact resonant peak for position 2 - 4 is failed to be recorded. However, it shows a similar pattern to the last prototype, which is an decreasing velocity amplitudes as the frequency increases. This is expected because, according to (7.1), the velocity decreases with the increase of frequency for a constant mechanical damping ratio. With the help of the impulse response of the time waveform, the damping ratios of four different frequencies are estimated in Table 7.2. Despite the improvements, the overall mechanical damping observed in this prototype is actually worse. Two main sources of damping are identified. One is the coupling between the roller forks and the rod, and second is that the lower benders are not clamped tight enough.

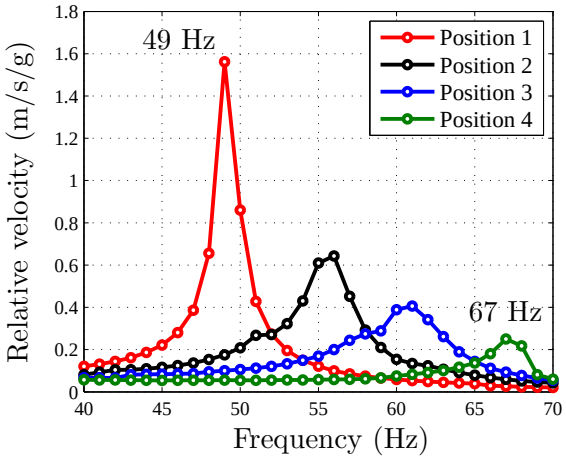

Figure 7.12: Measured relative velocity FRF of prototype A2.1. Position 1 is when the moveable pivots are closest to the free end. Position 4 is when the moveable pivots are closest to the fixed end. Tuning range is from 49 to 67 Hz, or 58 Hz ±16 %.

Table 7.2: Mechanical damping ratio of prototype A2.1.

Frequency (Hz)	Mech. damping ratio ξ_m
49	0.01
55.5	0.018
60.5	0.026
92	0.03

7.4.5 Prototype A2.2 testing

Based on the same concept, a couple of modifications have been made to the prototype, whose Solidworks model is shown in 7.13. In this version, the roller clamps have been replaced by blade clamps that are made of polyoxymethlene (POM). POM has a very low coefficient of friction with respect to metal, and the small contact area further reduces its friction. Another improvement is made to the rod in the proof mass, which is replaced by a better manufactured one. With these improvements, the same test was undertaken on the prototype, and the recorded relative velocity of the proof mass is shown in Figure 7.14. Being confirmed by the numerical results provided in Table 7.3, both the damping and the tuning range of this prototype have been improved compared to its predecessor. In particular, the prototype shows an excellent performance around the 50 Hz region, where its damping ratio is consistently below 0.01. The lowest measured damping ratio of 0.0062 at 49 Hz exceeds the expectation.

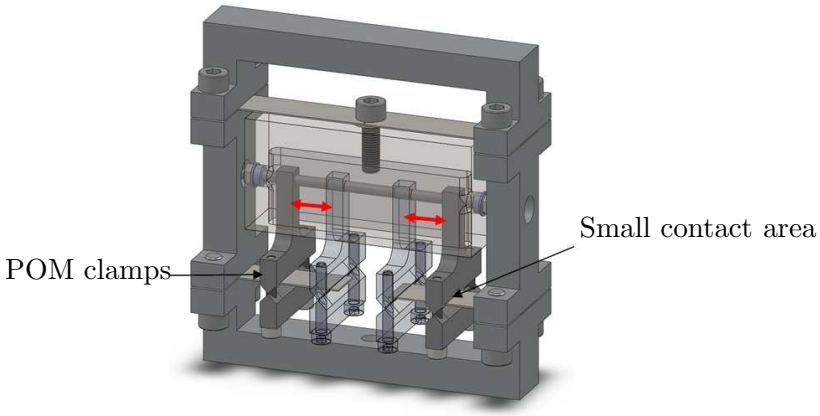

Figure 7.13: 3D model of prototype A2.2.

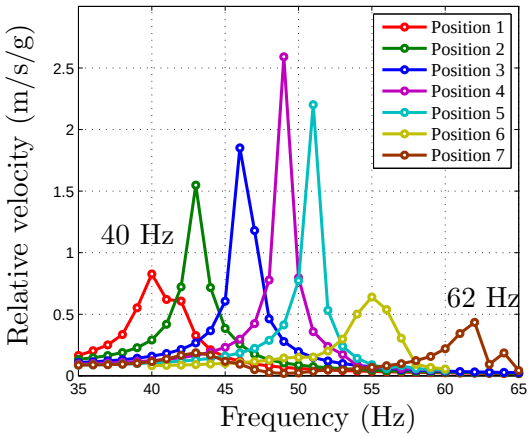

Figure 7.14: Measured relative velocity FRF of prototype A2.2. Position 1 is when the moveable pivots are closest to the free end. Position 7 is when the moveable pivots are closest to the fixed end. Tuning range is from 40 to 60 Hz, or 51 Hz ±22 %.

7.4.6 Concept A discussions and summaries

Concept A is to adjust the resonant frequency of the harvester by shifting the contact point between the cantilever beam and the proof mass. As a preliminary test, prototype A1 shows some promises on both the tuning range and mechanical damping. As a step forward to a more practical configuration, a more reliable version, prototype A2 was created, and its mechanical damping and tuning range was further improved. From the measured performance of the prototypes, insights are gained into a few possible improvements.

It was found that at times, when the rod is driving the clamping arm to a new

Table 7.3: Mechanical damping ratio of prototype A2.2.

Frequency (Hz)	Mech. damping ratio ξ_m
40	0.0200
43	0.0115
46	0.0090
49	0.0062
51	0.0070
55	0.0200
62	0.0230

position, the clamping arm may not be kept perpendicular to the rod. This has negative effects on both the tuning range and damping. To mitigate this problem, the distant between the clamping point to the rod should be designed as short as possible to minimise the bending moment about the y-axis. Increasing the thickness of the clamping arm where it is threaded on the rod can also help. Another improvement can be made is the vertical coupling between the rod and the roof mass. It is very important that between the two there is no free movement. Due to the low level of vibration that is being harvested, even the clearance of the ball bearings may introduce some damping. To minimise damping, the rod and the proof mass should be spring loaded with a high stiffness spring. It is confident that, with careful design and production manufacturing, the mechanical damping of this concept can be reduced to about 0.007, which is observed in some frequencies in prototype A2.2.

The tuning range for prototype A1, A2.1 and A2.2 are 36 %, 32 % and 44 %. To put these figures into perspective, a modulus and impedance matching with an *ideal* inductor (c.f. Chapter 6) can only give a tuning range of 8.2 % and 36 % FWHM, respectively. While the frequency range by electrical tuning can run into its theoretical limit, the frequency range of this concept can be extended by altering the physical dimensions. As (7.3) suggested, the tuning range can be extended by increasing the ratio of L_1 and L_2. In addition, the tuning range can also be extended with a variable cross section beam. As the pivot roller gets closer to L_1, the structure becomes more frequency sensitive. With a low mechanical damping and a frequency sensitive structure, an potential issue is that the harvester may not remain exactly in tune for a very long time in a vibrating condition. If that is the case, an electrical tuning circuit (e.g. modulus matching) will be beneficial as a complement for fine tuning of the harvester.

In summary, concept A has shown some very positive initial results both on the tuning range and the mechanical damping ratio. The test results of the prototypes have proven that concept A is an effective approach for semi-active tuning purpose.

Furthermore, by allowing all the mechanical and electrical components to be placed inside the proof mass, concept A demonstrates a great potential to become a practical approach towards semi-active tuning.

7.5 Prototypes on Varying Stiffness

In this section, another novel concept for semi-active tuning is presented. The concept utilises the non-linear springs to adjust the overall stiffness of the structure. In its simplest form, an example of the proposed concept is illustrated in Figure 7.15. The mechanism consists of a 2-layer piezoelectric cantilever beam, a proof mass and two conical springs. The resonant frequency of the proof mass depends

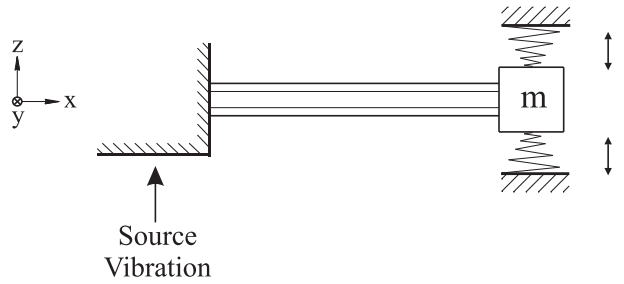

Figure 7.15: Concept of semi-active tuning by non-linear springs.

on the total spring constant of the system. In the illustrated configuration, the total spring constant is the sum of the spring constant of the piezoelectric beam and the two conical springs. Thus, the resonant angular frequency can be estimated as

$$\omega = \sqrt{\frac{k_{beam} + (2k_{spring})}{m}}. \tag{7.5}$$

Non-linear springs such as conical springs or progressive springs exhibit a different spring constant for a different compression distance. Based on this fact, the resonant frequency of this harvester can be tuned by adjusting the compression distances of the two conical springs. As (7.5) suggested, the tuning range can be maximised by keeping the spring constant of the cantilever beam relatively small compared to that of the two non-linear springs. The biggest advantage of this tuning mechanism is that it eliminates the movements between the beam and the proof mass completely, which can potentially improve mechanical damping, reliability and repeatability. For this concept, a part from the PZT beam itself, the only additional source of mechanical damping is from the conical springs, which can be minimised by using the telescoping type of conical springs. Under vibration, contact between coils of the spring should be avoid where possible. Another advantage of this concept is that an extension of frequency range does not require

a proportionally increase in size. It only requires a careful design of the non-linear springs.

7.5.1 Prototype B1 design

To initiate a preliminary test on this concept, the design for a prototype B1 showing in Figure 7.16 is conceived. The main components include a steel cantilever

	Parts
1	PZT sheet
2	Steel beam
3	Spring
4	Rod
5	Mass
6	Pusher
7	Bearing

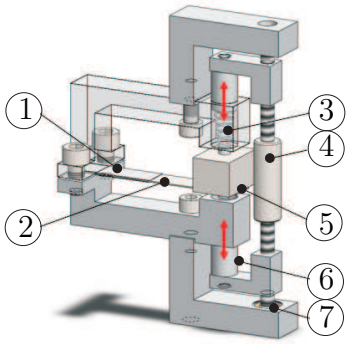

Figure 7.16: 3D Model of Prototype B1. The cantilever beam consist of two PZT layers and a stainless steel substrate. Two conical springs are facing against the proof mass. Compression of the conical springs can be adjusted by turning the rod manually.

beam with one PZT sheet bonded on each side, a proof mass, two conical springs and a threaded rod for manually adjusting the compression of the springs. The piezoelectric material is PSI-5A-S4-ENH from Piezo System, Inc. The schematic of the cantilever beam is illustrated in Figure 7.17. Wires are soldered on the coper

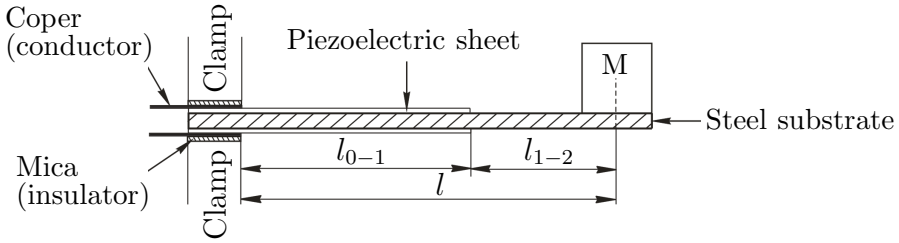

Figure 7.17: Schematics of the single mass cantilever beam in prototype B1.

plates at the fixed end to avoid any influences on the dynamics of the cantilever beam. Numerical values on dimensions and material properties of the design can be found in Table B.9 of Appendix B. The force versus distance characteristics of the conical spring is measured. By differentiating the forces with respect to distance, a spring constant curve in Figure 7.18 is obtained.

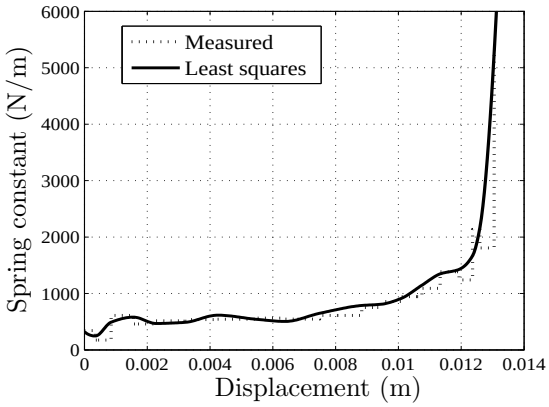

Figure 7.18: Measurement of a single conical spring characteristics for prototype B1. Least squared fitting is used to obtain a continuous curve.

As expected, the characteristics of the conical spring is non-linear, and its non-linearity increases as it is compressed further. This implies that the frequency can become very sensitive to the spring displacement at high frequency. Practically, the usable range of this spring is only from 0 to 12 mm, which corresponds to the spring constant range from 400 to 1450 N/m. To simplify comparison, this prototype is designed to have a similar frequency range to prototype A. This requires a proof mass of approximately 32 g. The spring constant of the cantilever (837 N/m) was designed to be small compared to the total spring constant of the springs (800 N/m - 2900 Nm) to maximise tuning range. By applying the lumped-mass model and (7.5), the tuning range of this design is estimated to be 36 - 54 Hz.

7.5.2 Prototype B1 testing

By following the specifications discussed in the previous design section, prototype B1 is built and tested on the shaker as can be seen in Figure 7.19. The procedure

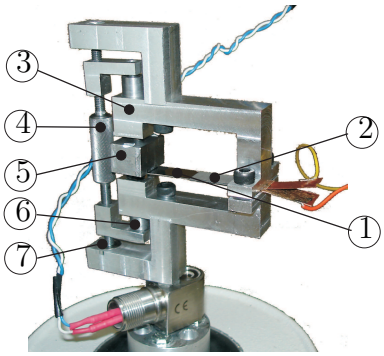

Figure 7.19: Prototype B1 was built and tested on the electromagnetic shaker.

to carry out the measurement in LabVIEW™ is the same as the one on other prototypes. In order to compare its mechanical performance with the previous prototypes, the initial testing was carried out by electrically shorting the two PZT layers. Hence, the electrical damping is zero. The measured relative velocity of the proof mass is shown in Figure 7.20. The test results show that prototype B1 has

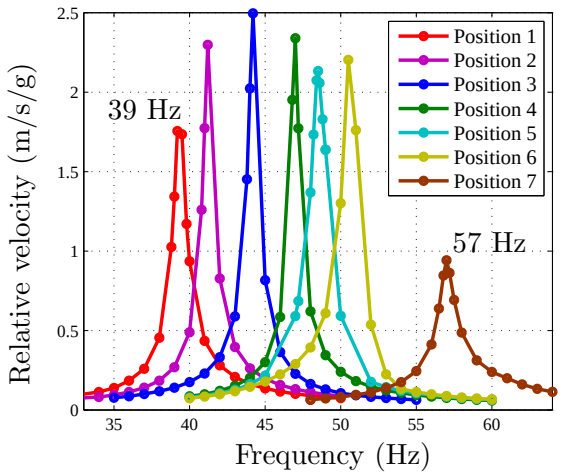

Figure 7.20: Measured velocity FRF of prototype B1. Tuning range is from 35 to 57 Hz, or 48 ±19 %.

a tuning range from 39 to 57 Hz, which agree well with the estimated 36 - 54 Hz range. Compared to prototype A2.2, the tuning range of this prototype is slightly reduced. Figure 7.20 also shows that this prototype has a low and consistent mechanical damping over its frequency range. Table 7.4 provides numerical values of the mechanical damping ratio for each measured frequency. Measuring at about

Table 7.4: Mechanical damping ratio of prototype B1.

Frequency (Hz)	Mech. damping ratio ξ_m
39.4	0.0110
41.2	0.0081
44.2	0.0073
47.2	0.0065
48.5	0.0075
50.2	0.0068
56.7	0.013

0.7 of mechanical damping ratio for most of its frequency range, Table 7.4 confirms the remarkable performance of prototype B1. Compared to prototype A2.2, the mechanical damping of prototype B1 is lower and more consistent. This has proven

that the elimination of movement between the mass and the beam does improve the mechanical damping.

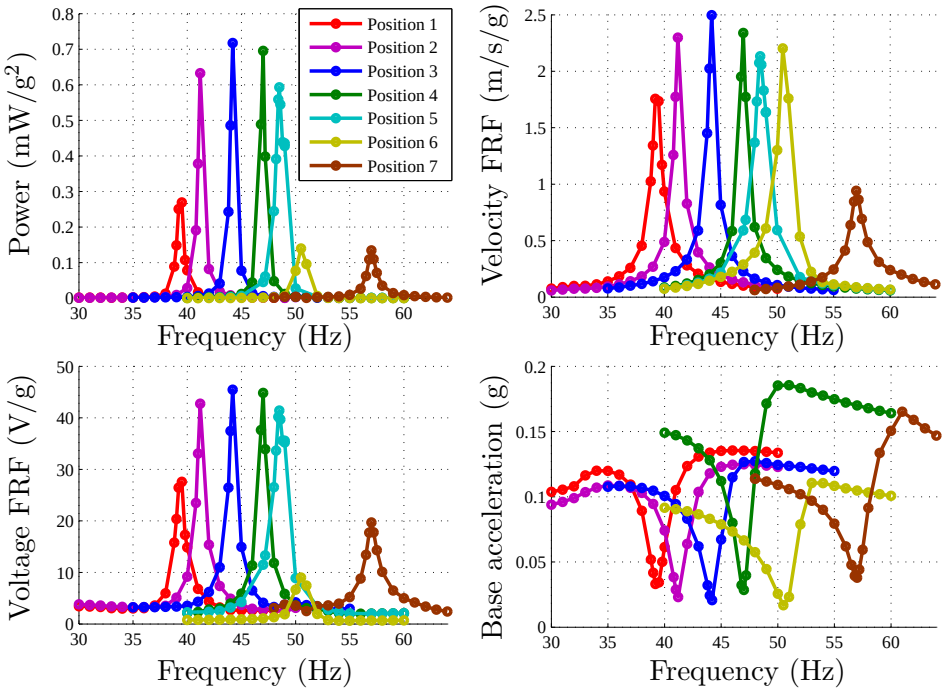

Figure 7.21: Prototype B1 test results with optimal load resistance.

Since PZT layers are bonded on the cantilever beam, the next test is to measure the voltage and power output. To demonstrate the maximum potential of the prototype, the load resistance for each frequency is tuned to optimum with a potentiometer. The results for power, relative velocity and voltage in FRF are presented in Figure 7.21. The base acceleration around each resonant frequency is under 0.1 g, which is in accordance to the level mostly found in industrial machine vibrations. Due to the weight of the proof mass, and the stiffness of the PZT layers, prototype B1 does not appear to generate significant power output. The power output can be increased by having a heavier proof mass and thicker and/or wider PZT layers.

7.5.3 Prototype B2 design

As a proof of concept, it is decided to create a prototype that is much closer to a fully functional energy harvester with semi-active tuning capability. The tuning of this prototype will be performed automatically by an electrical motor with encoder feedback. To meet the power requirement of this project, it is aimed to design this

prototype to generate at least 1 mW at a base acceleration of no greater than 0.1 g. According to the study of vibration characteristics detailed in Chapter 3, one of the most favourable frequency ranges is 22 - 52 Hz. This frequency range is used as a specification for the design of this prototype. To facilitate the manufacturing, off-the-shelf components are used where possible. This decision has some influences on the design and the size of the prototype. With this constrains designing a harvester that meets the power output and tuning frequency is no easy task. Many factors come into play such as PZT beam length, width, thickness, substrate material, proof mass (size and density), max displacement, conical spring length, stiffness, rate of change of stiffness, motor specifications and gearbox output torque, rod diameter and so on. Optimising all these factors are required to obtain the best combination of minimum base acceleration, frequency tuning range and power output. Therefore, design and component selection is an reiterative process. After which, the piezoelectric beam chosen is the Volture™ V20W from Midé Technology Corp. This beam is suitable because it can generate up to 6 mW of power, and its physical size and stiffness fit into the design. After testing a few off-the-shelf conical springs in a hydraulic instrument, the most suitable one was found. The spring constant curve of the chosen conical spring is shown in Figure 7.22. It is

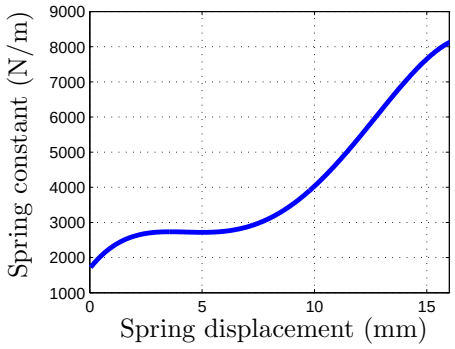

Figure 7.22: Measured conical spring constant versus displacement.

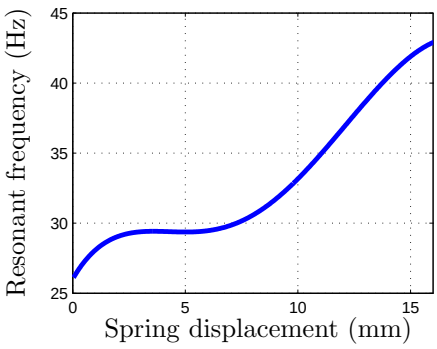

Figure 7.23: Estimated frequency range of prototype B2: 26 - 43 Hz.

interesting to see that the spring constant is varying in a different rate at different portion of the spring displacement. The portion that the spring constant increases linearly with respect to displacement (6 - 15 mm) is ideal for the semi-active tuning purposes, whereas the the portion where the spring constant stays the same (3 - 6 mm) is undesirable. By incorporating tapper wire and variable pitch, a conical spring with optimal characteristics can be designed. However, for proof of concept, this conical spring is deemed adequate. Based on the measured spring constant, the optimal proof mass is about 300 g to achieve the frequency range from 25 - 50 Hz. The composition of the overall spring constant is 4100 N/m from the cantilever beam and 3540 N/m - 16230 N/m from the two conical springs from 0 to 16 mm. By applying the lumped-mass model, the frequency range is estimated

to be 26 - 43 Hz as shown in Figure 7.23. Since the full compression of the springs is 19 mm, it it likely that the upper frequency limit is higher than estimated if the springs can be compressed further by the electric motor.

To avoid custom made parts, gearbox and electric motor are selected from the off-the-shelf products. The specifications of the available components have influence on the design. As mentioned earlier, it is advantageous to integrate most of the components as part of the proof mass. Bearing this in mind, the first design shown in Figure 7.24 was conceived. The design is based on the Tamiya 70188 mini motor

	Parts
1	PZT beam
2	Mass
3	Spring
4	Pusher
5	Motor & gearbox
6	PZT connector
7	Pusher holder

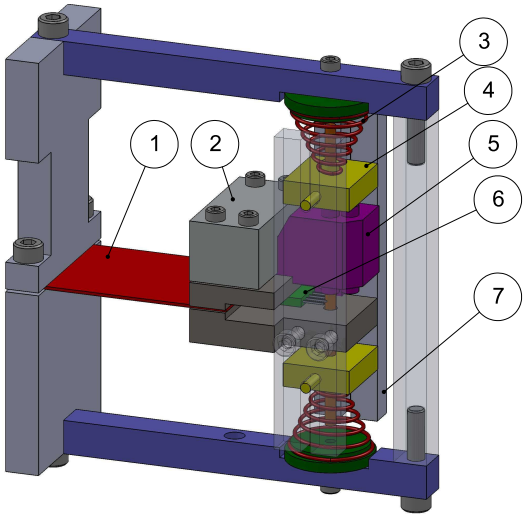

Figure 7.24: 3D Model design of a motorised semi-active tuning prototype. The motor, gearbox, pushers and all necessary electronics are part of the proof mass.

gearbox that comes with a long hexagonal shaft. The DC motor has a free-run current of 60 mA at 3 V. By rotating the shaft that has opposite threads on each end, the position of the pushers are controlled by the electric motor. There is one major issue associated with this design. The base vibration is transmitted via the conical springs to the pusher, then to the shaft and finally reaches the proof mass. It is important that the base vibration is transmitted to the proof mass with minimum losses through all these linkages, otherwise it will lead to a high mechanical damping. Among all the linkages, the weakness was identified to be the coupling between the shaft and the Tamiya gearbox. This is simply because the gearbox was not designed to restrain the longitudinal movement of the shaft. Therefore, this can be a major source of mechanical damping. Creating a harvester with all the components as part of the proof mass required careful design and custom parts. However, the main purpose here is to demonstrate the performance of the tuning concept. With the limited options of the commercially available components, an alternative design that has the motor mounted on the fixed base is proposed. Its 3D model is shown in Figure 7.25. The major improvement of this design is the

	Parts
1	PZT connector
2	PZT beam
3	Mass
4	Pusher holder
5	Spring
6	Pusher
7	Flanged bearing
8	Pinion gear
9	Motor & gearbox

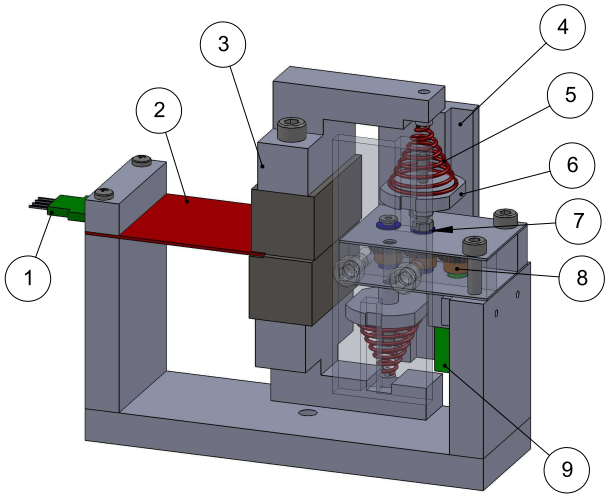

Figure 7.25: 3D Model of Prototype B2.

rotating shafts, there is one for each spring. In this configuration, each shaft is pushed against a flanged bearing by the conical spring, eliminating the vertical movement of the shafts. The proof mass consists of four pieces, the two closer to the beam are made of steel, and the two farther away are made of aluminium. This arrangement keeps the centre of mass close to the end of the beam. The key components of this prototype include: DC motor and gearbox, output shaft encoder, h-bridge, power conditioning, super capacitors and the micro-controller. The design of each components is discussed as follows.

The motor and gearbox set is the mini-gearbox 1095 from Polulu, which has a 250:1 gear ratio and output speed of 50 rpm. The output shaft of the gearbox drives a pinion gear, which drives the two shaft with 1:1 ratio pinion gears. The calculation results of the minimum torque presented in Table 7.5 confirms that the selected motor and gearbox can compress the conical springs to its full length. In the calculation, the minimum torque require to compress the spring does not include the friction on the thread, which can be considerable but hard to determine at the design stage. To be conservative, the gearbox that can provide 2300 gf.cm at 6 V is selected. The prototype is intended to be operated at 3.3 V, this would approximately reduce the torque by half. But even with this factored in, the torque produced by the gearbox should be sufficient to compress the spring to its full length. There is inefficiency involved when the gearbox torque is much higher than the required torque because the time required is longer than needed, which in term consumes more energy for tuning. The driving torque can be optimised for the product version where custom parts are accessible.

The purpose of the encoder is to sense the number of revolution of the motor, so that with the help of a lookup table, the motor can tune the harvester to the desired

Table 7.5: Minimum torque required and the travel time for full compression of the chosen conical springs. Calculated values are underlined.

Description	Value	comment
Rod pitch	0.5 mm	M3
Rod mean dia.	2.8 mm	M3
Max spring force	20 kg	For 2 springs
Gearbox output torque	2300 gf.cm	At 6 V
Gearbox Output speed	50 rpm	At 6 V
Travel length	18 mm	
Mini. torque	320 gf.cm	Excl. friction
Travel rev.	40 rev.	
Travel time	43 s	

frequency. Generally encoders measure the shaft the DC motor directly (from the input shaft of the gearbox) to obtain high resolution measurement. However, the chosen gearbox and motor set does not come with an encoder. Hence an external one has to be designed in the prototype to measure the output shaft. Optical encoders normally required a current in the order of tens of mA, which is excessive for the prototype. One of the most power efficient encoder is the omnipolar Hall effect sensor SL353. It only requires 0.33 mA at typical operation. It is used with a tiny permanent magnet (1 mm $\times$ 2 mm $\times$ 3 mm) fitted on the output shaft of the gearbox. The measurement resolution in this arrangement is relatively low, but it is considered adequate for prototyping purposes.

The module EHE004 from Volture™ is chosen to be the power conditioning circuit. Its job is to convert AC to DC, and regulate the rectified DC to a suitable and stable DC voltage. It is built upon the LTC3588-1 Piezoelectric Energy Harvesting Power Supply IC from Linear Technology. Since it is optimised for piezoelectric energy harvesting applications, the module is extremely power efficient, and it works with the Volture™ V20W PZT beam seamlessly. The module is configured in the following settings: 3.3 V regulated DC voltage, series connection of PZT layers, and full bridge rectifier. When active the module is expected to draw 150 μA.

An H-bridge is required to drive the DC motor in both directions. The H-bridge is constructed by two p-channel (BC 640) and two n-channel (BC 639) signal transistors, which are rated at 1 A and its more than sufficient to drive the DC motor that has a free-run current of 30 mA. Diodes are used to protect the circuit against the back-EMF of the motor.

As for energy storage, there has been some debate about rechargeable batteries versus super capacitors in the energy harvesting community [81, 5]. The merits and

drawbacks of rechargeable batteries and super capacitors are summarised in the Table 7.6. Since the technologies for rechargeable batteries and super capacitors

Table 7.6: Rechargeable batteries versus super capacitors for energy harvesting applications.

Energy storage	Merit	Drawback
Rechargeable batteries	· High energy density · Low leakage current · Stable voltage output	· Few recharge cycles · High ESR · Complex charging circuit
Super capacitors	· Infinite recharge cycles · High peak current · Low ESR · Simple recharging circuit	· Low energy density · High leakage current · Voltage drops when discharged · Need balancing circuit when connecting in series

are still evolving, some of the claims in the table may not be valid in even a few years time. For example, the Thinergy® solid state rechargeable batteries from Infinite Power Solutions have sufficient recharge cycles for the entire lifetime of the harvester. However, their peak current and internal resistance are still a problem for the Ranger wireless sensor. Hence, super capacitors are considered to be more suitable. The HW207 super capacitors from Cap-xx are chosen because they features high capacitance (400 mF), low ESR, low leakage current (1.6 μA), high peak current (57 A) and high pulsed power. They are rated at 5.8 V. Four of these capacitors are used, each pair is connected in series and the two pairs are connected in parallel. The capacitor bank is connected in parallel with the input capacitors of the EHE004 module. This allows the capacitors to be charged even when the power conditioning circuit is shut down.

A micro-controller is required to process the sensor information and tune the harvester to the desired frequency. At the time of this study, the most power efficient micro-controller is the PIC24F16KA102. It is designed for energy harvesting applications. The micro-controller only draws 195 μA when running at 1 MHz, and from 20 nA to 500 nA in sleep mode depending on the active peripherals. To reduce the development time, the evaluation board XLP 16-Bit is used.

A fully functional semi-active energy harvester will require the information of the base vibration. Since it was the assumption that the harvester will be working with Commtest's wireless accelerometer sensor, the harvester will get the base vibration information from the wireless sensor. For proof of concept, this prototype is to demonstrate that once it receives the frequency peak from the accelerometer, it can tune itself to that frequency based on the lookup table stored in the EPPROM.

The lookup table correlates the resonant frequency of the harvester to the number of revolutions. Once the harvester is in tune, the micro-controller shuts down all the electronics through a power MOSFET and then goes to sleep mode. These basic functionalities are deemed sufficient to demonstrate the tuning capability of the harvester.

7.5.4 Prototype B2 testing

The harvester is built according to the design specifications. The photos of the manufactured prototype B2 are shown in Figure 7.26. One of the pusher holder is

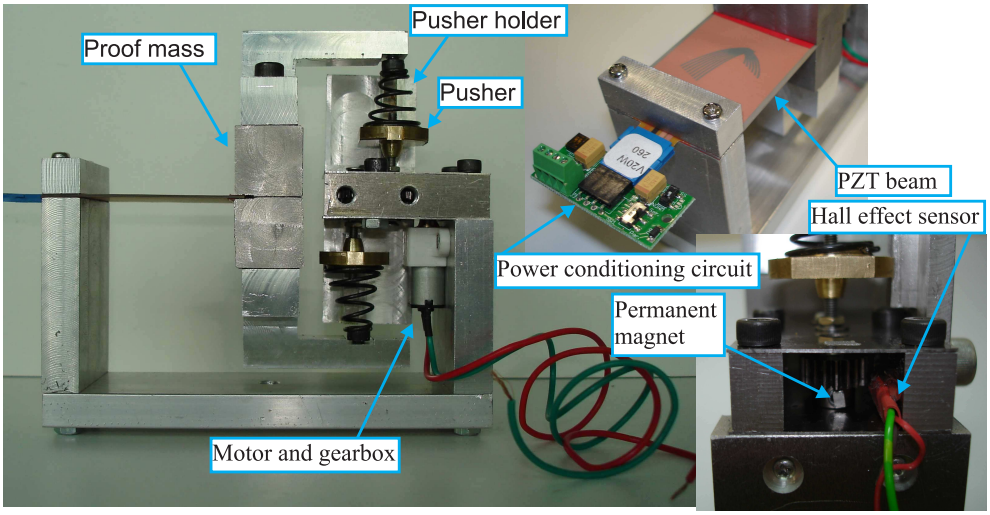

Figure 7.26: Prototype B2 was manufactured and assembled.

taken off to get a clear view of the conical springs, the turning shafts and the motor. Lubricant was applied to all the moving parts to minimise energy consumption when tuning. As per design, it includes an electric motor, a Hall effect sensor, and the power conditioning module. Like all the previous prototype, the first test is to short the piezoelectric layers to evaluate the mechanical performance of the prototype, which includes mechanical damping and tuning range. With the same procedures carried out in LabVIEW™, the velocity in Figure 7.27 is obtained. The tuning range appears to be 24 - 50 Hz, which is very close to the target range 22 - 52 Hz. By looking at the relative terms and comparing it with the ±3 % frequency shifting by modulus matching, the ±35 % tuning range of this prototype is actually very remarkable. This tuning range is wider than any of the previous prototypes. The values for the measured mechanical damping are shown in Table 7.7. The numerical values suggest that there is no obvious improvement on mechanical damping over its predecessor. For most of the range its around 0.01 or below. By comparing the mechanical performance of prototype B1 and B2, it

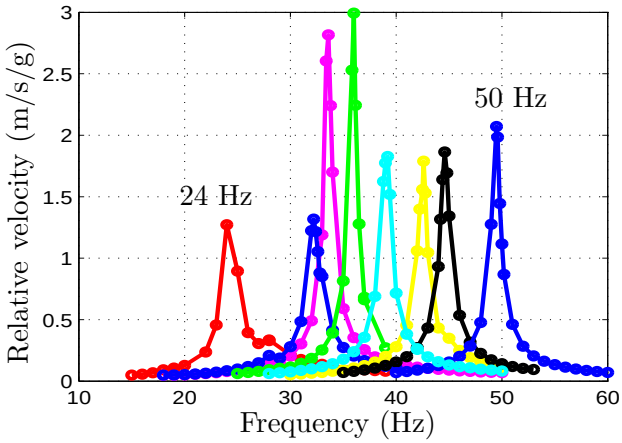

Figure 7.27: Measured relative velocity FRF of prototype B2. Tuning range is from 24 to 50 Hz, or 37 Hz ±35 %

Table 7.7: Mechanical damping ratio of prototype B2.

Frequency (Hz)	Mech. damping ratio ξ_m
24.1	0.0250
32.2	0.0180
33.6	0.0082
36	0.0065
39.2	0.0108
42.6	0.0102
44.6	0.0094
49.5	0.0077

has demonstrated that the frequency range of concept B can be extended without having to significantly increase the mechanical damping.

The next step is to evaluate the electrical performance of the prototype. In the test, the power conditioning module is not used. This is because with the power conditioning module, it is very difficult to determine the maximum power the harvester is producing. Instead, a potentiometer is directly connected to the PZT terminals, and for each excitation frequency, the load resistance is tuned to optimal and the power and other response are recorded. By following these procedures, the measurement in Figure 7.28 is obtained. The testing results show a very high power output produced by the harvester around the frequency range 30 to 40 Hz, with the maximum point of 800 mW/g^2. Outside of this frequency range, the power output reduced significantly due to the increase of mechanical damping.

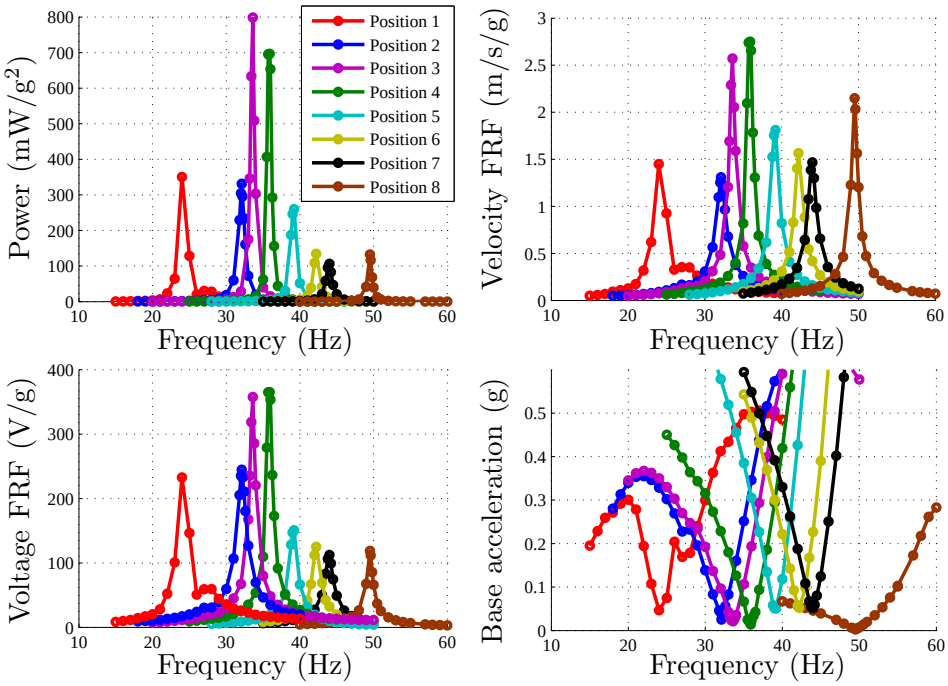

Figure 7.28: Prototype B2 performance with optimal load resistance.

Even with the significant difference in power output, the minimum power is still above 100 mW/g^2, and it translates to 1 mW per 0.1 g of base acceleration. From the base acceleration measurement, it can be seen that all the peak response of the harvester was measured at a base acceleration under 0.1 g, which is close to the acceleration level found in most machine vibrations. The optimal resistances used in the experiments were measured from 100 to 200 kΩ. The variations are believed to be caused by a combination of the mechanical damping and the excitation frequency. By comparing the power output of prototype B2 in Figure 7.28 and prototype B1 in Figure 7.21, it has demonstrated that while the mechanical damping determines how effective the structure is to amplify the base acceleration, it does not directly indicate how much power the harvester can produce. This is because with the same structure and frequency range, the power can be increased by mounting a heavier proof mass and a stiffer PZT beam. For a comparable mechanical damping and frequency range, the power of prototype B2 is 1000 times the power of prototype B1. Proof mass is always proportional to the power output, and the proportionality is partly determined by the mechanical damping.

The energy consumption of all the electronic components are tested with the harvester, the results are summarised in Table 7.8. In the testing, the power is provided by a bench power supply at 3.3 V, and the current drawn by the components of concerned is measured. The current drawn by the electric motor with the H-

Table 7.8: Summaries of prototype B2 electrical test performance and comparison to design specifications.

Items	Design	Experiment
Tuning range Operating voltage	22 - 52 Hz 3.3 V	24 - 50 Hz 3.3 V
DC motor and H-bridge	· 50 mA · 50 rpm · 43 s full range · 7100 mJ	· Wind up: 60 mA for 50 s · Wind down: 60 mA for 47 s · 9300 - 9900 mJ
Hall effect sensor	· Active: 0.33 mA · Sleep: 1.8 μA or 0 if shut down by a MOSFET	Same
Micro-controller PIC24F16KA102	· Run at 1 MHz: 195 μA · Sleep: 20 nA - 500 nA	· Run at 1 MHz: 1 mA · Sleep: 500 nA
Power conditioning AC-DC and DC-DC	· Active: 150 μA · Sleep: 450 nA	· Active: 150 - 200 μA · Sleep: 450 nA
Energy storage	· Super cap 0.4 F at 5.5 V $\times$ 4 · 24200 mJ · Leakage current: 1.6 μA each	· Leakage current: 5 μA each
Total power consumption	· Active: 51 mA at 3.3 V: 169 mW ○ For 43 s, 7240 mJ · Sleep: 8 μA	· Active: 61 mA at 3.3 V: · 202 mW ○ For 50 s, 10100 mJ · Sleep: 21 μA
Power harvested	· 1 mW at 0.1 g	· 100 - 800 mW/g^2 = 1 - 8 mW at 0.1 g or = 1 mW at 0.036 - 0.1 g
How often can be tuned	· At 1 mW · Full range: 121 min · 10 % range: 17 min	· At 1 mW · Full range: 169 min · 10 % range: 24 min

bridge was measured in the oscilloscope. It was observed that the motor took longer to compress the springs than to release them. This is an expected outcome because more energy is required to compress the springs. When the spring compression approaches to the limit, a small increased in current was observed (to about 63 mA), but in the meantime, the voltage dropped to about 2.7 V. This only happened in the last 4 seconds before the springs are fully compressed. In most of the compression time, the motor consumed slightly below 60 mA. The current drawn by the Hall effect sensor was tested to be close to 0.33 mA. The current drawn by the micro-controller when performing frequency tuning is higher than expected because its i/o's need to supply the base current required for the H-bridge. The power conditioning module was tested with the harvester, and it was observed that the current consumption was about 150 to 200 μA. The low power operational amplifier 628-89431BCFN (0.5 μA typ.) from Seiko was used to balance the super capacitors. The leakage of the super capacitors with the balancing circuit were then tested independently. After 24 hours as the leakage current become stable, the total current drawn by all super capacitors and the balancing circuit was measured to be about 20 μA. By comparing the values in Table 7.8, the actual performance of the harvester is very close to the design specifications. One of the highlights is the total energy consumption required for the harvester to tune for the whole range. When tuning is active, the total supply current is 61 mA at 3.3 V. For 50 seconds, the total energy consumption is 10100 mJ. This corresponds to about half of the energy stored in the super capacitors. Given that it is impossible to redraw all the energy stored in the super capacitors, drawing half is reasonable as the voltage drop is only less than 30 %. By looking into the composition of the total current consumption 61 mA, it can be found that more than 98 % (60 mA) of the current is actually drawn by the DC motor, dwarfing the current required by all the other electronic components combined. This means the motor should be the first component to look at when it comes to improving power efficiency of the harvester. Another highlight is the energy generated by the harvester. For the whole tuning range, the harvester is able to generate 100 - 800 mW/g^2, this translates to 1 - 8 mW at 0.1 g of base acceleration, or if the required power is kept constant, 0.036 - 0.1 g would be required to generate 1 mW. In the experiment, the actual base acceleration was slightly lower than that and the power generated was about 0.5 - 1 mW, which is more than the power of 0.32 mW that the wireless sensor needs. Based on 1 mW of power output, the time required to accumulate enough energy for a full range tuning is 169 minutes, or about 3 hours. Given that for the same machine, its vibration frequency does not change often, tuning in every 3 hours is more than sufficient. Experts in machine vibration monitoring suggested that even tuning once every few days would be sufficient. Moreover, a full range frequency adjustment is rarely needed in practice, an adjustment of about 10 % of the frequency is more realistic. In average, the harvester can adjust 10 % of its frequency in every 24 minutes.

7.5.5 Concept B discussions and summaries

Concept B is to adjust the resonant frequency of the harvester by adjusting the compression of two conical springs against the proof mass. With emphasis on tuning range and mechanical damping, prototype B1 was created. The test results show that prototype B1 has very low and consistent mechanical damping over its frequency range. However, the proof mass and the stiffness of the PZT layers limited its power output. Subsequently, the second version, prototype B2 was designed and manufactured aiming to improve the tuning range and power output. In addition, prototype B2 features automatic tuning capability with the inclusion of an electric motor, an encoder, a H-bridge, a power conditioning circuit and a micro-controller. As predicted, both the tuning range and power output of prototype B2 have been significantly improved over its predecessor. Despite the remarkable performance of prototype B2, insights into a few possible improvements are gained through the design and build exercise of prototypes B1 and B2. Recommendations of possible improvements on mechanical damping, frequency tuning range, energy efficiency for frequency tuning and energy storage, as well as strategies for frequency tuning are discussed in the following paragraphs.

Due to the number of mechanical components involved, there are many potential sources of mechanical damping if the harvester is not designed properly. Fortunately both of the two prototypes performed very well in the mechanical damping tests. If this concept was to build to a commercial product, the overall size matters. Hence, it becomes very necessary to integrate all the mechanical and electrical parts to the proof mass. To minimise mechanical damping, the designer must consider the coupling between parts so that the base vibration can be transmitted losslessly to the proof mass via the springs. A possible improvement of mechanical damping on prototypes B1 and B2 is to fasten/glue both ends of the springs. The reason this was not done was because it is preferred not to make the prototype permanent in case small adjustment if needed. However, any disengagement of the spring and the pusher can result in mechanical damping, and this has evidently happened during the tests of both prototypes near their low frequency limits. Near the high frequency limits, additional mechanical damping is caused by the highly non-linear spring constant of the compressed springs. As the conical spring gets compressed towards its full length, the spring constant gets more non-linear and it constrains the displacement of the proof mass. This is an inherent problem of the concept, and it can be mitigated by a careful spring design. A more desirable spring characteristics is one with a spring constant that does not change rapidly near full compression. This can be achieved by incorporating tapper wire and variable pitch into the conical spring design. Based on the performance of the prototypes, it is believed that the achievable mechanical damping ratio by this concept can be in the range of 0.0065 to 0.01 if it is designed and manufactured to an industrial quality. The key to the frequency range this concept can achieve is the conical springs. Prototype B2 has demonstrated a very wide tuning range even

with an off-the-shelf conical spring. Therefore, it is believed that the frequency range can be extended beyond ±35 % of the central frequency by custom designed conical springs that are optimised for the purposes. As mentioned earlier, this can be done by incorporating tapper wire and variable pitch into the conical spring design. While this feature can be a grossly expensive option for prototyping, it will not add any noticeable cost compared to manufacturing ordinary conical springs in mass production.

In terms of energy consumption for tuning, there is a lot of room for improvements. Due to the availability of off-the-shelf components, the tuning mechanism in prototype B2 is not optimised for power efficiency. This is particularly true for the electric motor and gearbox set that accounts for more than 98 % of power consumption during tuning. The gears in the gearbox and the brush of the DC motor are responsible for a significant part of the losses due to friction. This can be improved by using a brushless motor, or a piezoelectric motor that is inherently high torque, so it eliminates the need for a gearbox. If a gearbox is used, a careful match of the output torque to the required torque can minimise the tuning time, which in turn minimises the energy consumption. Another significant source of losses is the friction between the rotating shafts and the pushers. It can be minimised by using ball screws. Lastly, yet another source for significant energy losses is the process of manipulating the compression of the conical springs. In the presented designs, energy is required for both compressing and releasing the springs, which is not very efficient. Ideally, a mechanism that has an inverse spring characteristics of the conical springs can be used to store the energy when the conical springs are being released and release energy when the conical springs are being compressed. If all of these suggestions are implemented, it is believed that the energy required for frequency tuning can be dramatically reduced.

Super capacitors are chosen to be the preferred technologies for energy storage, because of the infinite recharge cycles and the high peak current. In prototype B2 when the super capacitors are fully charged, half of its energy is required for a full range tuning. While this is acceptable for prototypes, it is not reliable for a commercial product. The proportion of the energy required for tuning should be much less than half of the stored energy. In addition, for the commercial energy harvester, it is strongly recommended to have a primary non-rechargeable cell as a backup. Primary cells such as TLH-5935 manufactured by Dadiran Batteries can have a shelf life as long as 25 years, and it can supply the energy for either tuning or the operation of the wireless sensor when it is needed. The inclusion of a primary will dramatically increase the liability of the self-powered wireless sensor.

Although it is not implemented in the prototype B2, a tuning strategy would further reduce power consumption for tuning, as well as increase the harvested power. When the harvester is out of tune, it should perform a crass-tuning followed by a fine-tuning to keep itself in tune. Crass-tuning relies on an open-loop control mechanism; it requires the information of the driving frequency, the lookup table

values and the encoder. A fine-tuning uses a close-loop control mechanism; it uses the output voltage, current and/or power of the piezoelectric beam as feedback. It may use a look-up table, or follow a maximum power point tuning method [78]. Considering the energy required to run the motor being 100 times of the energy required for the micro-processor running at 1 MHz, it can be easily justified to have a rigorous power optimisation algorithm running in the processor. This means every time before activating the motor, a precise calculation that minimises the power consumption of the motor should be performed. Errors in controlling the motor directly translate to energy losses. A more sophisticated learning algorithm can take piezoelectric ageing, and other environmental conditions into account to update its lookup table in run time. Such a algorithm would even eliminate the need for the Hall effect sensor. Potentially the mechanical damping of the harvester is very low, and that can present a challenge if it is beyond the resolution of the tuning mechanism. If this is the case, a ±3 % frequency shifting by modulus matching is ideal for fining tuning purposes.

7.6 Conclusions

In this chapter, techniques for tuning the resonant frequency of the harvester mechanically have been investigated extensively. Compared to electrical tuning, a much wider frequency range is more achievable by mechanical actuation. The aim of this chapter was to find an effective mechanism for semi-active tuning. An ideal candidate should have very low mechanical damping and a wide tuning range. Preliminary concepts on shifting the frequency by changing the length of the beam, the position of the mass and the weight of the mass are briefly discussed. In particular, two novel concepts have been proposed.

The first concept (referred to concept A) is to adjust the resonant frequency by shifting the contact point between the proof mass and the cantilever beam. The major advantages of concept A are that it requires relatively little space and energy to perform frequency tuning, and that all the mechanical and electrical components can be easily built into the proof mass to minimise space usage. Hence, a compact harvester can be designed based on this concept. Two prototypes A1 and A2.2 are built and their performances are evaluated. Both of the prototypes require to be tuned manually and do not include piezoelectric layers, since the primary goal was to test their mechanical performances. Prototype A1 has a tuning range of 78 Hz ±18 %, and mechanical damping ratio of 0.0077 - 0.0108. Prototype A2.2 has a tuning range of 51 Hz ±22 %, and mechanical damping ratio of 0.0062 - 0.023. Possible improvements on mechanical damping and frequency range extension are discussed in Section 7.4.6.

The second concept (referred to concept B) is to adjust the resonant frequency by

adjusting the compression distance of non-linear springs, such as conical springs. The major advantage of the concept is the non-existence of relative movements in the single mass cantilever beam structure. This feature significantly reduces mechanical damping. Another advantage is that an extension of frequency range does not require a proportionally increase in size. Based on this concept, two prototypes B1 and B2 are created and tested. Prototype B1 is tuned manually and it has a tuning range of 48 $\pm$19 %, and a mechanical damping ratio of 0.0065 - 0.013. The power output is 0.16 - 0.73 mW/g^2. To demonstrate that both the tuning range and power output of concept B can be increased significantly by a better design, prototype B2 is created. The prototype includes an electric motor, a Hall effect sensor, an H-bridge, a power conditioning circuit and a micro-controller. As it receives a frequency command, it can tune itself to that frequency by the pre-calibrated lookup table. Prototype B2 has a tuning range of 37 Hz $\pm$35 %, it almost covers one of the most favourable frequency band (22 - 52 Hz) found in industrial machine vibrations (c.f. Chapter 3). The mechanical damping ratio of B2 is 0.0065 - 0.025, and its power output is 100 - 800 mW/g^2. All the electronic components are tested rigorously and their energy consumption at active and sleep mode is evaluated. Assuming that the prototype is producing 1 mW at 0.1 g of base acceleration, 24 minutes are required to accumulate enough energy to shift its resonance frequency by 10 %, or it takes about 3 hours of charging time for a full range tuning. As discussed in Section 7.5.5, major energy losses on frequency tuning are identified. There is a lot of room for improvements on prototype B2, especially the energy consumption for frequency tuning, which was not optimised. Nonetheless, the performances of the prototypes have proven concept B to be a promising concept for a semi-active tuning energy harvester.

8

Conclusions and Future work

8.1 Conclusions

For machine condition monitoring applications, wireless sensing are a cost effective solution due to its ease of installation and flexibility with the existing infrastructure. However, till now most of wireless sensors are powered by batteries. The dependence on batteries not only induces high maintenance costs to replace the them, but also has inherent environmental consequences. Energy harvesting, being the main focus of this work, is an enabling technology for wireless sensors to be powered by their environment. Other than infinitely scalable, self-powered wireless sensors allow instillation of the sensor in remote and inaccessible locations. The wireless sensor involved in this research requires an average power of about 0.32 mW. Compared with solar, thermal and radio frequency, vibration is considered to be the most reliable energy source for sensors used for machine condition monitoring. Compared with electrostatic and electromagnetic harvester, piezoelectric harvester is chosen to be to most suitable technology for a vibration-based energy harvester due to its high power density and output voltage.

A literature review is given in chapter 2, where the state of the art in vibration-based energy harvesting using piezoelectric material are summarised. For base acceleration, Roundy et al. [14] used 2.25 m/s^2, the typical acceleration of a microwave oven, and 120 Hz, twice of line frequency, as the basis for the design of their vibration-based energy harvesters. The review also shows that analytical models including lumped-mass and continuum models are widely used in the energy harvesting community. In addition, finite element method are also commonly applied to predict the dynamic behaviour of the harvester. As for techniques of solving narrow bandwidth issues associated with any vibration-based energy harvester, there are three categories of approaches: wide bandwidth structures, frequency tuning by electrical circuits and by mechanical actuation. Each of these techniques show some success in the literature but there are plenty of room for improvements.

Due to the lack of information on machine vibration characteristics in the literature, and its importance towards energy harvester designs, a thorough investigation on the matter is conducted in Chapter 3. From the vibration recordings of 15586 industrial machines, the statistics show that over 97 % of the optimal frequencies of the vibrations are below 500 Hz. The single most dominant frequency is about 25 Hz (half of mains line frequency), reflecting the fact that 2-pole fixed drive induction motors are still prevalent in the industry. As a result, the most favourable frequency band for narrow band harvester is 24.3 - 25.3 Hz, and for wide band harvesters are 22 - 52 Hz and 47 - 102 Hz. The median *rms* vibration amplitude is 0.48 m/s^2. The statistics show that, when the mechanical and electrical damping are equal to 0.01 and the required power output is 500 μW, a harvester needs to have a minimum proof mass of 300 g and a tunable frequency range between 11 to 102 Hz to generate adequate power from 52 % of surveyed machines. The results indicate that large variations in vibration amplitudes and frequencies are present in machinery, and therefore it is unrealistic to design a one-size-fits-all harvester. In some equipment such as cooling fans and oil circulating pumps, the vibration levels are too low to be usable, unless the proof mass is excessively large. The findings serve as a valuable reference for the design of a vibration-based energy harvester that is deployed in industrial machinery.

Since single mass piezoelectric cantilever models are the building block of the design of energy harvesters, chapter 4 is dedicated to acquire a solid understanding of the theories, and to build an experimentally validated model. After deriving a lumped-mass model and a continuum model, a generalised model for piezoelectric cantilever beams is derived. The main purpose of the generalised model is to enable any further analysis on the model to be backward compatible to both lumped-mass and continuum model, which are the two dominating types of models in the piezoelectric energy harvesting arena. Followed by the derivation, the equivalent current circuit and the Thévenin equivalent circuit of the model are presented. The analysis leads to the analytical expression of the source impedance, which explicitly shows how the source impedance is related to the mechanical and electrical parameters of the system. A case study reveals the fact that when electrical damping and mechanical damping are equal, the impedance of the electromechanical system is indeed matched, leading to maximum power output. The case study also predicts that modulus matching can tune the resonant frequency of the harvester by about 10 % of its natural frequency for the commonly available PZT-5H crystal. The tuning range is solely dependent on the coupling coefficient of the PZT material. Finally, experimental validations are performed on PZT cantilever beams with and without a tip mass. Quantitatively, the frequency response of the beam velocity and power output predicted by the model for a whole range of load resistances are in excellent agreement with observations. It is confidant that the model can serve as a reliable tool for the purposes of energy harvester designs.

To investigate the feasibility of multi-modal harvesters, a continuum model for

double-mass piezoelectric cantilever beams are derived using Hamilton's principle in Chapter 5. After showing the equations of motion together with all necessary boundary and transition conditions, the undamped natural frequencies and the mass normalized eigenfunctions are determined through modal analysis. The steady state solution for harmonic base excitation is obtained. Both series and parallel connection for the bimorph are incorporated in the model through the definitions of some geometric variables. In addition, electrode segmentation for power output enhancement is incorporated into the model. The derived model is validated experimentally on a 2-layer piezoelectric beam with two proof masses. In the experiment, the resonant frequencies, velocity frequency response, voltage output and the mode shape of the first two vibration modes are measured and compared with modelling results. In all quantities compared, the model showed excellent agreement with the actual measurements. High credibility means this model can be used to quickly evaluate the performance of a double-mass energy harvester, and design the two resonant frequencies and the power output to desired specifications. Depending on the required bandwidth, a broadband energy harvester can be implemented by an array of double-mass PZT beams for more compactness compared to its single-mass counterpart. The development of this model is an important step forward to solving the optimization problem of double-mass PZT harvesters, and to deriving a generalised model for a PZT beam with any number of proof masses.

Chapter 6 explores the potential of tuning the frequency by modulus and impedance matching. In order for the analysis of an impedance matched system to be valid, an improved continuum model for PZT cantilever beams is introduced. The model takes into account of polarisation losses and electrode layer Ohmic losses. The inclusion of these losses is essential for an impedance matched system where relatively high voltage and current are developed among passive elements in the circuit. The model is experimentally validated on a modulus matched circuit, and on a circuit of a bridge rectifier with a capacitive load. It has demonstrated that a frequency range of 8.2 % can be achieved through modulus matching for the PZT-5A material. The experimental validation on a full bridge rectifier with a capacitive load demonstrates that the improved model can simulate a PZT beam with any electrical load (linear/non-linear and of any impedance). All experimental observations quantitatively agree well with the model.

The study in Chapter 6 has shown that electrical tuning is only effective for small frequency range. To maximise the tuning range, a concept for a conjugate matched system is proposed. The circuit consists of a fixed value inductor and a variable capacitor and a load resistor. The case study reveals that the contact losses for the particular PZT beam are negligible while the polarisation losses account for most of the losses in the conjugate matched system. With polarisation losses considered, the theoretical maximum frequency range can be achieved by a conjugate matched system is 36 %, but the range diminishes as the inductor ESR losses increased. It

is found that it is not the absolute value of the R_{esr} but the ratio of R_{esr} to L that influences the tuning range. In the presented analysis, a procedure is developed to deduce the requirements of the inductor and the required capacitance and resistance values. The simulation results suggest that with commonly available PZT material and inductors today, conjugate matching can only be implemented for a small mass, medium frequency and very low power output PZT harvester. The challenges are the loss tangent of the PZT material and the ESR to inductance ratio of inductors. Nonetheless, as material science and manufacturing technologies incrementally improved, the concept presented in this chapter for conjugate matching will eventually become more achievable for high power and low frequency harvesters.

In Chapter 7, techniques for tuning the resonant frequency of the harvester mechanically have been investigated extensively. The aim of this chapter was to find an effective mechanism for semi-active tuning. An ideal candidate should have very low mechanical damping and wide tuning range. In the investigation, two concepts (A and B) are proposed, and four prototypes (A1, A2, B1 and B2) are designed and built, and their performances are evaluated.

Concept A is to adjust the resonant frequency by shifting the contact point between the proof mass and the cantilever beam. The major advantages of concept A are that it requires relatively little space and energy to perform frequency tuning, and that all the mechanical and electrical components can be easily built into the proof mass to save space. Prototype A1 has a tuning range of 78 Hz ±18 %, and mechanical damping ratio of 0.0077 - 0.0108. Prototype A2.2 has a tuning range of 51 Hz ±22 %, and mechanical damping ratio of 0.0062 - 0.023.

Concept B is to adjust the resonant frequency by adjusting the compression distance of non-linear springs, such as conical springs. The major advantage of the concept is the non-existence of moving parts on the cantilever beam and mass structure. This feature significantly reduces mechanical damping. Prototype B1 has a tuning range of 48 ±19 %, and a mechanical damping ratio of 0.0065 - 0.013. The power output is 0.15 - 0.73 mW/g^2. Prototype B2 includes an electric motor, a Hall effect sensor, an H-bridge, a power conditioning circuit and a micro-controller. As it receives a frequency command, it can tune itself to that resonant frequency by the pre-calibrated lookup table. Prototype B2 has a tuning range of 37 Hz ±35 %, it nearly covers one of the most favourable frequency band (22 - 52 Hz) found in Chapter 3. The mechanical damping ratio of B2 is 0.0065 - 0.025, and its power output is 100 - 800 mW/g^2. All the electronic components were tested rigorously and their energy consumption at active and sleep mode is evaluated. Assuming the prototype is producing 1 mW at 0.1 g of base acceleration, 24 minutes are required to accumulate enough energy to shift its resonance frequency by 10 %, or it takes about 3 hours charging time to tune the full range. Concept B has proven to be a promising concept for a semi-active tuning energy harvester.

In summary, all the objectives have been met. The favourable frequency range and vibration levels of industrial machine vibrations have been identified. An accurate model for piezoelectric energy harvesters has been developed. Three most attractive solutions for wide frequency range energy harvesters, multi-modal, electrical tuning and mechanical tuning, have been studied theoretically and experimentally. The best solution was identified to be concept B, and a practical implementation has been demonstrated by prototype B2, which produced 1 mW from 24 to 50 Hz at a base acceleration range of 0.036 - 0.1 g. While energy harvesting for wireless sensors does not have the same kind of impact compared to large scale renewable energy production, it does facilitate the proliferation of wireless sensors, and reduce the dependence on chemical cells. Both of these outcomes are beneficial to the society in terms of productivity and the environment. This work has pushed the envelope of piezoelectric energy harvesting technologies, and provided a practical solution that made a commercial self-powered wireless sensor closer to reality.

8.2 Future work

Given the prevalence of machine condition monitoring in the industries and its high installation costs, the demand for self-powered wireless sensors can only continue to rise. From magazines such as the *Energy Harvesting Journal* [82], recent years many manufacturers have been striving to secure the first to market advantage by providing a reliable solution. There are a lot can be done as a continuation of this work.

For multi-modal harvester, it would be helpful to extend the double-mass piezoelectric cantilever beam model to any number of masses. To push it further, optimisation techniques such as genetic algorithm can be applied to maximise power output and obtain the desirable frequency peaks by finding the combination of geometric dimensions and material properties. Be it an array of multiple-mass straight beams, a stack of multiple-mass spiral beams, an optimised multi-modal harvester can find its commercial advantage for a broadband MEMS harvester.

Impedance matching is an area where an IC or a small footprint module can be developed. Although this work shows that inductor ESR and piezoelectric material losses are the major hurdle of developing an impedance matched system, the presented theories provide insights into the impedance required for each frequency and how it relates to many parameters of the system. A more practical way to implement impedance matching with the current technologies is to emulate the required impedance by electrical switches (e.g. MOSFETs). By sampling the output voltage of the piezoelectric harvester, an current with a desirable amplitude and phase can be generated by the electrical switches, which emulates the optimal impedance.

For mechanical tuning harvesters, further work can be done on the energy optimisation and control strategies of frequency tuning. A learning algorithm should be developed aiming to minimise the tuning effort using a combination of open-loop (lookup table) and close-loop control. The algorithm should be able to optimise the harvester from environmental changes such pressure, temperature and humidity, as well as piezoelectric material ageing by periodically update its lookup table and/or control gains. Alternatively, the control technique called Extremum Seeking Control (ESC) [83] can be used for maximum power tracking purpose. An investigation on a device that has an inverse spring characteristic of the conical spring can be a valuable add-on to the chosen semi-active tuning mechanism. Ideally such device can help counteract most of the friction on the threads when the conical springs are being compressed or decompressed, making frequency tuning much more efficiency. For the semi-active tuning mechanism, emphasis should be placed on miniaturization, robustness and manufacturability. Due to the fact that power output is inversely proportional to mechanical damping, an in-depth investigation on ways to reduce mechanical damping can be very rewarding, and a breakthrough on this area can significantly reduce the proof mass and hence the size and weight of the harvester.

Last but not least, it should be reminded that lead is toxic and it may cause pollution to the environment. Hence products contain lead are not sustainable and will face more and more restrictions in the future. In this work, PZT was chosen because it was readily available and inexpensive. However, for commercial product development, lead-free piezoelectric ceramics should be used. Lead-free piezoelectric ceramics such as BNT-BT, BNT-BKT-BCTZx [84, 85, 86] are widely reported. To identify the most suitable material for energy harvesting applications, more in-depth literature review on lead-free piezoelectric ceramics and performance testing are required.

Bibliography

[1] F. M. Discenzo, D. Chung, and K. A. Loparo, "Power scavenging enables maintenance-free wireless sensor nodes," *Proceedings of the 6th International Conference on Complex Systems*, 2006.

[2] J. Koomey, S. Berard, M. Sanchez, and H. Wong, "Implications of historical trends in the electrical efficiency of computing," *IEEE Annals of the History of Computing*, vol. 33, no. 3, pp. 46–54, 2011.

[3] GE Energy Ltd, "Commtest instruments," *www.commtest.com*.

[4] R. Murugavel, "Taxes instruments white paper - energy harvesting," Nov 2008.

[5] S. Roundy, "Energy scavenging for wireless sensor nodes with a focus on vibration to electricity conversion," Master's thesis, The University of California, 2003.

[6] S. Wojtczuk and K. Reinhardt, "High-power density (1040 w/kg) gaas cells for ultralight aircraft," pp. 49–52, 1996.

[7] E. Topal, H. Kulah, and A. Muhtaroglu, "Thin film thermoelectric energy harvesters for mems micropower generation," 2010.

[8] "Micropelt," 2008.

[9] Loreto Mateu and Francesc Moll, "Review of energy harvesting techniques and applications for microelectronics," *Proceedings of SPIE - The International Society for Optical Engineering*, vol. 5837 PART I, pp. 359–373, 2005.

[10] Jaymi Heimbuch, "Intel demos rf energy harvesting technology," 2009.

[11] K. Finkenzeller, *RFID Handbook: Fundamentals and Applications in Contactless Smart Cards and Identication*. John Wiley I& Sons, 2003.

[12] P. Fiorini, I. Doms, C. Van Hoof, and R. Vullers, "Micropower energy scavenging," 34th European Solid-State Circuits Conference, ESSCIRC 2008, pp. 4–9, 2008.

[13] S. P. Beeby, M. J. Tudor, and N. M. White, "Energy harvesting vibration sources for microsystems applications," *Measurement Science and Technology*, vol. 17, pp. 175–195, 2006.

[14] S. Roundy, P. K. Wright, and J. Rabaey, "A study of low level vibrations as a power source for wireless sensor nodes," *Computer Communications*, vol. 26, no. 11, pp. 1131–1144, 2003.

[15] C. B. Williams, C. Shearwood, M. A. Harradine, P. H. Mellor, T. S. Birch, and R. B. Yates, "Development of an electromagnetic micro-generator," *IEE Proceedings: Circuits, Devices and Systems*, vol. 148, no. 6, pp. 337–342, 2001.

[16] Steven R Anton and H. A. Sodano, "A review of power harvesting using piezoelectric materials (2003-2006)," *Smart Materials and Structures*, vol. 16, pp. R1–R21, 2007.

[17] James M. Gilbert and Farooq Balouchi, "Comparison of energy harvesting systems for wireless sensor networks," *International Journal of Automation and Computing*, vol. 05, no. 4, p. 334, 2008.

[18] C. Mo, R. R. Knight, A. A. Frederick, and W. W. Clark, "Energy harvesting by vibrations with mems piezoelectric benders," *ASME Conference Proceedings*, vol. 2009, no. 48982, pp. 489–494, 2009.

[19] M. Renaud, T. Sterken, A. Schmitz, P. Fiorini, C. V. Hoof, and R. Puers, "Piezoelectric harvesters and mems technology : fabrication, modeling and measurements," in *Transducers '07 and Eurosensors XXI : digest of technical papers, vols 1 and 2*, pp. U450–U451, IEEE, 2007.

[20] H. B. Fang, J. Q. Liu, Z. Y. Xu, L. Dong, L. Wang, D. Chen, B. C. Cai, and Y. Liu, "Fabrication and performance of mems-based piezoelectric power generator for vibration energy harvesting," *Microelectronics Journal*, vol. 37, no. 11, pp. 1280–1284, 2006.

[21] J.-Q. Liu, H.-B. Fang, Z.-Y. Xu, X.-H. Mao, X.-C. Shen, D. Chen, H. Liao, and B.-C. Cai, "A mems-based piezoelectric power generator array for vibration energy harvesting," *Microelectronics Journal*, vol. 39, no. 5, pp. 802–806, 2008.

[22] X.P. Zhang, L.Ye, Y-W. Mai, and S. Galea, "Fatigue crack growth and piezoelectric property decay induced by cyclic electric fields for an actuation piezoceramic," *SIF2004 Structural Integrity and Fracture*, 2004.

[23] T. Sterken, K. Baert, C. Van Hoof, R. Puers, G. Borghs, and P. Fiorini, "Comparative modelling for vibration scavengers," *IEEE*, pp. 1249–1252, 2004.

[24] Q. Ou, X. Chen, S. Gutschmidt, A. Wood, N. Leigh, and A. F. Arrieta, "An experimentally validated double-mass piezoelectric cantilever model for broadband vibration-based energy harvesting," *Journal of Intelligent Material Systems and Structures*, vol. 23, no. 2, pp. 117–126, 2012.

[25] S. Roundy, "On the effectiveness of vibration-based energy harvesting," *Journal of intelligent material systems and structures*, vol. 16, pp. 809–823, 2005.

[26] S. Roundy and Yang Zhang, "Toward self-tuning adaptive vibration based micro-generators," *Proc. SPIE Int'l Symp. Smart Materials, Nano-and Micro-Smart Systems, SPIE Press*, pp. 373–384, 2004.

[27] S. Roundy and P. Wright, "A piezoelectric vibration based generator for wireless electronics," *Smart Materials and Structures*, vol. 13, no. 5, pp. 1131–1142, 2004.

[28] M. Renaud, K. Karakaya, T. Sterken, P. Fiorini, C. V. Hoof, and R. Puers, "Fabrication, modelling and characterization of mems piezoelectric vibration harvesters," *Sensors and Actuators A: Physical*, vol. 145-146, pp. 380 – 386, 2008.

[29] B. Marinkovic and H. Koser, "Smart sand—a wide bandwidth vibration energy harvesting platform," *Applied Physics Letters*, vol. 94, no. 10, pp. 103505–3, 2009.

[30] A. Erturk and D. Inman, "Issues in mathematical modeling of piezoelectric energy harvesters," *Smart Materials and Structures*, vol. 17, no. 6, 2008.

[31] H. Sodano, G. Park, and D. Inman, "Estimation of electric charge output for piezoelectric energy harvesting," *Strain*, vol. 40, no. 2, pp. 49–58, 2004.

[32] P. H. A. and DasGupta, *Vibrations and Waves in Continuous Mechanical Systems*. Wiley, 2007.

[33] L. Meirovitch, *Elements of vibration analysis*. McGraw-Hill, 1986.

[34] J. Humar, *Dynamics of structures*. A.A. Balkema Publishers, 2002.

[35] A. Erturk and D. J. Inman, "An experimentally validated bimorph cantilever model for piezoelectric energy harvesting from base excitations," *Smart Materials and Structures*, vol. 18, no. 2, p. 025009, 2009.

[36] C. De Marqui Junior, A. Erturk, and D. J. Inman, "An electromechanical finite element model for piezoelectric energy harvester plates," *Journal of Sound and Vibration*, vol. 327, no. 1-2, pp. 9–25, 2009.

[37] M. Lumentut, K. Teh, and I. Howard, "Computational fea model of a coupled piezoelectric sensor and plate structure for energy harvesting," *Australian Journal of Mechanical Engineering*, vol. 5, no. 2, pp. 199–208, 2008.

[38] H. Xue, Y. Hu, and Q.-M. Wang, "Broadband piezoelectric energy harvesting devices using multiple bimorphs with different operating frequencies," *IEEE Transactions on Ultrasonics, Ferroelectrics, and Frequency Control*, vol. 55, no. 9, pp. 2104–2108, 2008.

[39] T. Kazmierski and S. Beeby, *Energy Harvesting Systems: Principles, Modeling and Applications*. Springer, 2010.

[40] S. M. Shahruz, "Design of mechanical band-pass filters for energy scavenging: Multi-degree-of-freedom models," *Journal of Vibration and Control,*, vol. 14, no. 5, pp. 753–768, 2008.

[41] Y. Tadesse, S. Zhang, and S. Priya, "Multimodal energy harvesting system: Piezoelectric and electromagnetic," *Journal of Intelligent Material Systems and Structures*, vol. 20, no. 5, pp. 625–632, 2009.

[42] N. Ching, H. Wong, W. Li, P. Leong, and Z. Wen, "A laser-micromachined multi-modal resonating power transducer for wireless sensing systems," *Sensors and Actuators, A: Physical*, vol. 97-98, pp. 685–690, 2002.

[43] I.-H. Kim, H.-J. Jung, B. Lee, and S.-J. Jang, "Broadband energy-harvesting using a two degree-of-freedom vibrating body," *Applied Physics Letters*, vol. 98, no. 21, 2011.

[44] S. Lee, B. D. Youn, and B. Jung, "Segment-type energy harvester powering wireless sensor for building automation," Proceedings of the ASME 2009 International Design Engineering Technical Conference & Computers and Information in Engineering Conference, IDETC/CIE, 2009.

[45] S. Dong, J. Zhai, J. Li, and D. V. S. Priya, "Multimodal system for harvesting magnetic and mechanical energy," *Applied Physics Letters*, vol. 93, no. 10, 2008.

[46] M. S. M. Soliman, E. M. Abdel-Rahman, E. F. El-Saadany, and R. R. Mansour, "A wideband vibration-based energy harvester," *Journal of Micromechanics and Microengineering*, vol. 18, no. 11, 2008.

[47] J.-T. Lin, B. Lee, and B. Alphenaar, "The magnetic coupling of a piezoelectric cantilever for enhanced energy harvesting efficiency," *Smart Materials and Structures*, vol. 19, no. 4, 2010.

[48] S. Moss, I. Powlesland, M. Konak, A. Barry, and S. G. G. Carman, "Broadband vibro-impacting energy harvester," *Materials Science Forum*, vol. 654-656, pp. 2799–2802, 2010.

[49] J. Yang, Y. Wen, P. Li, and X. Dai, "Design, modeling, and performance measurements of a broadband vibration energy harvester using a magnetoelectric transducer," *Instrumentation Science and Technology*, vol. 39, no. 3, pp. 312–323, 2011.

[50] V. Challa, M. Prasad, and F. Fisher, "Towards an autonomous self-tuning vibration energy harvesting device for wireless sensor network applications," *Smart Materials and Structures*, vol. 20, no. 2, 2011.

[51] D. Barton, S. Burrow, and L. Clare, "Energy harvesting from vibrations with a nonlinear oscillator," *Journal of Vibration and Acoustics, Transactions of the ASME*, vol. 132, no. 2, pp. 0210091–0210097, 2010.

[52] S. Stanton and C. M. B. Mann, "Nonlinear dynamics for broadband energy harvesting: Investigation of a bistable piezoelectric inertial generator," *Physica D: Nonlinear Phenomena*, vol. 239, no. 10, pp. 640–653, 2010.

[53] A. Erturk and D. Inman, "Broadband piezoelectric power generation on high-energy orbits of the bistable duffing oscillator with electromechanical coupling," *Journal of Sound and Vibration*, vol. 330, no. 10, pp. 2339–2353, 2011.

[54] D. Quinn, A. Triplett, A. Vakakis, and L. Bergman, "Energy harvesting from impulsive loads using intentional essential nonlinearities," *Journal of Vibration and Acoustics, Transactions of the ASME*, vol. 133, no. 1, 2011.

[55] J. Moehlis, B. DeMartini, and J. R. K. Turner, "Exploiting nonlinearity to provide broadband energy harvesting," No. PART A, pp. 119–121, 2010.

[56] M. Lallart, S. Anton, and D. Inman, "Frequency self-tuning scheme for broadband vibration energy harvesting," *Journal of Intelligent Material Systems and Structures*, vol. 21, no. 9, pp. 897–906, 2010.

[57] N. Kong, D. Ha, A. Erturk, and D. Inman, "Resistive impedance matching circuit for piezoelectric energy harvesting," *Journal of Intelligent Material Systems and Structures*, vol. 21, no. 13, pp. 1293–1302, 2010.

[58] J. Liang and W.-H. Liao, "Impedance matching for improving piezoelectric energy harvesting systems," vol. 7643, 2010.

[59] C. Luo and H. H.F., "Wideband energy harvesting for piezoelectric devices with linear resonant behavior," *Ultrasonics, Ferroelectrics and Frequency Control, IEEE Transactions on*, vol. 58, pp. 1294 –1301, july 2011.

[60] D. Charnegie, "Frequency tuning concepts for piezoelectric cantilever beams and plates for energy harvesting," Master's thesis, Pittsburgh, 2007.

[61] e. a. Xiaoming Wu, "A frequency adjustable vibration energy harvester," *Proceedings of PowerMEMS 2008+ microEMS2008*, 2008.

[62] Eli S Leland and P. K. Wright, "Resonance tuning of piezoelectric vibration energy scavenging generators using compressive axial preload," *Smart Materials and Structures*, vol. 15, pp. 1413–1420, 2006.

[63] Vinod R Challa, M G Prasad, Yong Shi, and F. T. Fisher, "A vibration energy harvesting device with bidirectional resonance frequency tunability," *Smart Materials and Structures*, vol. 17, p. 10, 2008.

[64] C. Eichhorn, R. Tchagsim, N. Wilhelm, and P. Woias, "A smart and self-sufficient frequency tunable vibration energy harvester," *Journal of Micromechanics and Microengineering*, vol. 21, no. 10, 2011.

[65] C. Peters, D. Maurath, W. Schock, F. Mezger, and Y. Manoli, "A closed-loop wide-range tunable mechanical resonator for energy harvesting systems," *Journal of Micromechanics and Microengineering*, vol. 19, no. 9, 2009.

[66] M. S. M. Soliman, E. F. El-Saadany, and R. R. Mansour, "Electromagnetic and electrostatic micro-power generators; an overview," vol. 1, pp. 89–93 Vol. 1, 2005.

[67] N. G. Stephen, "On energy harvesting from ambient vibration," *Journal of Sound and Vibration*, vol. 293, no. 1-2, pp. 409–425, 2006.

[68] L. Tang, Y. Yang, and C. Soh, "Toward broadband vibration-based energy harvesting," *Journal of Intelligent Material Systems and Structures*, vol. 21, no. 18, pp. 1867–1897, 2010.

[69] "Getting started with vibration energy harvesting," *Perpetuum Ltd.*

[70] *IEEE Standard on Piezoelectricity.* IEEE, New York, 1988.

[71] D. Wang and N. Liu, "A shear mode piezoelectric energy harvester based on a pressurized water flow," *Sensors and Actuators A: Physical*, vol. 167, pp. 449–458, jun 2011.

[72] A. Erturk and D. Inman, "A distributed parameter electromechanical model for cantilevered piezoelectric energy harvesters," *Journal of Vibration and Acoustics, Transactions of the ASME*, vol. 130, no. 4, 2008.

[73] S. Priya and D. J. Inman, *Energy Harvesting Technologies.* Springer, 2009.

[74] S. Roundy, S. E. Leland, J. Baker, E. Carleton, E. Reilly, E. Lai, B. Otis, J. Rabaey, K. Wright P, and V. Sundararajan, "Improving power output for vibration-based energy scavengers," *IEEE Pervasive Computing*, vol. 4, no. 1, pp. 28–36, 2005.

[75] A. Phipps and T. Nishida, "System modeling of piezoelectric energy harvesters," *Power Electronics, IEEE Transactions on*, vol. PP, no. 99, p. 1, 2011.

[76] J. Scruggs, "An optimal stochastic control theory for distributed energy harvesting networks," *Journal of Sound and Vibration*, vol. 320, no. 45, pp. 707 – 725, 2009.

[77] G. W. Bohannan, *Application of fractional calculus to polarization dynamics in solid dielectric materials.* PhD thesis, Montana State University, 2000.

[78] G. Ottman, H. Hofmann, and G. Lesieutre, "Optimized piezoelectric energy harvesting circuit using step-down converter in discontinuous conduction mode," *IEEE Transactions on Power Electronics*, vol. 18, no. 2, pp. 696–703, 2003.

[79] K. Wolf and O. Gottlieb, "Nonlinear dynamics of a noncontacting atomic force microscope cantilever actuated by a piezoelectric layer," *Journal of Applied Physics*, vol. 91, no. 7, p. 4701, 2002.

[80] A. Cammarano, S. Burrow, D. Barton, A. Carrella, and L. Clare, "Tuning a resonant energy harvester using a generalized electrical load," *Smart Materials and Structures*, vol. 19, no. 5, 2010.

[81] J. R. Farmer, "A comparison of power harvesting techniques and related energy storage issues," Master's thesis, Virginia Polytechnic Institute and State University, 2007.

[82] IDTechEx, "Energy harvesting journal," *www.energyharvestingjournal.com*, May 2012.

[83] X. Li, Y. Li, J. E. Seem, and P. Lei, "Maximum power point tracking for photovoltaic systems using adaptive extremum seeking control," *ASME Conference Proceedings*, vol. 2011, no. 54754, pp. 803–810, 2011.

[84] S. Acharya, S.-K. Lee, J.-H. Hyung, Y.-H. Yang, B.-H. Kim, and B.-G. Ahn, "Ferroelectric and piezoelectric properties of lead-free batio 3 doped bi 0.5na 0.5tio 3 thin films from metal-organic solution deposition," *Journal of Alloys and Compounds*, vol. 540, pp. 204–209, 2012.

[85] B. Wu, C. Han, D. Xiao, Z. Wang, J. Zhu, and J. Wu, "Investigation of a new lead-free (0.89 - x)(bi 0.5na 0.5)tio 3-0.11(bi 0.5k 0.5)tio 3-xba 0.85ca 0.15ti 0.90zr 0.10o 3 ceramics," *Materials Research Bulletin*, vol. 47, no. 11, pp. 3937–3940, 2012.

[86] W. Lin, L. Fan, D. Lin, Q. Zheng, X. Fan, and H. Sun, "Phase transition, ferroelectric and piezoelectric properties of ba 1-xca xti 1-yzr yo 3 lead-free ceramics," *Current Applied Physics*, vol. 13, no. 1, pp. 159–164, 2013.

A

Appendix

A.1 Eigenfunctions of Single Mass Cantilever Beams

Referring to Section 4.3, the derivation of eigenfunctions $\phi_r(x)$ involves modal analysis, which only focuses on the dynamics of free vibration by excluding all external forces. In modal analysis, the equation of motion becomes

$$m\ddot{w}(x,t) + c_s I\dot{w}''''(x,t) + Y_p I w''''(x,t) = 0. \tag{A.1}$$

By substituting the hypothesis solution (4.25) to (A.1) and rearranging, the functions of $\phi_r(x)$ and $\eta_r(t)$ are separated as

$$\phi_r''''(x) - \frac{\omega_r^2 m}{Y_p I}\phi_r(x) = 0, \tag{A.2}$$

and

$$\ddot{\eta}_r(t) + \omega_r^2\Big[\eta_r(t) + \frac{c_s}{Y_p}\dot{\eta}_r(t)\Big] = 0. \tag{A.3}$$

For convenience, the equation (A.2) can be rewritten to

$$\phi_r''''(x) - \Big(\frac{\lambda_r}{L_b}\Big)^4\phi_r(x) = 0, \tag{A.4}$$

where

$$\Big(\frac{\lambda_r}{L_b}\Big)^4 = \frac{\omega_r^2 m}{Y_p I}, \text{ or } \omega_r = \lambda_r^2\sqrt{\frac{Y_p I}{m L_b^4}}. \tag{A.5}$$

The general solution for (A.4) can be written in the form

$$\phi_r(x) = c_1\sin(\frac{\lambda_r}{L_b}x) + c_2\cos(\frac{\lambda_r}{L_b}x) + c_3\sinh(\frac{\lambda_r}{L_b}x) + c_4\cosh(\frac{\lambda_r}{L_b}x). \tag{A.6}$$

From the variational principle [32], the following four boundary conditions are obtained for the cantilever beam with a tip mass:

$$w_{rel}(0,t) = 0, \tag{A.7}$$

$$w'_{rel}(0,t) = 0, \tag{A.8}$$

$$I_t \ddot{w}'_{rel}(L_b,t) + Y_p I w''_{rel}(L_b,t) = 0, \tag{A.9}$$

$$-M_t \ddot{w}_{rel}(L_b,t) + Y_p I w'''_{rel}(L_b,t) = 0. \tag{A.10}$$

Substituting (4.25) to (A.7) - (A.10), the four boundary conditions can be written in terms of $\phi_r(x)$ as:

$$\phi_r(0) = 0, \tag{A.11}$$

$$\phi'_r(0) = 0, \tag{A.12}$$

$$-I_t \omega_r^2 \phi'_r(L_b) + Y_p I \phi''_r(L_b) = 0, \tag{A.13}$$

$$M_t \omega_r^2 \phi_r(L_b) + Y_p I \phi'''_r(L_b) = 0. \tag{A.14}$$

Substituting (A.6) to (A.11) - (A.14), a system of linear equations is obtained:

$$\mathbf{K}\mathbf{c} = \mathbf{0}, \tag{A.15}$$

where $\mathbf{K}$ is a 4×4 matrix, and $\mathbf{c}$ is the column vector of $[c_1\, c_2\, c_3\, c_4]$. The characteristic equation is obtained from setting the determinant of $\mathbf{K}$ to zero. The general solution of $\mathbf{c}$ is the null space of $\mathbf{K}$.

B

Appendix

B.1 Numerical values of parameters and material properties.

Table B.1: Parameters and material properties of the PZT beam used for experimental validation referred in Section 4.6.1.

Description	Symbol	Value
PZT connection		Series
Beam width	b	5.4 mm
Beam length	L	23.2 mm
Thickness of single PZT layer	h_p	0.13 mm
Thickness of substrate	h_s	0.12 mm
PZT density	ρ_p	7800 kg/m^3
Substrate density	ρ_s	7200 kg/m^3
Substrate elastic modulus	Y_s	120 GPa
PZT elastic modulus	Y_p	62 GPa
Relative permittivity	ε_r	3800 F/m
PZT constant	d_{31}	-320×10^{-12} m/V
Mechanical damping ratio	ξ_m	0.007

Table B.2: Parameters and material properties of the single-mass PZT beam used for experimental validation referred in Section 4.6.2.

Description	Symbol	Value
PZT connection		Series
Mass dimension	$w \times h \times l$	$5.42 \times 5.42 \times 5.10$ mm^3
Mass density	ρ_m	7794 kg/m^3
Beam width	b	5.4 mm
Beam length	L	19.4 mm
Thickness of single PZT layer	h_p	0.13 mm
Thickness of substrate	h_s	0.12 mm
PZT density	ρ_p	7800 kg/m^3
Substrate density	ρ_s	7200 kg/m^3
Substrate elastic modulus	Y_s	120 GPa
PZT elastic modulus	Y_p	62 GPa
Relative permittivity	ε_r	3800 F/m
PZT constant	d_{31}	-320×10^{-12} m/V
Mechanical damping ratio	ξ_m	0.02

Table B.3: Parameters and material properties of the double-mass PZT beam used for experimental validation referred in Section 5.3.1.

Parameters/Properties	Symbol	Value
Elastic modulus	Y_s	200 GPa
Beam width	b	11.2 mm
Beam thickness	h_s	6.5 mm
Beam density	ρ_s	7800 kg m^{-3}
Mass 1 distance	L_1	36 mm
Mass 2 distance	L_2	50 mm
Mass dimension	$w \times h \times l$(mm)	$10 \times 10 \times 10$ mm^3
Mass density	ρ_m	7900 kg m^{-3}
1$^{\text{st}}$ mode damp. ratio	ξ_1	0.010
2$^{\text{nd}}$ mode damp. ratio	ξ_2	0.004

Table B.4: Parameters and material properties of the double-mass PZT beam used for experimental validation referred in Section 5.3.2.

Description	Symbol	Value
Mass dimension	$w \times h \times l$	$6 \times 6 \times 6$ mm^3
Mass density	ρ_m	7920 kg/m^3
Beam width	b	6 mm
Beam length	L_1	13.8 mm
Beam length	L_2	26.5 mm
Thickness of PZT layer	h_p	0.16 mm
Thickness of substrate	h_s	0.19 mm
PZT density	ρ_p	7800 kg/m^3
Substrate density	ρ_s	7200 kg/m^3
Substrate elastic modulus	Y_s	110 GPa
PZT elastic modulus	Y_p	66 GPa
Relative permittivity	ε_r	1800 F/m
PZT constant	d_{31}	-190 $\times 10^{-12}$ m/V
1$^{\text{st}}$ mode damping ratio	ξ_1	0.04
2$^{\text{nd}}$ mode damping ratio	ξ_1	0.012
Load resistance	R_L	20 kΩ

Table B.5: Parameters and material properties of the single mass PZT beam used for modulus matching experimental validation referred in Section 6.3.

Description	Symbol	Value
Mass dimension	$w \times h \times l$	$5.7 \times 5.5 \times 5.2$ mm^3
Mass density	ρ_m	7794 kg/m^3
Beam width	b	6.35 mm
Beam length	L	23.9 mm
Thickness of single PZT layer	h_p	0.19 mm
Thickness of substrate	h_s	0.13 mm
Thickness of electrode layer	h_c	0.5 μm
Electrode resistivity (nickel)	ρ_e	6.99 $\times 10^{-8}\Omega$·m
PZT density	ρ_p	7800 kg/m^3
Substrate density	ρ_s	7200 kg/m^3
Substrate elastic modulus	Y_s	110 GPa
PZT elastic modulus	Y_p	66 GPa
Relative permittivity	ε_r	1800 F/m
PZT constant	d_{31}	-190×10^{-12} m/V
PZT loss tangent	θ_{LT}	0.015
Mechanical damping ratio	ξ_m	0.01

Table B.6: Parameters and material properties of the single mass PZT beam used for modulus matching experimental validation referred in Section 6.3.3.

Description	Symbol	Value
Mass dimension	$w \times h \times l$	$5.7 \times 5.5 \times 5.2$ mm^3
Mass density	ρ_m	7794 kg/m^3
Beam width	b	6.35 mm
Beam length	L	20.3 mm
Thickness of single PZT layer	h_p	0.19 mm
Thickness of substrate	h_s	0.13 mm
Thickness of electrode layer	h_c	0.5 μm
Electrode resistivity (nickel)	ρ_e	6.99 $\times 10^{-8}\Omega$·m
PZT density	ρ_p	7800 kg/m^3
Substrate density	ρ_s	7200 kg/m^3
Substrate elastic modulus	Y_s	110 GPa
PZT elastic modulus	Y_p	66 GPa
Relative permittivity	ε_r	1800 F/m
PZT constant	d_{31}	-190×10^{-12} m/V
PZT loss tangent	θ_{LT}	0.015
Mechanical damping ratio	ξ_m	0.01

Table B.7: Circuit parameter for input acceleration of 1 g at 140.1 Hz referred in Section 6.3.2.

Parameter	Symbol	Value from the improved model
Output voltage	V_o	37.81 V
Output current	I_o	0.055 mA
Load resistance	R_L	684.73 kΩ
Contact ohmic losses resistance	R_{ce}	0.177 Ω
Polarisation losses resistance	R_p	12 MΩ
Power harvested	P_{R_L}	2.088 mW
Contact ohmic losses	$p_{R_{ce}}$	0.0005393 mW
Polarisation losses	p_{R_p}	0.1191 mW
Total losses	p_{Losses}	0.1196 mW
$\frac{\text{Contact ohmic losses}}{\text{Total losses}}$	$\frac{P_{R_{ce}}}{P_{Losses}}$	0.45 %
$\frac{\text{Total losses}}{\text{Total power}}$	$\frac{P_{Losses}}{P_{Losses} + P_{R_L}}$	5.4 %

Table B.8: Parameters and material properties of prototype 7.4.3.

Description	Symbol	Value
Elastic modulus	Y	210 GPa
Beam width (for all beams)	b	12 mm
Beam thickness (for all beams)	h_t	0.6 mm
Beam density (for all beams)	ρ_b	7800 kg/m^3
Beam 1 length	L_1	75 mm
Beam 2 length max.	$L_{2e,max}$	31 mm
Beam 2 length min.	$L_{2e,min}$	12.5 mm
Proof Mass	M_t	310 g

Table B.9: Parameters and material properties of prototype 7.5.1.

Description	Symbol	Value
Substrate elastic modulus	Y_s	210 GPa
PZT elastic modulus	Y_P	52 GPa
Beam width	b	10 mm
Substrate thickness	h_s	0.45 mm
PZT thickness	h_p	0.19 mm
Substrate length	l	50 mm
PZT length	l_{0-1}	21.8 mm
Substrate density	ρ_s	7800 kg/m^3
Spring constant max.	k_{max}	6080 N/m
Spring constant min.	k_{min}	90 N/m
Proof Mass	M_t	32 g